INFORMATION TO USERS

This manuscript has been reproduced from the microfilm master. UMI films the text directly from the original or copy submitted. Thus, some thesis and dissertation copies are in typewriter face, while others may be from any type of computer printer.

The quality of this reproduction is dependent upon the quality of the copy submitted. Broken or indistinct print, colored or poor quality illustrations and photographs, print bleedthrough, substandard margins, and improper alignment can adversely affect reproduction.

In the unlikely event that the author did not send UMI a complete manuscript and there are missing pages, these will be noted. Also, if unauthorized copyright material had to be removed, a note will indicate the deletion.

Oversize materials (e.g., maps, drawings, charts) are reproduced by sectioning the original, beginning at the upper left-hand corner and continuing from left to right in equal sections with small overlaps.

ProQuest Information and Learning
300 North Zeeb Road, Ann Arbor, MI 48106-1346 USA
800-521-0600

Use of Vibrator Performance Data to Improve Near-Surface Velocity Determination

BY

Mustafa Naser Ali Al-Ali

A Thesis Presented to the

DEANSHIP OF GRADUATE STUDIES

KING FAHD UNIVERSITY OF PETROLEUM & MINERALS

DHAHRAN, SAUDI ARABIA

In Partial Fulfillment of the

Requirements for the Degree of

MASTER OF SCIENCE

In

GEOLOGY

MAY 2002

ProQuest Information and Learning Company
300 North Zeeb Road
P.O. Box 1346
Ann Arbor, MI 48106-1346

KING FAHD UNIVERSITY OF PETROLEUM AND MINERALS
DHAHRAN, SAUDI ARABIA

DEANSHIP OF GRADUATE STUDIES

This thesis, written by **Mustafa Naser Al-Ali** under the direction of his Thesis advisor and approved by his Thesis committee, has been presented to and accepted by the Dean of Graduate Studies, in partial fulfillment of the requirements for the degree of **MASTER OF SCIENCE IN GEOLOGY**.

Thesis Committee

Chairman (Dr. Gabor Korvin)

Member (Dr. M. Makkawi)

Member (Dr. R. Hastings-James)

Department Chairman
Dr. M. Hariri

Dean of Graduate Studies
Prof. O. Jannadi

19/5/02
Date

عمادة الدراسات العليا
DEANSHIP OF GRADUATE STUDIES

Dedication

This thesis is dedicated to the fond memory of my father Naser and my mother.

ACKNOWLEDGMENTS

Acknowledgments are due to the King Fahd University of Petroleum and Minerals for supporting this research, and Saudi Aramco and the Ministry of Petroleum and Mineral Resources for permission to publish this thesis.

I am greatly indebted to my thesis chairman, Dr. Gabor Korvin, for his guidance and for his thorough and prompt review of the manuscript. I am sincerely grateful to my thesis member, Dr. Mohammad Makkawi, for his great assistance and advice especially in the geostatistical part of this study. I am also indebted to my thesis committee member, Dr. Richard Hastings-James, for his support and for many helpful insights and suggestions.

I am thankful to Earth Sciences Department Chairman Dr. Mustafa Al-Hariri and other faculty and colleagues for their support during my association with them.

I would like to express my thanks to Saudi Aramco management for their continuous support and permission to use Saudi Aramco facilities and data. Among these, I thank Mr. Mahmoud Abdul-Baqi, Vice President of Exploration; Mr. Abdulla Al-Naim, Manager of Area Exploration; Dr. Kamal Al-Yahya, Manager of Exploration Operations; Dr. A. Al-Dulaijan, Assistant to VP, Exploration; Mr. Ali Al-Hauwaj, Chief Explorationist of Eastern Area Exploration; Dr. Mohammed Al-Faraj; Chief Geophysicist of Research and development; Mr. Adil Al-Khelaiwi, Chief Geophysicist of Geophysical Data Acquisition; Mr. Yousef Al-Ali, Chief Geophysicist of Geophysical Data Acquisition; Mr. AbdulNasser Khusheim, Team Leader of East Ghawar Exploration.

I thank Mr. Said Al-Hajri for his guidance and assistance in the field trip and Mr. Riyadh Al-Saad for his assistance in processing the seismic data. I also thank Dr. Zaki Harari for bringing the civil engineering literature to my attention. Thanks are due to Dr. Denis Mougenot and Mr. Jacques Hamon from CGG for their help.

Last but not least, I put in record my high appreciation to the support of my family during the study period.

TABLE OF CONTENTS

LIST OF TABLES

LIST OF FIGURES

THESIS ABSTRACT

Name: Mustafa Naser Ali Al-Ali
Title: Use of Vibrator Performance Data to Improve Near-Surface Velocity Determination
Major Field: Geology
Date: May 2002

Reliable estimation of near-surface *P*-wave velocity is one of the key problems in land seismic exploration. Uphole surveys are usually used to acquire near-surface velocity information. However, in the presence of rapidly varying near-surface geology, such estimation is inherently uncertain due to the sparse uphole sampling grid.

A principal goal of this study is to determine a relationship between the densely sampled vibrator performance control data, obtained in the course of normal seismic data acquisition, and uphole *P*-wave velocity so that the two data sets can be integrated using geostatistical techniques to provide improved near surface velocity models.

A theoretical model was derived relating near-surface *P*-wave velocity to vibrator control system estimates of ground stiffness and viscosity. Estimated velocity from these vibrator measurements exhibited good statistical correlation over a large 3D seismic survey area with uphole velocities down to a 50-meter depth.

Two 3D near-surface velocity models were constructed using uphole data alone as well as combined with vibrator information, both of which were used to calculate statics. The seismic imaging results obtained using these statics were found to be better than using uphole data alone. On the basis of these results, we concluded that the integrated model resolved statics better than models that individually utilized uphole data through geostatistical and conventional computation techniques.

Master of Science Degree

King Fahad University of Petroleum and Minerals
Dhahran, Saudi Arabia

May 2002

ملخص الرسالة

الاسـم : مصطفى ناصر علي العلي
العنوان : استخدام قياسات نظام تحكم جهاز الاهتزازات السيزموغرافيه لتحسين قياس سرعة الموجات الصوتية في الطبقات القريبة من سطح الأرض
التخصص : جيولوجيا
التاريخ : مايو ٢٠٠٢ م

تعتبر عملية تحديد سرعة الموجات الصوتية في الطبقات القريبة من سطح الأرض واحدة من الصعوبات التي تواجه عملية الاستكشاف السيزموغرافي على اليابسة. عادةً تقاس السرعة في هذه الطبقات من خلال حفر آبار مخصصة لهذا الغرض، ولكن التغيرات في سرعة الموجات الصوتية من مكان إلى آخر قرب السطح يجعل عملية تحديد السرعة في منطقة ما بأكملها غير دقيقة نظرا لقلة وتباعد الآبار المخصصة لقياس السرعة وذلك لكلفتها العالية.

أن الهدف الأساسي من هذه الدراسة هو ايجاد علاقة بين سرعة الموجات الصوتية في الطبقات القريبة من السطح المقاسه عن طريق الآبار المخصصة لذلك وتلك القياسات المستقاة من نظام تحكم جهاز الاهتزازات السيزموغرافيه من خلال المسح السيزموغرافي والتي هي بطبيعتها اكثر كثافة من الآبار . بعد ذلك سوف يتم
دمج هذه المعلومات عن طريق تطبيقات الجيولوجيا الإحصائية.

لقد أوجدت هذه الرسالة علاقة نظرية بين سرعة الموجات الصوتية ومعلومات الصلابة واللزوجة الأرضية اللتين يقيسهما نظام تحكم جهاز الاهتزازات السيزموغرافيه . ذلك ساعد على حساب تقديري للسرعة الصوتية من هذه القياسات والتي أظهرت مقارنة جيده مع قياسات الآبار في منطقة الدراسة إلى عمق ٥٠ متر تحت سطح الأرض.

استخدمت هذه العلاقة في بناء مجسمين ثلاثي الأبعاد للسرعة الصوتية في الطبقات القريبة من السطح باستخدام تطبيقات الجيولوجيا الإحصائية، وذلك أولا باستخدام قياسات الآبار على حده، وثانيا باستخدام قياسات الآبار وقياسات أجهزة الاهتزازت . هذه المجسمات استخدمت في معالجة تشويشات المعلومات السيزموغرافيه . أثبتت النتائج أن استخدام قياسات الآبار مع قياسات أجهزة الاهتزازات نتج عنه مقاطع سيزموغرافيه للأرض احسن من نظيراتها الناتجة من استخدام قياسات الآبار فقط، على أساس هذه النتائج، استنتجت هذه الدراسة أن عملية تحديد السرعة في الطبقات القريبة من سطح الأرض يمكن تحسينها عن طريق دمجها مع المعلومات الناتجة من نظام تحكم جهاز الاهتزازات السيزموغرافيه.

درجة الماجستير في العلوم
جامعة الملك فهد للبترول والمعادن
الظهران/ المملكة العربية السعودية
مايو ٢٠٠٢م

CHAPTER 1

INTRODUCTION AND STUDY APPROACH

1.1 Introduction

A good knowledge of near surface layers velocity model is vital for hydrocarbon reservoir exploration and characterization that utilize seismic data. For instance, this model is crucial for statics solution and depthing. However, the complexities of near surface layers make its determination, using direct measurements via uphole surveys, economically prohibitive. In the hydrocarbon industry, the cost of information is very critical. Therefore, tools are needed to estimate near surface velocity using available data in order to minimize the risk associated with depthing errors resulting from an incomplete knowledge of the near-surface.

Geostatistics is one of the tools that are becoming routinely used in hydrocarbon industry to predict reservoir parameters based on an available limited number of data samples. In addition, geostatistics is used to integrate data of different scales. For

example, the dense spatially well-sampled 3D seismic data could be efficiently integrated with sparsely but vertically well sampled reservoir properties using geostatistical techniques. In this case, seismic attributes are integrated with direct measurements, made in the wells, to improve the determination of reservoir properties. Consequently, this integration approach can be applied at any level within the earth layers (for example to improve near surface layers velocity model obtained from direct measurements such as upholes) provided that other related data components are available.

Modern vibrator control systems estimate the actual ground force generated by vibrators relative to the theoretical input signal. There is always a difference between the actual and the theoretical signals because the former are affected by surface conditions. These conditions determine the vibrator surface coupling which depends on surface elastic properties. Vibrator control system measurements have the same spatial sampling rate as the source grid in the seismic survey, which is considerably finer than the uphole grid.

While vibrating at any location on the ground, the vibrator exerts a force that is opposed by a counter force from the ground. The response of the ground to the applied force is sensed from the motion of the vibrator baseplate. The ground force, in addition to the baseplate motion, can be used to obtain information about ground physical properties. Modern vibrator controllers use a Kalman filter incorporating dynamic mathematical models of the ground and the vibrator to estimate both the ground force applied by the vibrator, and the stiffness and viscosity of the ground. In addition, other vibrator performance control data are acquired at every vibration point (VP). These are average and maximum values of phase, force and distortion.

1.2 Study Approach

In Chapter 2 we discuss the involved parameters including vibrator performance control data, uphole data, and their spatial analyses by geostatistical techniques. An analytical solution will be developed to relate the ground parameters: viscosity and stiffness to the seismic wave velocity in an elastic half-space. This solution can be used to estimate seismic wave velocity in the near surface layers from ground parameters. Other vibrator performance control data will be numerically related.

Subsequently, in Chapter 3 the real data that will be used to implement this approach will be analyzed. The real data is obtained from an area of about 2,450 km^2 located west of Ghawar field in Saudi Arabia, Figure 1.1. This area contains 463 upholes that penetrate the near surface layers down to different depths. In addition, vibrator performance data have been obtained from a recently acquired 3D seismic survey. Area surface geology will be studied in order to understand the vibrator performance data spatial variations.

In Chapter 4 uphole and vibrator performance control data relations will be analyzed. Then, five velocity maps to depths of 10 to 50 meters with an increment of 10 meters from the surface will be constructed for both uphole and integrated data. Results will be validated using data from 20 excluded upholes.

Following that, in Chapter 5, two 3D velocity models will be constructed for the near surface layers in the study area. First, a model will be generated using only uphole data. The second velocity model will be generated by integrating uphole and vibrator performance control data. These models will be used to calculate statics correction, which in turn, will be applied to stack seismic data in a portion of the study area. Furthermore,

two data sets including uphole and vibrator performance data obtained from two other areas in Saudi Arabia will be presented to illustrate the regional application of this method. Finally, conclusions and recommendations will be given in Chapter 6.

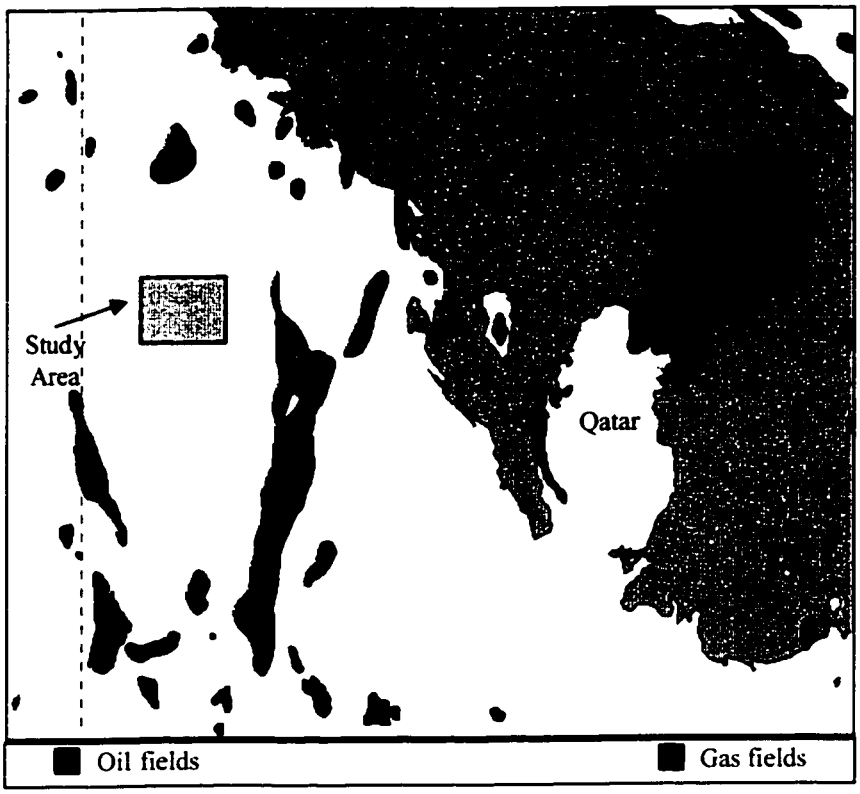

Figure 1.1: Study area location map.

CHAPTER 2

PARAMETERS REVIEW AND HYPOTHESIS DEVELOPMENT

2.1 Vibrator Performance Control Data

2.1.1 Introduction

On land, seismic energy is generated by impulsive or vibratory energy sources. Among the latter is the Vibroseis® method that was first introduced by Continental Oil Company (CONOCO) in 1958 (Figure 2.1). Vibroseis energy is generated by a hydraulic vibrator that actuates a steel plate coupled firmly against the ground for a certain period of time. Since 1961, this method has become the most used seismic energy source in land. More than 50% of the world land seismic surveys acquired in 1991 used vibroseis sources (Baliguet, 1992). The method received its popularity over the explosive sources because it is environmentally friendly, capable of high production, and theoretically produces

controllable down-going wavelet. Because of the great success and popularity of this method, the ideal way of controlling the phase and amplitude of vibroseis seismic generated wavelet was a subject for extensive research (Lerwill, 1981).

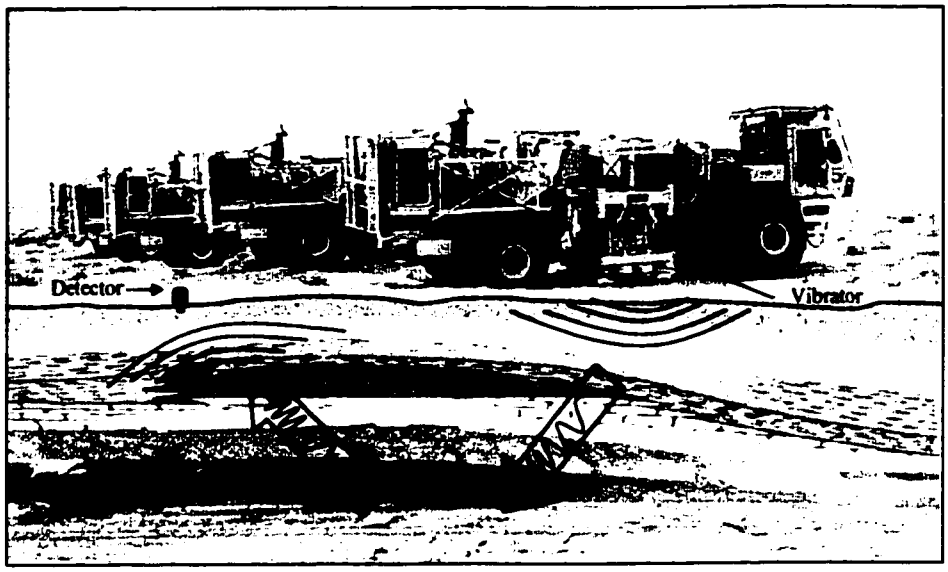

Figure 2.1: Vibroseis method.

The method of vibrator control was much debated from 1975 to mid 1980s. Thigpen et al. (1975) recommended the baseplate for phase control. Lerwill (1981) advocated the reaction mass model, while Sallas (1984) showed the ground force phase control method to be better. These methods were all tested by Martin and Jack (1990). They concluded that none of these methods was much better than any other. Baeten and Ziolkowski (1990) provided a detailed discussion of these phase control methods and proposed a new method called flexural rigidity that takes into account all the forces acting on or at the baseplate. Later, Pelton implemented a proto-type control system using an accelerometer-array on the baseplate and obtained encouraging results; however the method was too costly to justify commercial use. Currently, the Sallas (1984) model incorporating the concept of "ground-force" has become by far the most popular method of phase control.

It is well established that the results of vibroseis seismic data depend on the coupling between vibrator and ground and the ambient noise level (Meunier, 1996). These results include the actual recorded seismic data and the vibrator performance control system feedback. Vibrator ground coupling is controlled by the elastic properties of the medium. Garotta (1990) and Postel et al. (1996) found correlation between down-going vibrator wavelet and ground conditions. These observations form the motivation for my current research, where vibrator performance control data will be correlated with near-surface compressional wave velocity obtained from well measurements and the relationship between the two data sets will be investigated using geostatistics.

2.1.2 Ground Force Phase Control Model

Sallas and Weber introduced the dynamic force phase locking technique in 1982 to control the phase and amplitude of the vibrator generated seismic signal. In this technique, the dynamic ground force is represented by a weighted sum of the baseplate and reaction mass accelerations. Simple models for vibrator mechanical system and the earth's impedance seen by the vibrator were assumed to illustrate this technique.

Vibrator Mechanical Model

Figure 2.2a shows the vibrator mechanical model of Sallas and Weber. The parameters of this model are defined as follows:

Z_r Reaction mass displacement (m)

Z_b Baseplate displacement (m)

Fa Actuator force (N), force applied by the hydraulic fluid on the piston

F_t Dynamic force of the vibrator vehicle acting on the baseplate (N)

F_g Dynamic ground force (N) that is the force exerted by vibrator on earth

M_r Mass of the reaction mass (kg)

M_b Baseplate mass (kg)

K_a Actuator oil column spring constant (N/m)

D_a Actuator damping or dashpot constant (N.s/m)

M_g Effective captured ground mass (kg)

K_g Ground spring constant (N/m)

D_g Ground damping or dashpot constant (N.s/m)

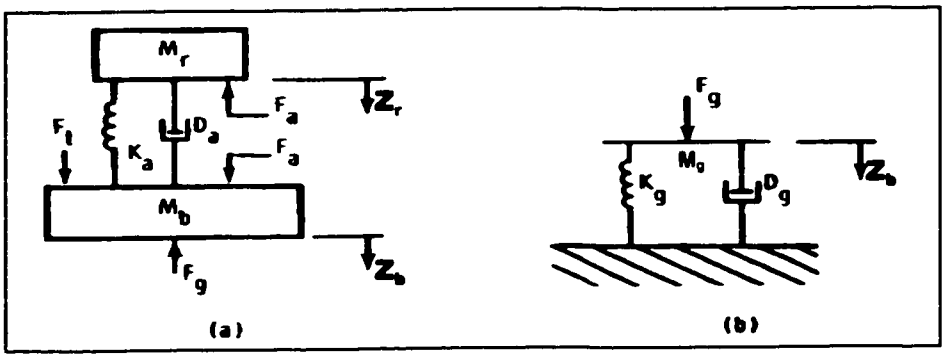

Figure 2.2: a) Vibrator mechanical model b) Mechanical ground impedance model. (Sallas 1984)

The equation of motion for this model can be written as:

$$-F_g = M_r \ddot{Z}_r + M_b \ddot{Z}_b \qquad (2.1)$$

$\ddot{Z}_r$ and $\ddot{Z}_b$ are respectively the second derivatives of reaction mass and baseplate displacements. Two assumptions are made to derive this equation. First is that reaction mass and baseplate act as rigid bodies. Baetan and Ziolkowski (1990) provided a detailed discussion of the error of this assumption, especially with increasing frequency. Second is that the vibrator vehicle is dynamically isolated from the baseplate. This is a reasonable assumption for the frequency range used in hydrocarbon exploration, since a modern

vibrator vehicle is isolated at frequencies above approximately 3 Hz (Sallas, 1984) and its effect on the transmitted signal can be neglected.

Mechanical Ground Impedance Model

Figure 2.2b illustrates the simple mechanical ground impedance model assumed by Sallas and Weber (1982). Earth is represented by a spring constant (K_g) and a damping coefficient(D_g). These two parameters define the interaction between the baseplate and the surface of the earth.

The earth motion equation is obtained by considering the equilibrium of the contributing dynamic forces. The equation includes inertial forces, damping forces, spring forces that are equated to the external force such that:

$$F_g = -(M_g \ddot{Z}_b + D_g \dot{Z}_b + K_g Z_b) \qquad (2.2)$$

Z_b and $\dot{Z}_b$ are respectively the first and second derivatives of the baseplate displacement. M_g is assumed to be equal to zero in the ground model proposed by Lerwill (1981). Nevertheless, there is a mass of earth to be driven that is approximately equal to the mass of the baseplate (M_b) but varies with baseplate and soil properties (Waters, 1981).

The interaction between the vibrator and the earth varies with the earth's physical properties and thus alters the response of the vibrator. Simply, as it pushes against the earth, the vibrator feels the earth response to the applied force through the movements of the baseplate. Therefore, knowing the dynamics of the vibrator, that is the ground force and baseplate accelerations, estimates can be obtained for the underlying earth properties as implied by equations (2.1) and (2.2).

2.1.3 Vibrator Performance Control System

The vibrator performance control system is a real-time feedback system with which each vibrator is equipped. The main function of this system is to compensate for changes in the earth's impedance as the vibrator crosses grounds with different physical properties. There are other factors that alter the transmitted signal, namely the linear and nonlinear effects in the vibrator itself. Plate bending is an example of the vibrator's linear effect. On the other hand, as and example for nonlinear effects, the oscillation force in the hydraulic vibrator is generated by reversing the fluid flow in the drive system by the servo valve. The discontinuity arising when closing of this valve causes discontinuities in the fluid flow and a resulting harmonic distortion in the exerted force. It should be pointed out that the vibrator performance control system is causal and thus the harmonic distortion cannot be removed from the system which means that it would always exist in the emitted signal (Baeten and Ziolkowski, 1990).

The vibrator performance control system varies the amplitude and phase of the drive system's applied force in order to reduce the discrepancy between the feedback signal and the preset signal or pilot. Figure 2.3 provides a simple illustration for the function of the vibrator performance control system. Most of the modern vibrator control systems use the Sallas (1984) phase-locking technique to control the phase and amplitude of the applied force. Measurements made at the reaction mass and baseplate of the vibrator allow determination of the weighted-sum feedback signal, used to estimate the ground force, that is used for comparison with the pilot. The latter is then rectified before it is input to the vibrator drive system. Therefore, the amplitude and the phase of the

exerted force are varied in such a way as to minimize the error between the feedback and pilot signals.

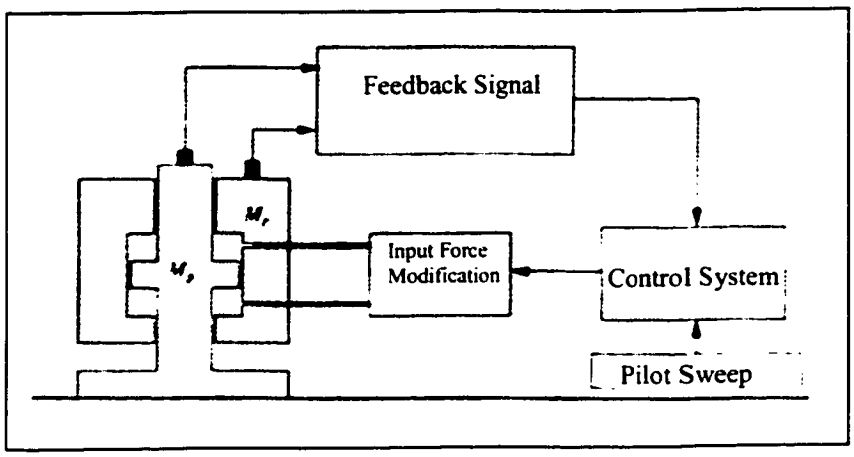

Figure 2.3: Vibrator performance control system schematic diagram. (Redrawn from Baeten and Ziolkowski, 1990)

Sercel VE 432 Vibrator Performance Control System

In the previous discussion, I have considered the vibrator mechanics and the associated earth dynamics and finally the rule of the vibrator control system. In this section I will briefly discuss the Sercel VE 432 vibrator performance control system because the data that will be used later in this study was acquired with this system. There exist other commonly used control systems such as Pelton Advanced V.

Figure 2.4 shows a schematic diagram of the Global Control System (GCS) that depicts the functions of the VE 432 controller. Sercel introduced this controlling methodology in 1988. It uses a single control loop besides the state variable approach for controlling the raw ground force. For comparison, Figure 2.5 shows a schematic diagram of the conventional ground force Phase Locked Loop (PLL) control system. In the main loop of this model the phase comparator is fed with the vibrator signal coming from the

sensors' measurements, compares it with the pilot, and issues a modified signal to change the operating point of the phase shifter.

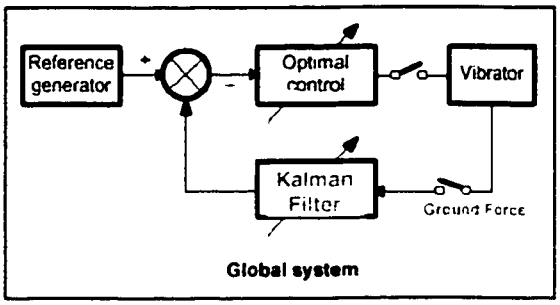

Figure 2.4: Global Control System.

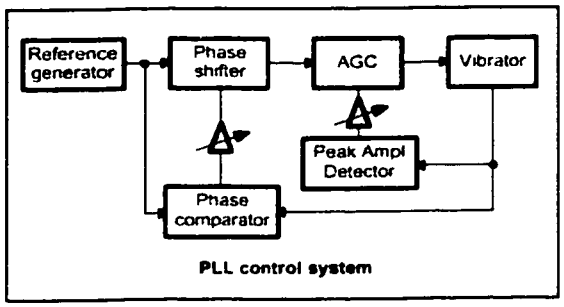

Figure 2.5: Phase Locked Loop.

The VE 432 controller includes an auto-adaptive model and a KALMAN filter. This filter allows computation of the estimated states of the system obtained from measurements and thus takes into account the non-linear effects of the vibrator and the near-surface ground (Baliguet et al., 1992). Therefore, the vibrator and the ground are modeled using the state variables compared to the conventional (PLL) method that provides information only on the control system. Ten estimated state variables are used to drive the system including the shaker components and the ground mathematical model. The KALMAN filter can be considered as a recursive periodic-corrector algorithm implemented for estimating the unknown model internal state variables, given certain measurement signals corrupted by noise. It is different from a sample mean estimator because it is a model-based processor represented by state variables (VE 432 Training Manual, 1999). The concept of vibrator control using the KALMAN filter approach is similar to adaptively compute the parameters of tenth order state equations representing the vibrator-ground model equations and then using these equations to estimate the

unknown internal model state variables, which include the ground force, ground stiffness, and ground viscosity, amongst others.

VE 432 Post Sweep Performance Control Data

The system acquires data from accelerometers mounted at different points of the vibrator and derives quality control data every half a second from the raw ground force and pilot signals. Upon completion of each vibration called "sweep", VE 432 sends back to the recording truck via radio link eight performance control values plus other quality control values such as the positioning. The eight performance control values are:

1. Average absolute phase error values in degrees
2. Maximum phase error in degrees
3. Average distortion in percent
4. Maximum distortion in percent
5. Average fundamental ground force in percent
6. Maximum fundamental ground force in percent
7. Ground viscosity
8. Ground stiffness

The two ground parameters, 7 and 8, are estimated assuming the Sallas (1984) model. The other six attributes are measured to reflect certain criteria of the raw ground force determined using the same model.

The amplitude of the fundamental ground force (AMPL) is given by:

$$AMPL = \sqrt{(\mathrm{Re}\,Peak)^2 + (\mathrm{Im}\,Peak)^2} \qquad (2.3)$$

where

Re Peak is the cross correlation of ground force and reference

Im Peak is the cross correlation of ground force and a 90° shifted reference

The phase (ϕ) is given by:

$$\phi = \tan^{-1} \frac{\text{Im}\, Peak}{\text{Re}\, Peak} \tag{2.4}$$

The distortion (DIST) is calculated as:

$$DIST = \sqrt{\frac{(GroundForce)^2 - (AMPL)^2}{(AMPL)^2}} \tag{2.5}$$

where *GroundForce* is the RMS value of ground force.

2.1.4 Previous Investigations of Vibrator Performance Control Data

Garotta and Marin (1992) attempted with partial success to use the vibrator derived ground parameters: stiffness and viscosity to compensate for the changes in seismic response due to surface coupling conditions. The compensation could be performed at acquisition stage by controlling the vibrator signal, or even at processing stage. The experiment was performed in well and then in surface seismic.

The well experiment was carried out as shown in Figure 2.6a where the vibrator was placed on concrete slab and on pasture (clay) while the receiver was placed at a depth of 150 meters in the well. Figure 2.6b exhibits the amplitude, frequency spectra and ground properties of the experiment. Signal emitted on the pasture is higher in amplitude by 6 dB than on concrete slab while the frequency spectra show that higher frequencies are more transmitted on pasture. Ground stiffness increases by 25 percent on the concrete and the ground viscosity increases by 80 percent on the pasture.

Figure 2.7 illustrates the correlation between elevation and stiffness-to-viscosity ratio (Postel et al., 1996). Good correlation was also obtained between stiffness-to-

viscosity ratio and the RMS amplitude around 200 seconds of the first break stacks as shown in figure 2.8.

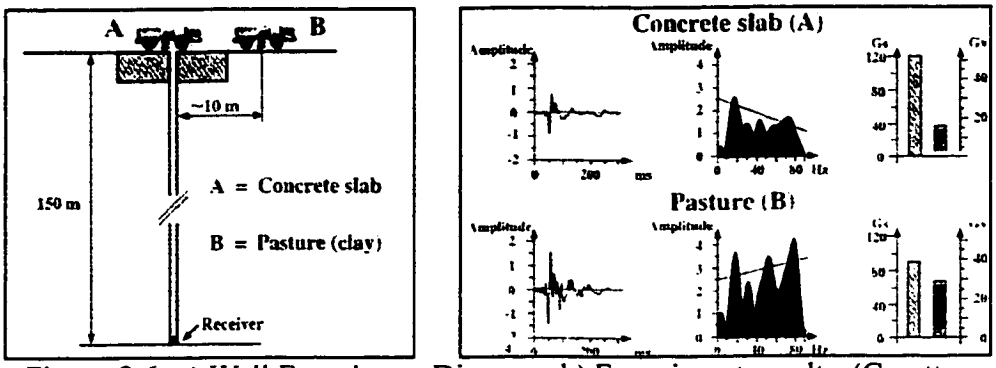

Figure 2.6: a) Well Experiment Diagram, b) Experiment results. (Garotta and Marin, 1992)

As can be concluded from the previous examples, earlier attempts to use vibrator performance control data, particularly ground parameters, concentrated on seismic amplitudes. The applications of these attributes to improving the spatial calculation of a near surface earth elastic property, like V_p is a new idea.

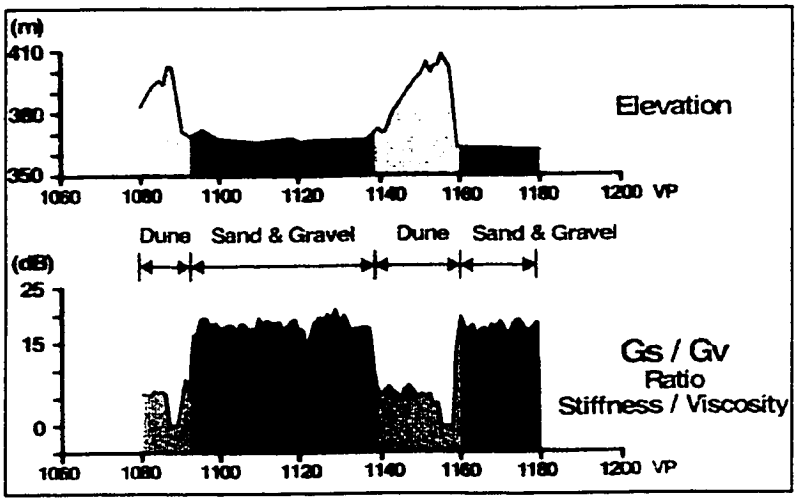

Figure 2.7: Stiffness to viscosity ratio correlation to surface elevation material. (Postel et al., 1996)

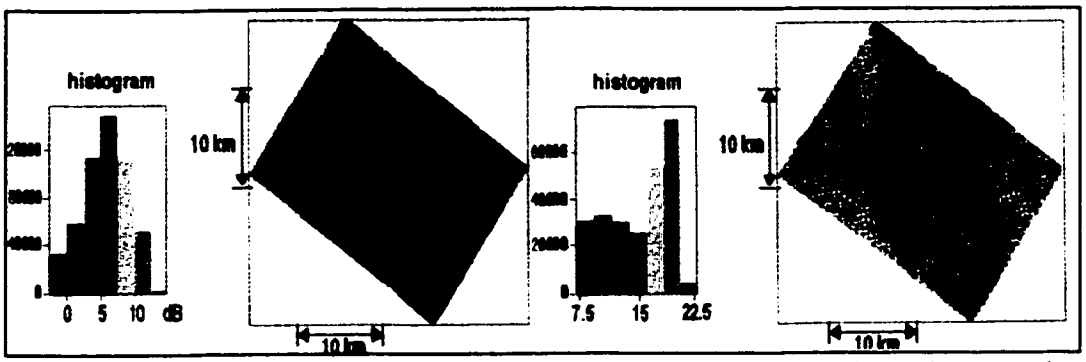

Figure 2.8: a) First break amplitude b) Ground stiffness to viscosity ratio. (Postel et al., 1996)

2.1.5 Vibrator and Earth Models Analogues

The theory of vibrations on the earth surface is well studied in field of civil engineering. Therefore, this already developed framework for the vibration of foundations will be utilized to provide further analytical insights into vibrator and earth mechanical models.

Lumped Mechanical Spring-Dashpot System

The lumped mechanical spring-dashpot system model of the earth is comprehensively discussed in civil engineering classical books, for example (Berg, 1989); (Buchholdt, 1997); (Reynolds, 1981); (Richart et al., 1970). This system is called single degree of freedom system (SDOFS) for forced damped vibrations.

The lumped mass spring-dashpot is an idealized system where the translational displacements are defined and in which the properties of a real elastic body have been lumped. The ground spring constant K_g, which was referred to as ground stiffness is a schematic representation of a linear load-deformation relation of the ground material using a linear force displacement spring. An elastic spring obeys Hooke's law so that the spring force is linearly proportional to the spring deformation. The ground damping

coefficient D_g that is represented by a dashpot is a factor used in dynamic systems to represent energy dissipation (Arya, 1979). Ground damping is referred to as ground viscosity. The force in the dashpot is proportional to the velocity of vibration $\dot{X}_b$. The dashpot force opposes the motion of the mass(M_g). It should be noted that ground damping is not considered to be a result of viscous damping; however, the theory for SDOF systems with viscous damping is an applicable framework for representing the effect of the damping that occurs in the ground material. It is also important to differentiate between vibration velocity Z_b and wave propagation velocity. The latter depends on material properties while the former is a function of the applied stress intensity.

Oscillatory Force Exerted by Rigid Bodies Coupled to Earth Surface

Vertical oscillation of footing resting on the surface of an elastic half-space is the civil engineering analogue of the aforementioned Sallas and Weber model of the vibrator and earth's dynamics. The elastic half-space is defined as a homogeneous, isotropic, and elastic semi-infinite body. The soil is assumed to behave as a nearly elastic medium for small scales of strains (Richart et al., 1970).

Joseph Valantin Boussinesq (1885) provided theoretical formulations for determining stresses at a point within the elastic-half space due to surface static point loads. In 1904 Lamb advanced a theoretical solution for both transient-pulse and steady-state oscillation loadings due to single oscillation force acting on the surface. This vertical oscillating force at the surface is called "dynamic Boussinesq loading". In addition, Lamb discussed the dynamic reciprocity that is extended from Maxwell's law of reciprocal deflections to dynamic conditions. Maxwell's law states that the deflection that occurs at

point 1 in an elastic body caused by a unit value of load at point 2 in the same body is equal to the deflection at point 2 as a result of a unit value of load acting at point 1. Lamb stated that the dynamic reciprocity can be used to determine the dynamic motion within an elastic body resulting from a point load on the surface by using the displacement at the surface caused by an oscillatory point force acting within the body. This conclusion is depicted in Figures 2.9a and 2.9b. Here the vertical displacement at point O within the half-space resulting from the vertical load Q at point O' shown in Figure 2.9a is equal to the vertical displacement acquired at point O' as a result of the vertical load Q at point O as shown in Figure 2.9b.

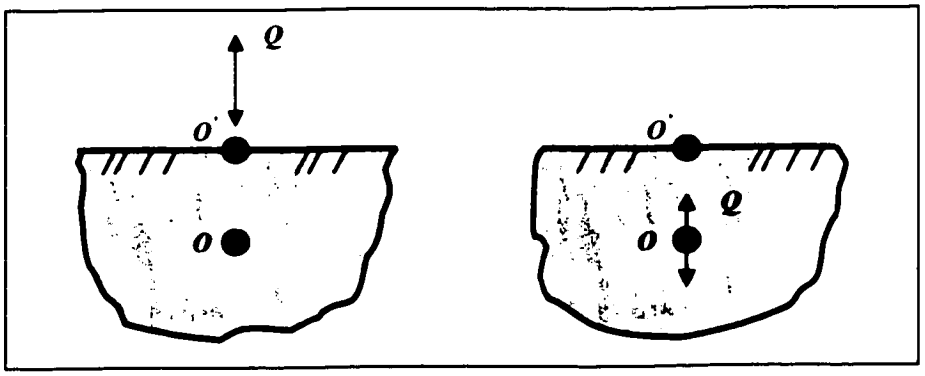

Figure 2.9: Lamb's concept of steady-state or pulse vertical loading at the surface. (Modified from Richart et al., 1970)

The Deutschen Forschungsgesellschaft für Bodenmechanik (DEGEBO) examined the use of mechanical oscillators in the early 1930's to determine the soil physical properties in the field (see Hertwig et al., 1933). As a result of this investigation, Reissner (1936) developed a theory for the dynamic response of a vibrating footing as it was affected by the soil properties. Refer to Richart et al., (1970) for detailed discussions of Reissner's work and some subsequent studies by Quinlan (1953), Sung (1953), Hsieh (1962) and Lysmer (1965). Lysmer (1965) studied the dynamic response of a rigid

circular footing to vertical motion of the model shown in figure 2.10. This model shows a rigid circular footing of radius (r_0) and mass (m) coupled to the elastic half-space and put into oscillation by an external periodic force (Q). The equation of motion of this model can be expressed in a similar form as in Equation (2.2) by replacing (F_g) by (Q) and (M_g) by (m).

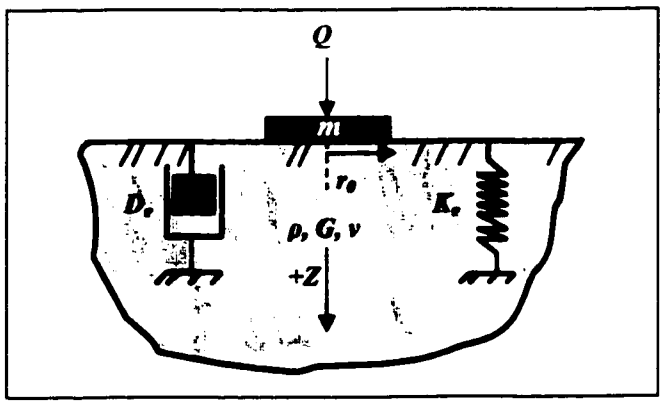

Figure 2.10: Circular body on elastic half-space. (Modified from Richart et al., 1970)

Lysmer (1965) discovered that constant values of K_g and D_g could be used where he related them to properties of the elastic half space. He expressed K_g as:

$$K_g = \frac{4Gr_0}{1-\nu} \tag{2.6}$$

where

G shear modulus

ν Poisson's ratio

and D_g is best fitted by:

$$D_g = \frac{3.4r_0}{(1-\nu)}\sqrt{\rho G} \tag{2.7}$$

where

ρ mass density

Hence, Lysmer's work establishes the link between the elastic half-space theory and the mass-spring-dashpot system. The problem of a vertically oscillating rigid rectangular body coupled to the elastic half-space has also been studied. It has been concluded that for practical purposes, the Lysmer's solution can be utilized for rectangular footing provided that the ratio between the length and the width of the footing does not exceed two (Richart et al., 1970). The equivalent r_0 for square or rectangular plates can be calculated by equating the area to that of a circle such that:

$$r_0 = \sqrt{\frac{4cd}{\pi}} \tag{2.8}$$

where c and d are respectively the plate length and width.

Relation Between Ground Parameters and V_p

As the goal of this research calls for, a relation between compression wave propagation velocity (V_p) and ground parameters: stiffness (K_g) and viscosity (D_g) will be investigated in this section.

Poisson's ratio which is a parameter in the (K_g) and (D_g) equations can be expressed in terms of V_p to V_s (shear wave propagation velocity) ratio so that:

$$\nu = \frac{0.5 - (V_s / V_p)^2}{1 - (V_s / V_p)^2} \tag{2.9}$$

Also, the shear modulus (G) can be expressed in terms of mass density and (V_s) by:

$$V_s = \sqrt{\frac{G}{\rho}} \tag{2.10}$$

Substitution of Equations (2.9) and (2.10) into (2.6) and (2.7) gives:

$$K_g = 8r_0\rho(V_s^2 - \frac{V_s^4}{V_s^2}) \tag{2.11}$$

$$D_g = 6.8r_0\rho(V_s - \frac{V_s^3}{V_p^2}) \tag{2.12}$$

It is obvious from Equations (2.11) and (2.12) that (K_g) and (D_g) depend on 3 inter-dependent parameters, V_p, V_s and ρ. Therefore, relating each of the ground parameters independently to the P-wave wave velocity is not possible without knowledge of a further parameter.

The critical damping for vertical oscillation in viscously damped systems is defined such that the free displacement reaches equilibrium without oscillation. It is given by:

$$D_c = 2\sqrt{K_g m} \tag{2.13}$$

The critical damping is expressed in terms of D_g and a dimensionless mass ratio such that:

$$\frac{D_g}{D_c} = \frac{0.425}{\sqrt{B_z}} \tag{2.14}$$

B_z is the dimensionless mass ration introduced by Lysmer given by:

$$B_z = \frac{1-\nu}{4}\frac{m}{\rho r_0^3} \tag{2.15}$$

Knowing both K_g and D_g, the value of $(1-\nu)/\rho$ can be determined from Equation (2.12):

$$\frac{\rho}{1-\nu} = \frac{D_g^2}{2.89K_g r_0^3} \tag{2.16}$$

Substitution of $(1-\nu)/\rho$ in any of the Equations (2.6) or (2.7) leads to the determination of V_s. The previous derivation shows that both K_g and D_g can be used to

eliminate the dependence on density ρ and Poisson's ratio v and thus computing V_s. Equation (2.9) relates V_s and V_p to Poisson's ratio. An idealized case is shown in Figure (2.11). In general, Poisson's ratio for cohesionless soils ranges from 0.25 to 0.35 and for cohesive soils from 0.35 to 0.45 (Richart et al., 1970). The corresponding V_p to V_s ratio will vary from 1.73 to 2.08 for cohesionless soils and from 2.08 to 3.32 for cohesive soils. The median of these ratios is 2.3. This value is a reasonable approximation of the V_p to V_s ratio for the near surface materials that will be sensed by the vibrator as not all of these materials will be cohesive, or cohesionless, but rather a combination of these two. Therefore, V_s obtained from K_g and D_g will be correlated with V_p measured from upholes, seeking a linear relation.

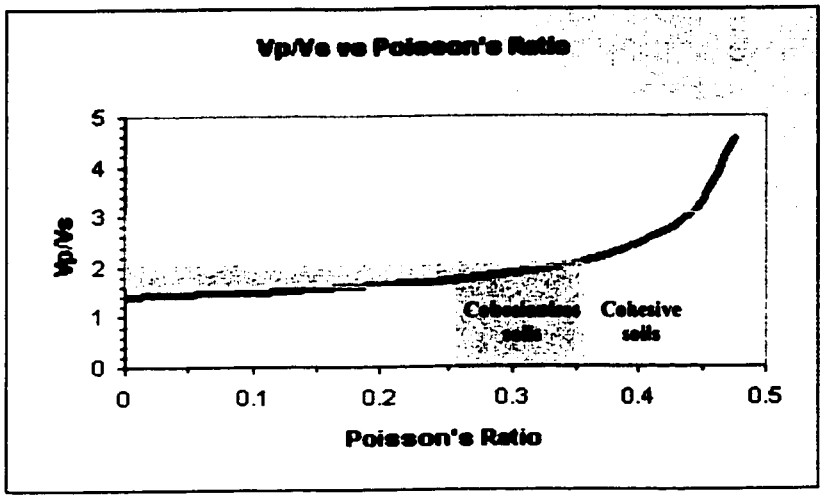

Figure 2.11: Idealized Poisson's ratio and (V_p/V_s) curve.

Depth of Penetration

In the preceding discussion, shear wave velocity was related to the elastic half-space stiffness and viscosity. However, the depth of penetration did not appear in any of the analytical derivations because these all assumed an elastic half-space. It is well

established that the earth's surface is not really elastic but more complicated in which elastic properties vary with depth. Therefore, it is important to know the thickness of the earth surface that these ground parameters represent.

A vertically oscillating energy source coupled to the surface of an elastic half-space generates three types of elastic waves: compression, shear, and Rayleigh waves. Miller and Pursey (1956) showed that for an oscillating circular energy source on the half-space, for Poisson's ratio of ¼, the energy distribution is 6.9%, 25.8, and 67.3 respectively for compression, shear, and Rayleigh waves. Hence, most of the displacements occurring at the vibrator baseplate as a reaction to ground response are due to the vertical component of the Rayleigh waves.

Rayleigh waves penetrate a depth of the half-space which equals one wavelength. Thus it is reasonable to assume that the Rayleigh waves carry information about the properties of half-space close to a depth equal to one-half wavelength (Richart et al., 1970). The depth of penetration depends on frequency, the higher it is the shallower the penetrated depth. Richart et al, (1970) showed examples of measuring shear wave velocity in the field from Rayleigh waves penetrating up some 170 ft depths.

The vibrator source used in hydrocarbon exploration emits energy for a certain period of time, and with linearly varying frequency. Consequently, different Rayleigh wavelengths are generated having different velocities. This phenomenon, called dispersion, is beyond the scope of this study. Instead, an experimental approach will be used in this study to geostatistically correlate near-surface compressional wave velocities measured from upholes with vibrator performance control data obtained during the

acquisition of 3D seismic surveys. If a strong correlation would be observed using the experimental data, this will give impetus for further theoretical studies.

2.1.6 The Study of Vibrator Control Data Relationships to Measured Near-surface V_p Velocities

Based on the previous discussion, vibrator performance control data can be defined as measurements produced by the seismic vibrator control system at the end of each vibration that compare the applied ground force and the pilot reference, and determine the coupling between vibrator and ground.

In Section 2.1.5 an analytical relation was established between the ground parameters and the compression wave velocity. However, no analytical relation can be established between the six other performance control values and V_p. Nevertheless, a numerical relation will be sought based on observations of the response of these attributes to different ground materials.

Schrodt (1987) confirmed experimentally that amplitude and phase control and suppression of vibrator harmonic distortion are more severe on solid ground. The study showed that these problems are of greater magnitude on frozen tundra than on soils. The harmonic distortion is attributed to different factors including the discontinuously closing vibrator drive system, earth response to large dynamic loading, and feedback controlling system (Seriff and Kim, 1970). When vibrating on stiff grounds, vibrator has to exert more energy in order not to reduce output levels (Brown and Moxley, 1964). Based on these observations, proportional relations will be investigated between distortion and maximum fundamental ground force and V_p. The fact that the vibrator control system

minimizes the differences between the amplitude and phase of the emitted signal, and those of the theoretical signal may eliminate the phase and the average fundamental ground force because they change in a very narrow range. Thus it is reasonable to hypothesize that many of the measured vibrator performance data may be correlated with near surface ground properties, including ground stiffness and viscosity. Due to the previously discussed relationships, we may also expect a correlation with P-wave velocities. Therefore, the geostatistical studies will also look for correlations between V_p velocities, estimated ground stiffness and viscosity, and additionally several other types of vibrator performance data.

2.2 V_p Velocity Determination from Uphole Survey

P-wave velocity of the near surface layers can be measured directly by using an uphole survey. An uphole survey is performed by drilling a borehole to depths of 10's to 500 meters and using a seismic source and receiver to determine V_p by placing the source on the surface and the receiver in the borehole (or vica versa), and measuring the time taken by the sound wave to travel from source to receiver. Knowing the time T and the depth d, V_p can be determined by:

$$V_p = d / T \tag{2.17}$$

The same procedure is repeated at different depths to the bottom of the well in order to construct a time versus depth function. This function assists in forming a velocity model versus depth or determining the different layers velocity. Figure 2.12 explains the process of the uphole survey and the obtained information.

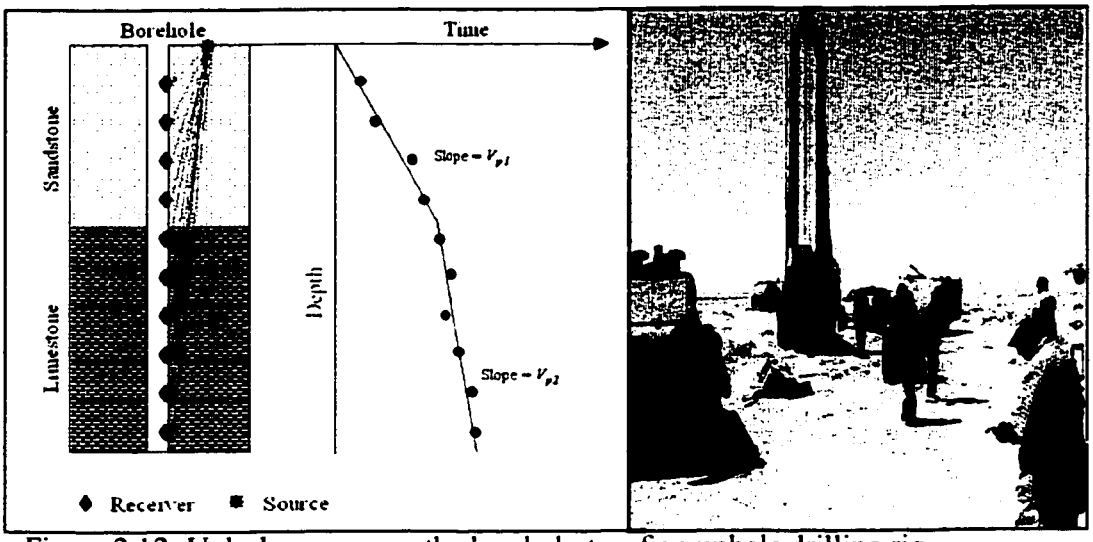

Figure 2.12: Uphole survey method and photo of an uphole drilling rig.

Normally, the source or receiver whichever is placed on the surface is offset from the borehole by a certain distance (x). Besides, the elevation at the well might be different from the elevation of the source or receiver point. Therefore, a geometric correction must be applied to the recorded times to obtain vertical travel times. Before these geometric corrections, another correction is normally applied to remove recording system delays (Cox, 1999). The geometric correction from recorded time t to vertical time T for the case of constant surface elevation of both borehole and source is illustrated in Figure 2.13 and can be expressed as:

$$T = t\frac{z}{(z^2 + x^2)^{1/2}} \tag{2.18}$$

There are other indirect methods to determine the near surface layers velocity model. These are refraction and shallow reflection surveys. These measurements for near surface properties determination are conducted separately from the surveys directed towards imaging deep layers. These refraction and shallow reflection surveys normally

require further constraining factors to validate their results. Upholes are used to perform this task.

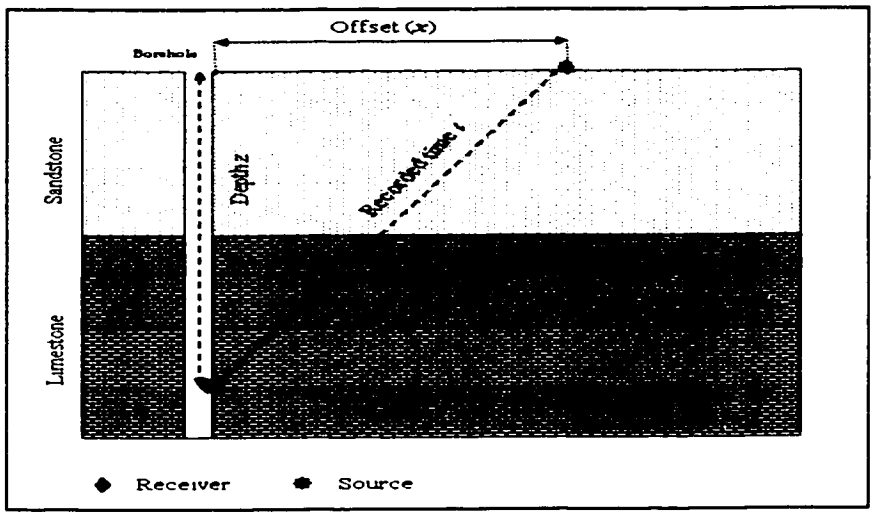

Figure 2.13: Schematic diagram of uphole vertical time geometric correction.

Refraction and shallow reflection surveys are used to interpolate between sparsely located upholes for improving the near surface velocity model. Velocity of the near surface layer is estimated from the direct arrivals from these two techniques. Sometimes other kinds of data are used for interpolation, such as ground penetrating radar (GPR) or resistivity. In short, these techniques are good aids for interpolation between upholes; however, they add an extra cost component to the survey.

2.3 Geostatistics Review

2.3.1 Introduction

Geostatistics is a branch of statistics that honors the continuity exhibited by random variables in space or time. Successful use of statistical methods in hydrocarbon prospecting requires integration of statistical concepts with geology.

Early development in geostatistics started about four decades ago. It has been used to describe spatial patterns and to interpolate between sampled data points. Geostatistics is becoming routinely used in hydrocarbon industry to predict reservoir parameters based on the available limited number of wells. Besides of describing spatial and temporal patterns, it is a good tool for multi-scaled data integration. The success rates of this tool highly depend on the structure of the data.

2.3.2 Univariate Statistics

The characteristics of a single variable data set can be summarized by certain numbers that are called univariate statistics. The latter are obtained by performing some arithmetic operations with samples of the variable. These arithmetic operations include measures of location, spread or dispersion, and shape. We can refer to (Isaaks and Srivastava, 1989); (Wheeler, 1995); (Marsal, 1987) for more elaborate discussions of univariate statistics.

The location measures consist of the mean, mode, and median. The mean is given by:

$$m = \frac{1}{n}\sum_{i=1}^{n} x_i \tag{2.19}$$

where x_i is a data sample and n is the number of samples. The median is defined by the value below and above which fifty percent of the data samples occur provided that the data set is sorted in an increasing order. It is determined by:

$$M = x_{\frac{n+1}{2}} \text{ if } n \text{ is odd and } M = \frac{1}{2}(x_{\frac{n}{2}} + x_{\frac{n}{2}+1}) \text{ if } n \text{ is even} \tag{2.20}$$

The mode represents the most frequently occurring value within a data set. For normal distributions, these three location measures are equal.

Measures of spread or dispersion include variance, standard deviation (sigma), and interquartile range. The variance is the average squared difference between the data samples and their mean which is given by:

$$\sigma^2 = \frac{1}{n}\sum_{i=1}^{n}(x_i - m)^2 \tag{2.21}$$

Standard deviation is the square root of the variance. It is more meaningful because it has the same units as the distribution measures (Isaaks and Srivastava, 1989). The interquartile is the difference between the upper (below which 75% of the data samples fall) and the lower (below which 25% of the data samples fall) quartiles of a data set.

It is well established that three-sigma limits provide effective bounds for most real world data. For most distributions in geophysical practice, 60% to 75% of the data is located within a range of one standard deviation from both sides of the mean. And about 90% to 98% of the data is located within a distance from either side of the mean equals to two standard deviations. Within a distance equals to three standard deviations from both sides of the mean nearly 99% to 100% of the data is located (Wheeler, 1995).

Coefficient of skewness, kurtosis, and coefficient of variation measure the shape of the data distribution. Coefficient of skewness measures the symmetry of a data set and it is written as:

$$Skewness = \frac{1}{n\sigma^3}\sum_{i=1}^{n}(x_i - m)^3 \tag{2.22}$$

A positive coefficient of skewness means that more values higher are than the mean. This can also be inferred from the measures of location, if the mean is greater than the median, and the latter is greater than the mode. The opposite is true for negatively skewed data. Kurtosis primarily characterizes the amount of data in the extreme tails of the distribution or histogram. The greater the relative proportion of the data in the extreme tails, the greater the kurtosis. Kurtosis is the fourth moment around the mean divided by the squared variance such:

$$Kurtosis = \frac{1}{n\sigma^4}\sum_{i=1}^{n}(x_i - m)^4 \tag{2.23}$$

The benchmark for comparison is the normal distribution whose kurtosis is equal to 3. The coefficient of variation is given by the ratio of the standard deviation to the mean such that:

$$CV = \frac{\sigma}{m} \tag{2.24}$$

It does not change with linear transformation of the data. It is mainly calculated for data sets with only positive samples. A coefficient of variation greater than one reveals the presence of erratic high sample values.

2.3.3 Semi-variogram

The semi-variogram $\gamma(h)$ is the basic tool to describe the spatial or temporal correlation between nearby data samples as function of the separation vector h. Mathematically, it is half the average squared difference between data pairs separated by a vectorial or temporal distance h. It is calculated as:

$$\gamma(h) = \frac{1}{2N(h)} \sum_{i=1}^{N(h)} (U(x_i) - U(x_i + h))^2 \qquad (2.25)$$

where:

$N(h)$ is the number of data pairs separated by h

h vectorial or temporal distance

$U(x_i)$ are the data values

The semi-variogram $\gamma(h)$ typically increases as h increases until it reaches a plateau. Refer to Clark (1979) for detailed description of semi-variogram calculation.

Semi-variogram Model Parameters

The semi-variogram model parameters (Figure 1.14) include the nugget (C_0), sill (C_0+C), and the range (a). The nugget indicates the variability at small h's and the analysis errors. Sill measures the average half squared difference between data pairs. When the semi-variogram reaches its sill, this means that there is no more correlation between sampled points. It should be pointed out that not all semi-variograms reach a sill: they may keep increasing with distance which is an aspect that distinguishes semi-variogram from covariance which is limited and exists for stationary variables only (Armstrong, 1998). The distance or time beyond which data points behave as if they were

independent is called range. Normally there exists a correlation between data points separated by distances or times less than the range.

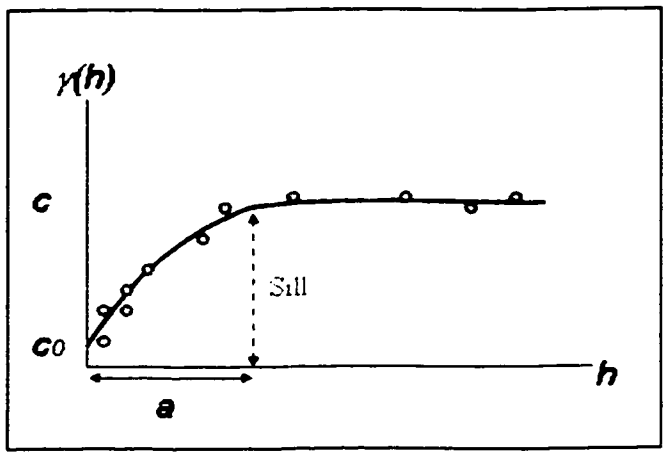

Figure 2.14: Semi-variogram model parameters.

Directional Variogram and Anisotropy

The semi-variogram is usually calculated in different directions to detect anisotropy in the data. Therefore, it is a function of the length of distance vector and its orientation. Semi-variances are plotted against *h* values to construct the experimental semi-variogram.

If a semi-variogram behaves similarly in all directions, it is referred to as isotropic, otherwise it is anisotropic. There are two kinds of anisotropy: geometric anisotropy and zonal anisotropy. The former is normally depicted when semi-variograms exhibit different ranges in different directions while maintaining nearly equal sill value. The zonal anisotropy, on the other hand, results if the sill values are not the same in all directions. This can exist for example in the vertical direction when dealing with horizontal strata as there is more variation between strata than within them (Armstrong, 1998). See for example Kitanidis (1997) and Goovaerts (1997) for further description and examples of anisotropy.

Experimental Semi-variogram Fitting

A mathematical expression, called semi-variogram model, is fitted to the experimental variogram to determine its parameters. Once this model is obtained, it can be used to determine unsampled data points within the vicinity of existing samples through an estimation procedure called kriging. There are different semi-variogram models such as spherical, exponential, power, Gaussian, cubic, fractal, and compound or nested. Data samples behavior determines which model should be used (Armstrong, 1998); (Goovaerts, 1997). If nested behavior is exhibited by the calculated semi-variograms, this means that there are more than one processes in the system operating at different scales. Nested models have more than one values for the range and sill.

In practice, the form of the analytical fitting of the model does not greatly matter provided that the major characteristics of the phenomenon are honored. These characteristics are ordered according to their importance as nugget effect, slope at the origin, range, sill, and anisotropy (Armstrong, 1998). The range is visually assessed, while the sill is set where the variogram reaches a plateau. The sill is normally equal to the variance; however, it may vary due to the presence of long range trends. Changes in variogram curvature indicate the presence of more than one ranges. Finally, anisotropy can be evaluated by comparing variograms calculated in different directions.

2.3.4 Kriging

Kriging is an estimation procedure named after D. G. Krige, a South African engineer who developed the first application of geostatistics in Witwaters sand gold mines (Armstrong, 1998). Kriging is a local estimation technique that provides unbiased

estimates with minimum variance. It is also known as BLUE (Best Linear Unbiased Estimator) that provides optimal interpolation.

Kriging depends on the spatial correlation or variability and data configuration but not on data values. It utilizes the information obtained from the semi-variogram to find an optimal set of weights for estimating unsampled points in space or time. Thus the estimate at a point X in space or time is given by:

$$U_0 = \sum_{i=1}^{n} \lambda_i u_i \tag{2.26}$$

U_0 is the point in time or space to be estimated

λ_i is the weight given for sampled point u_i

The optimal set of weights is determined by solving a set of linear equations with coefficients that depend on the semi-variogram and the sampled data values. The set of weights is calculated in the kriging system to ensure that estimate is unbiased and that the estimation variance is minimal. The kriging weights are found from the following system of equations:

$$\begin{bmatrix} \gamma_{11} & \gamma_{12} & \cdots & \gamma_{1n} & -1 \\ \gamma_{21} & \gamma_{22} & \cdots & \gamma_{2n} & -1 \\ \vdots & \vdots & \vdots & \vdots & \vdots \\ \gamma_{n1} & \gamma_{n2} & \cdots & \gamma_{nn} & -1 \\ 1 & 1 & \cdots & 1 & 0 \end{bmatrix} \begin{bmatrix} \lambda_1 \\ \lambda_2 \\ \vdots \\ \lambda_n \\ \mu \end{bmatrix} = \begin{bmatrix} \gamma_{u1} \\ \gamma_{u2} \\ \vdots \\ \gamma_{un} \\ 1 \end{bmatrix} \tag{1.27}$$

γ_{ij} is the semi-variogram value for the respective data samples |j-i| distance units apart

μ is Lagrange multiplier

γ_{un} is the semi-variogram value between estimated location or time U and sampled data values

λ_n is the unknown weight

The kriging system (2.27) defines Ordinary Kriging, which is used as a point estimator. However, it can be used in a similar form to estimate the average value over an area, when it is called Block Kriging. Other important kriging type is Co-Kriging, which is used to integrate different related data. Sometimes, one variable may not have been adequately sampled to provide estimates of good precision. Considering another variable that is sufficiently sampled and has a spatial or temporal correlation to the variable of interest can augment the precision.

2.3.5 Integration of Secondary Information

Improvements in estimating unsampled spatial or temporal points are obtained when the primary measurements are integrated with related secondary attributes. In practice, the primary measurements are sparsely sampled compared to the densely sampled secondary information. There are different forms of kriging that allow performing this task. Among these are kriging with strata, simple kriging with varying local means, kriging with an external drift, and cokriging. The latter will be discussed in this section because it is the primary tool that will be utilized for data integration in this research. The other three methods are comprehensively explained in Goovaerts (1997)

The spatial or temporal cross correlation between primary and secondary data is explicitly accounted for when non-exhaustive secondary data is integrated using cokriging. The general form of cokriging of two variables is given by:

$$U_0 = \sum_{i=1}^{k} \lambda_i u_i + \sum_{j-1}^{l} \beta_j v_j \qquad (2.28)$$

where

U_0 estimated value of U at location 0

u_i and v_j respectively primary and secondary variables

λ_i and β_j cokriging weights respectively for the primary and secondary variables

k and l number of primary, respectively secondary, samples in nearby locations

The cokriging is a linear combination of primary and secondary data. The cokriging weights must meet two criteria in order to provide unbiased estimations and minimum cokriging error variances. These two conditions are satisfied if the primary weights add up to 1 and the secondary weights add up to 0 (Isaaks and Srivastava, 1989):

$$\sum_{i=1}^{k} \lambda_i = 1 \qquad \text{and} \qquad \sum_{j=1}^{l} \beta_j = 0 \qquad (2.29)$$

There are different forms of cokriging, for instance, simple cokriging, ordinary cokriging, and collocated cokriging. Simple cokriging is thoroughly discussed in (Goovaerts, 1997). It differs from ordinary cokriging in the assumption that the local means of both primary and secondary variables are known and constant in the entire area of interest.

Ordinary Cokriging

Ordinary cokriging takes into consideration local mean variations of the primary and secondary variables. This is achieved by limiting the stationarity of primary and secondary variables to local vicinity centered on the location being estimated. The ordinary cokriging is written as:

$$U_0 = \sum_{i=1}^{k} \lambda_i u_i + \sum_{j-1}^{l} \beta_j v_j + \lambda_{m1} m_1 + \beta_{m2} m_2 \qquad (2.30)$$

where

m_1 and m_2 are respective means of primary and secondary variables within a local vicinity

λ_{m1} and β_{m2} respectively are weights of primary and secondary variables within a local vicinity

The weights of the primary and secondary means are given by:

$$\lambda_{m1} = 1 - \sum_{i=1}^{k} \lambda_i \quad \text{and} \quad \beta_{m2} = -\sum_{j=1}^{l} \beta_j \qquad (2.31)$$

If m_1 and m_2 are not known, they can be eliminated by assigning their respective weights to zero. This means that the primary and secondary weights are limited to the conditions of Equation (2.29). This reduces the ordinary cokriging equation to the form of Equation (2.28).

The ordinary cokriging system can expressed, like kriging, in terms of stationary auto and cross semi-variograms, yet in this case, for both the primary and the secondary data. This system consists of linear equations that are solved to determine the weights of primary and secondary data and then use them to derive the estimation according to Equation (2.30). The ordinary cokriging system is given by:

$$\left.\begin{aligned}
&\sum_{a=1}^{k}\lambda_a\gamma_{ia}+\sum_{b=1}^{l}\lambda_b\gamma_{ib}+\mu_1=\gamma_{ui} \quad \text{for } i=1,\cdots,k\\
&\sum_{a=1}^{k}\lambda_a\gamma_{ja}+\sum_{b=1}^{l}\lambda_b\gamma_{jb}+\mu_2=\gamma_{uj} \quad \text{for } j=1,\cdots,l\\
&\sum_{a=1}^{k}\lambda_a=1\\
&\sum_{b=1}^{l}\lambda_b=0
\end{aligned}\right\} \qquad (2.32)$$

μ_1 and μ_2 are the Lagrange multipliers of the respective primary and secondary variables. As can be inferred from the above system, the more samples are included in the estimation of a particular point the more time consuming the computation would be. This system can be expressed in matrix form similar to the ordinary kriging form of equation (2.27).

Collocated Cokriging

Collocated cokriging is introduced to avoid instability of the cokriging system when dealing with a secondary variable that is exhaustively sampled. This is attributed to the aspect that densely sampled secondary data have greater correlation at closer distances than the sparsely sampled primary data. Also the collocated secondary point at the location being estimated for primary masks the influence of farther secondary data points (Goovaerts, 1997).

Considering only the collocated secondary data point, the collocated ordinary cokriging is written with only one constraint that the weights sum up to 1 such that:

$$U_0 = \sum_{i=1}^{k} \lambda_i u_i + \lambda_2 (v - m_2 + m_1) \text{ and } \sum_{i=1}^{k} \lambda_i + \lambda_2 = 1 \qquad (2.33)$$

If the primary and secondary means (m_1 and m_2) are not equal, they must be scaled to ensure unbiasedness. As in the case of ordinary cokriging, the collocated ordinary cokriging system can be written as:

$$\left.\begin{aligned} &\sum_{a=1}^{k} \lambda_a \gamma_{ia} + \lambda_2 \gamma_{ui} - \mu = \gamma_{ui} \qquad \text{for } i = 1,\ldots,k \\ &\sum \lambda_a \gamma_{ua} + \lambda_2 \gamma_{22}(0) + \mu = \gamma_{21}(0) \\ &\sum_{a=1}^{k} \lambda_a + \lambda_2 = 1 \end{aligned}\right\} \qquad (2.34)$$

It is obvious from system (2.34) that when dealing with similar estimation parameters, collocated ordinary cokriging takes less computation time than the ordinary cokriging.

CHAPTER 3

STUDY AREA GEOLOGY AND DATA ANALYSES

3.1 Area Geology

3.1.1 Geomorphology

The study area represents a hilly terrain dissected by shallow wadis with areas covered by sand and gravel sheets. The geomorphic features of the study area are depicted in Figure 3.1. This figure shows locations for photographs and samples that were acquired during a site visit conducted to become more acquainted with the surface geomorphic features and the lithostratigraphic units of the area of interest. Some of these photographs will be presented in this section and the rest in Appendix I. The topography of this area varies from 120 to about 340 meters above mean sea level (MSL) as shown in Figure 3.2. The high elevations characterize the hills that exist in the southern and western parts of

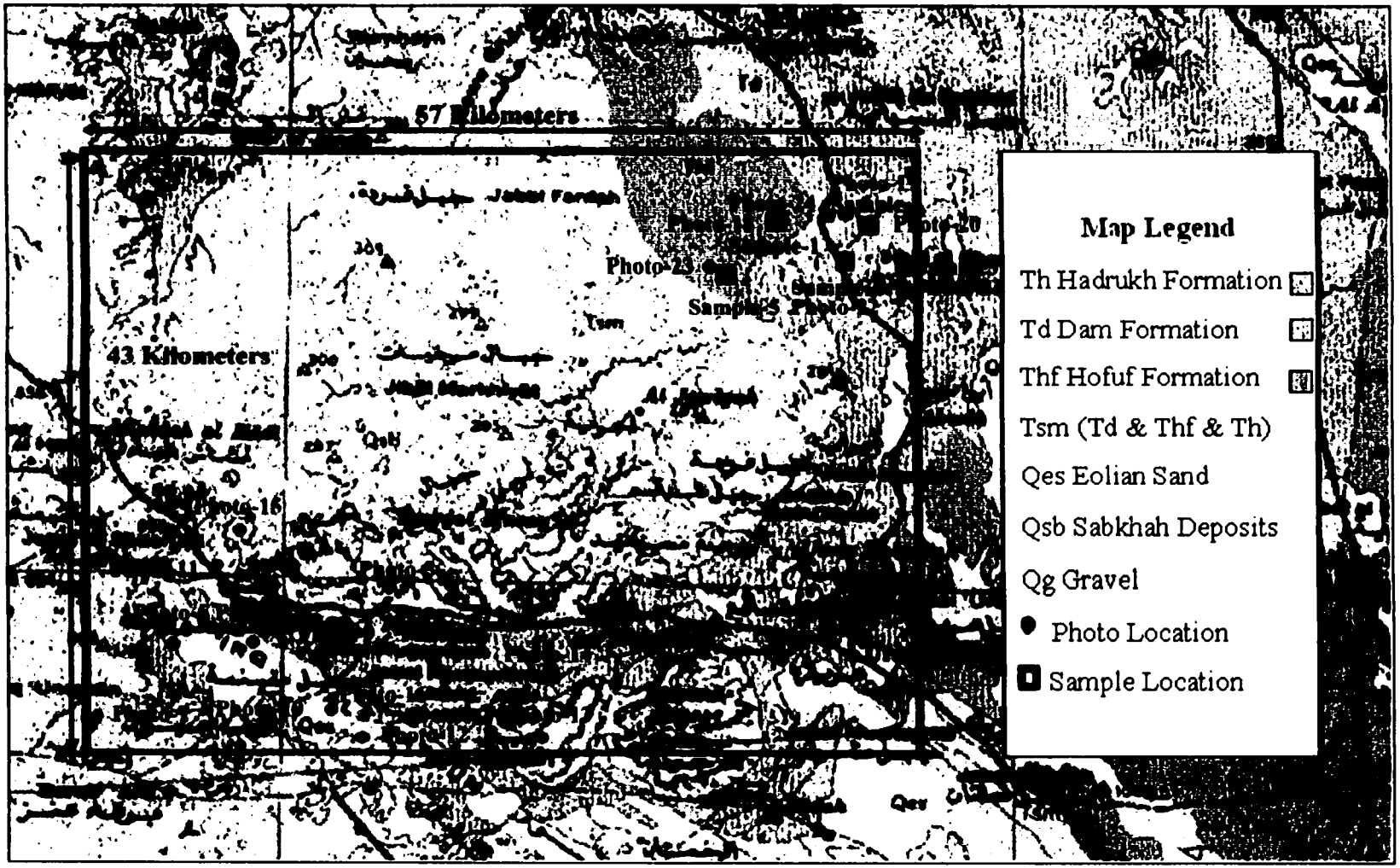

Figure 3.1: Area surface geology. (from the Geology of the Western Persian Gulf Quadrangle, Kingdom of Saudi Arabia, by Steinke et al., 1958)

this region (Figure 3.3). The central and the southern hills are separated by a wadi or dry water course (Wadi and Najabiyah). The depression of this wadi extends to the east and north of the study area where it exposes different lithostratigraphic units. Another depression is located in the northwestern corner (Batn Sabsab) of the study area.

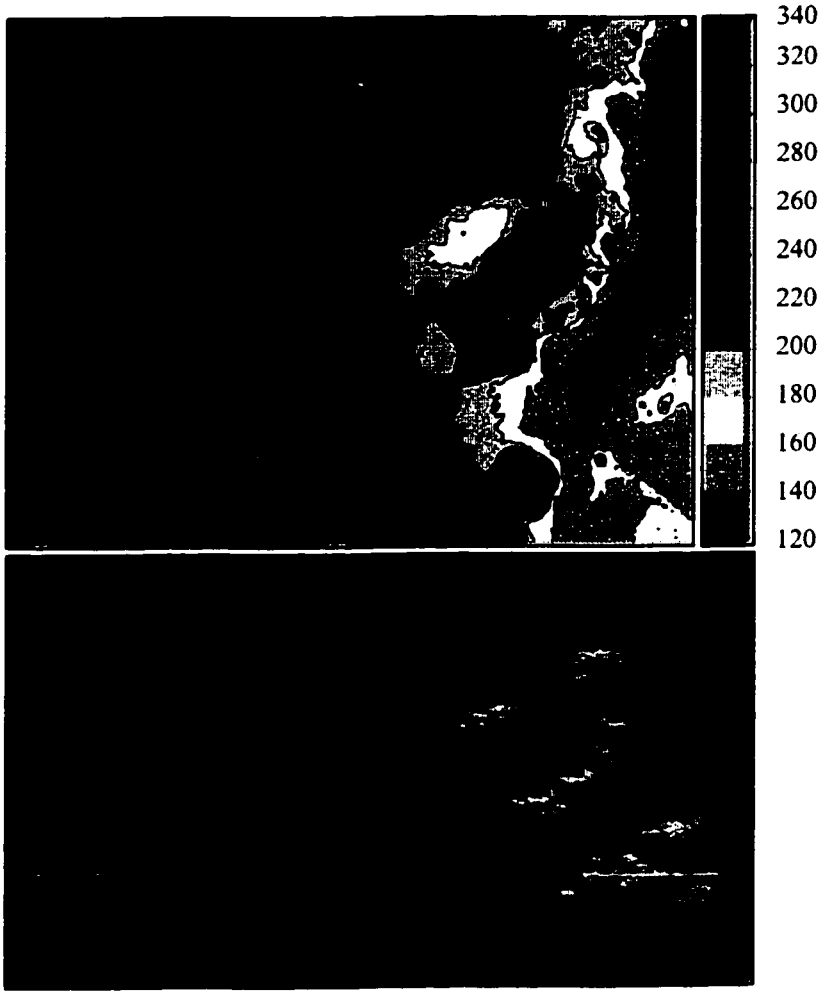

Figure 3.2: 2D and 3D views of the area elevation above MSL, contour interval is 20 meters.

Some undulating eolian sand sheets are also present in the study area. The greater sand bodies exist in the south western part. These sand sheets include irregular surface

covered with bush and grass (Figure 3.4). Relatively large areas are flat and floored with thin layers of gravels (Figure 3.5).

Figure 3.3: Photograph No. 1 exhibiting some hills.

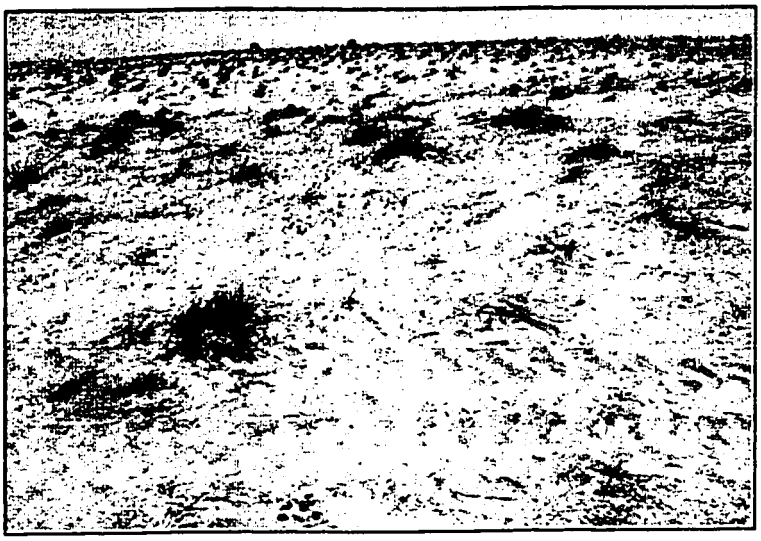

Figure 3.4: Photograph No. 16 showing sandy surface with bush.

Sabkhahs or salt flats also exist in the southeastern part of the study area, yet their arial extents are small compared to other features. The major sabkhah is located in the central eastern part. These sabkhahs are inland and they are genetically different from

coastal ones. They are filled with silt, clay, muddy sand, gypsum, and anhydrite. Normally, salt covers the surface of these sabkhahs. It should be noted that vibroseis seismic surveys cannot be performed on sabkhahs because they are normally wet and thus cause vibrator sinking.

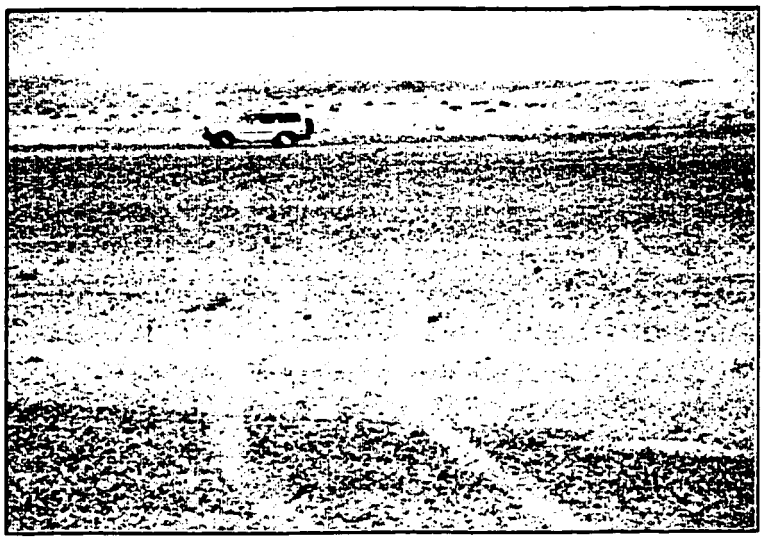

Figure 3.5: Photograph No. 16 showing sandy surface with bush

3.3.2 Surface Geology

The surface geology of the study area exhibits, in some parts, three distinct formations. These are respectively, from the oldest, Hadrukh Formation, Dam Formation, and Hofuf Formation (Figure 3.6) which form the divisions of the Neogene sea level fluctuations. Towards the western interior of this area, the marine layers of the Dam Formation intercalate with the other two continental formations and become thin until they disappear. The divisions of the Neogene no longer apply towards the west where surface rocks are undifferentiated. Such deposits are marked 'Tsm' representing Tertiary continental sandstone, marl, and limestone (Whybrow et al., 1987). Figure 3.6 shows a

schematic diagram of the main lithostratigraphic units interaction within the area of interest. The 'Tsm' represent the majority of the study area.

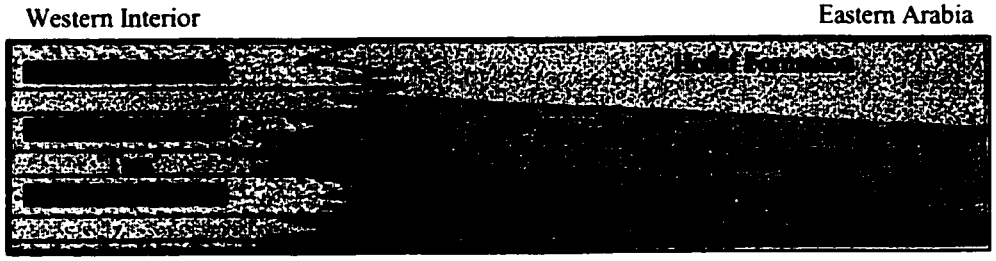

Figure 3.6: Schematic diagram showing the interaction between areal lithostratigraphic units.

Hadrukh Formation

The Hadrukh Formation was named by Steinke and Koch for the type locality at Jabal al Haydruk (lat. 27°04′36′′ N, long. 49°11′24′′ E) where about 51.5 meters of the upper part of this formation crops out (Powers, 1968). The Hadrukh Formation appears on a long band parallel to the Arabian Gulf coast from the northern border of Saudi Arabia to about latitude 26°30′ N to the south with some scattered patches around Abqaiq (Al-Sayari and Zötl, 1978). This band extends about 100 kilometers from the coast due west with some outliers up to 200 kilometers inland. The thickness of this formation varies from 20 to 120 meters (Whybrow et al., 1987). It is about 20 meters in the Abqaiq- Al-Qatif region with a northwesterly increase up to 120 meters around Abu Hadriyah (Powers, 1968).

The age of the Hadrukh Formation is believed to be of Lower Miocene to early Burdigalian (23.7 to 20 Ma) (Weijermars, 1999). It is contemporaneous with the Ghar Formation in Kuwait and south Iraq and, its equivalent Ahwaz Sandstone in Iran (Powers, 1968).

The Hadrukh Formation is overlain by marine deposits of the Dam Formation and it unconformably overlies non-sandy marine Eocene limestone of the Dammam Formation. The Hadrukh Formation is mostly continental except in some areas where few thin layers in the top contain poorly preserved marine mollusks (Powers, 1968). The rocks comprise marly sandstone, sand, marl, clay, and sandy limestone with some strata rich in chert and minor gypsum. The colors are dominantly green with some red, brown, white, and pink (Al-Sayari and Zötl, 1978).

Two samples were picked from Hadrukh Formation outcrop in the study area at locations sample-2 and 3 shown in Figure 3.1. Accordingly two thin sections were made from these samples as shown in Figures 3.7a and 3.7b. The thin section of Figure3.7a shows fine to medium quartz grains with calcite cement. These grains are poorly sorted and show sub-rounded to rounded shapes. Another lithology is exhibited by this section that contains carbonate clasts with few scattered quartz grains floating in carbonate matrix and silica cement filling existing fractures. Figure 3.7b shows limestone as the main lithology with existing fine to medium quartz grains.

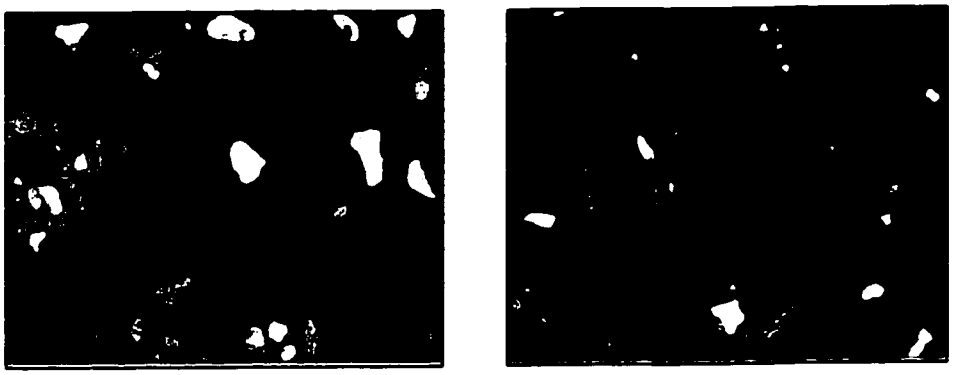

Figure 3.7: a- (left) Fine to medium sandstone grains with carbonate clasts b- fine grained silty sandy carbonate.

Dam Formation

The Dam Formation takes its name from the type locality at Jabal al Lidam (lat. 26°21′42″ N, long. 49°27′42″ E) where the lower part is exposed. The upper part is exposed at Al Umayghir, which is very close to the type locality making up a full section of about 90 meters (Powers, 1968). Unlike the Hadrukh Formation, Dam Formation is exposed in scattered patches from lat. 27°30′N trending southeast to south of Qatar (Al-Sayari and Zötl, 1978).

The thickness of the Dam Formation ranges from 30 meters to about 90 meters at the type locality to as thick as 100 meters found in other areas (Powers, 1968). The Dam Formation was deposited through a major Neogene transgression and it contains shallow marine and warm water fossils (Weijermars, 1999). The marine transgression extends about 120 kilometers inland from the modern coastline. It covers areas from south of Qatar to Jibal an Nu'ayriah that comprises a distance of about 450 kilometers parallel to the coast. At the margins, around the eastern part of the study area, the Dam Formation rapidly gives way to continental deposits (Powers, 1968).

The Dam Formation biostratigraphically correlates with the Lower Fars Formation of Iraq (Powers, 1968). The Indo-West Pacific origin of the Dam Formation marine biota is dated as Burdigalian (16-19 Ma) (Whybrow et al., 1987). Pink, white, and gray marl, and red and green clay with interbedded limestone, sandstone and coquina comprise the Dam Formation (Al-Sayari and Zötl, 1978).

Figure 3.8 shows a thin section cut from a sample collected from the Dam Formation outcrop in the study area (sample-4 location, Figure 3.1). This section shows a mudstone with few forams and some shell parts with their spaces filled with carbonate.

Also quartz grains are present from silt to medium size moderately sorted and sub-rounded.

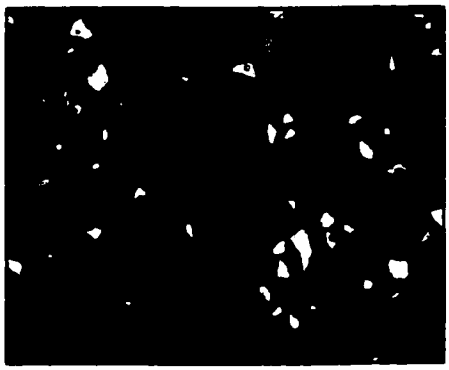

Figure 3.8: Dam Formation thin section.

Hofuf Formation

The type locality is about 15 kilometers northwest of the town of AL Hufuf (lat. 25°22′ N, long. 49°35′ E) from which the Hofuf Formation takes its name (Powers, 1968). It is lenticular and heterogeneous with variable thickness from a place to another. It unconformably overlies the Dam Formation with thickness varying from 30 to 100 meters (Whybrow et al, 1987).

The Hofuf Formation is well exposed on the anticline of the giant Ghawar field where it almost mirrors the field's outline. The upper part of this formation is capped with hard sandy limestone not only in the coastal region but also in the western interior, part of which is the eastern part of the study area. It is generally covered with gravel deposits which were supplied by the erosion of the interior Arabian foreland. This occurred because of the tilting of the Arabia foreland after the time of the Dam Formation. The gravel deposits include quartz, limestone pebbles and boulders, igneous rocks, and metamorphic rocks (Powers, 1968).

The Hofuf Formation is considered to be the closing unit of the Arabian Tertiary deposits and thus it could be of late Miocene to Pliocene (Powers, 1968). The vertebrate-bearing zone that stratigraphically lies about 30 meters above the Dam Formation at Al Jadidah is dated about 14 Ma (Whybrow et al., 1987). At the type locality, it consists of red and white conglomerate, greenish-gray to red sandy marl, red and light gray argillaceous sandstone and gray marly conglomerate with limestone boulders in a quartz sand matrix (Al-Sayari and Zötl, 1978).

Thin sections were made for two samples acquired from Hofuf Formation outcrops in the study area. The two samples shown in Figures 3.9a and 3.9b were collected respectively at locations sample-1 and 5 in Figure 3.1. Figure 3.9a shows fine grain chert with some fine to medium quartz grains. There are few pores in this section and they are circulated by chalcedony nodules. Figure 3.9b is a typical sample from a continental formation such as the Hofuf Formation. The sample includes mainly quartz that is poorly to moderately sorted with sub-rounded to rounded grains. The cement is mainly carbonate. Few heavy minerals such as zircon are also present.

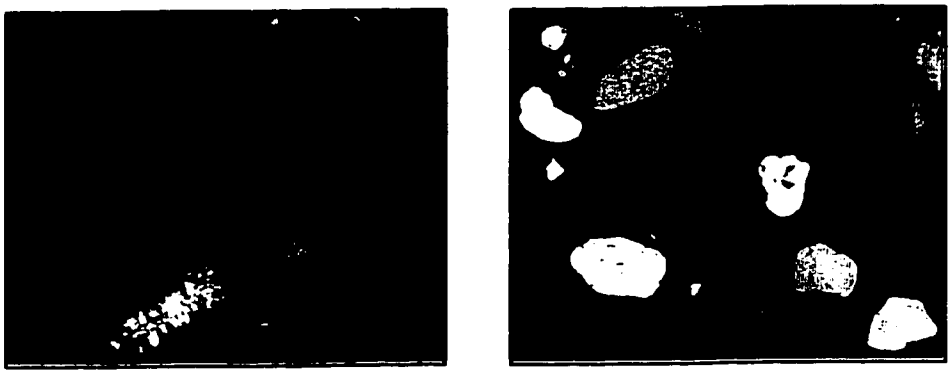

Figure 3.9 a- (left) chert with chalcedony nodules b- (right) fine to coarse grained sandstone.

3.2 Data Preparation and Quality Assessment

3.2.1 Introduction

Prior to commencing any data analysis in practice, the data samples must be checked for outliers. In most cases, unless the cause of the outlying values can be understood, they should be removed. However, outliers may represent a second population, or legitimate extreme values in the data, in which case they should be retained.

3.2.2 Vibrator Performance Control Data

Vibrator performance control data are obtained from seismic surveys that use vibrator as a source. The spatial distribution of such data will be the same as the distribution of vibration points (VP's) in the survey design.

The vibrator performance control data that will be used in this study come from a recently acquired 3D seismic survey in the study area. Refer to Al-Ali et al, (2001) for detailed description of the survey design. The VP's in this survey are acquired 720 meters apart along east-west lines and 480 meters apart along north-south lines (Figure 3.10). The VP's along each line are spaced at 60 meter intervals. Five vibrators are used at each VP spaced by a 12 meter interval following an east-west pattern.

Pursuant to vibration completion at every VP, vibrator performance data are sent from each vibrator via radio transmission to the recording truck where they are analyzed for quality control purposes and stored for further uses. Besides the vibrator performance control data, other useful information such as position of each vibrator, vibration time, and vibrator number are also transmitted.

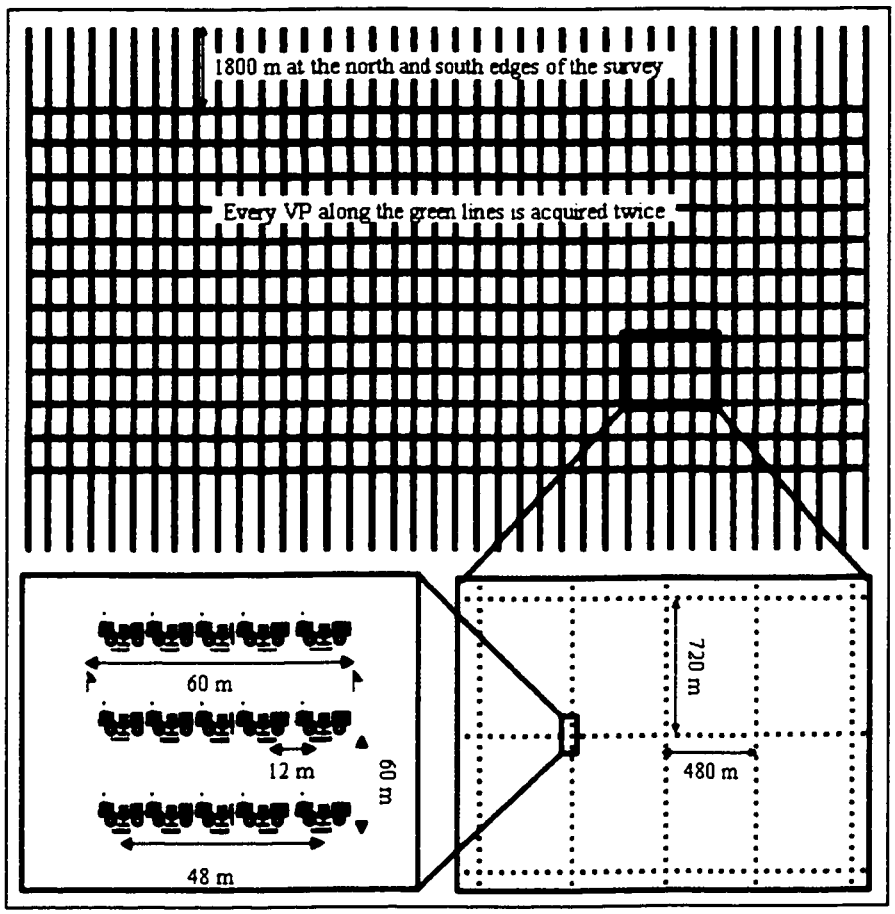

Figure 3.10: Vibrator performance control data geometry.

Positioning

The current practice in seismic acquisition is to survey source and receiver positions using Real Time Kinematics (RTK), and then the Real Time Source Positioning (RTSP) is used for source positions quality control (QC) while recording. Today, each vibrator is equipped with a Differential Global Positioning System (DGPS) receiver for location determination that is sent to the recording truck via radio from all involved vibrators at a pre-surveyed (flagged) center location for these vibrators. The real-time center of gravity (COG) is calculated in the recording truck using RTSP from all vibrators. COG is

defined as the geometrical center of all vibrator pads making up a source array at ground level. It is checked against the surveyed RTK position for QC.

Whereas the importance of COG for QC is well recognized, much less attention seems to be paid for using it as a final source position. That is because of the relatively big uncertainty in real time measurement of elevation (Z-coordinate). However, for this study, the spatial coordinates X and Y are of more importance for vibrator performance control data analyses so that each vibrator information is placed at its spatial position. Because of the fact that RTK data provide only a single position for the COG of the five contributing vibrators, the RTSP data will be checked if they are within acceptable tolerances.

COG's were calculated from RTSP data and compared to those obtained from RTK. obtained from the two systems. Figure 3.12 shows a histogram of the absolute positioning variations. Real measurements showed that RTK provides positions within few centimeters accuracy for X, Y, and for the Z coordinate ±2 cm while RTSP provides positions within ±30-50 cm accuracy for X and Y, and about ±1 m accuracy for the Z coordinate. The majority of the obtained differences follow these accuracy limits. Differences falling outside these limits can be attributed to the limitations of the process of positioning the vibrators in practice with an acceptable tolerance of ±10 m knowing the fact that only the center of the array is flagged. Therefore, the RTSP X and Y coordinates will be used to represent the spatial locations of the vibrator performance data.

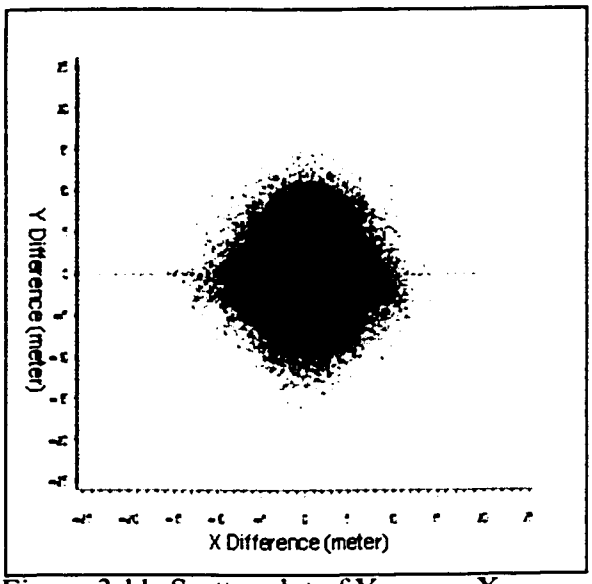

Figure 3.11: Scatter plot of Y versus X positioning differences.

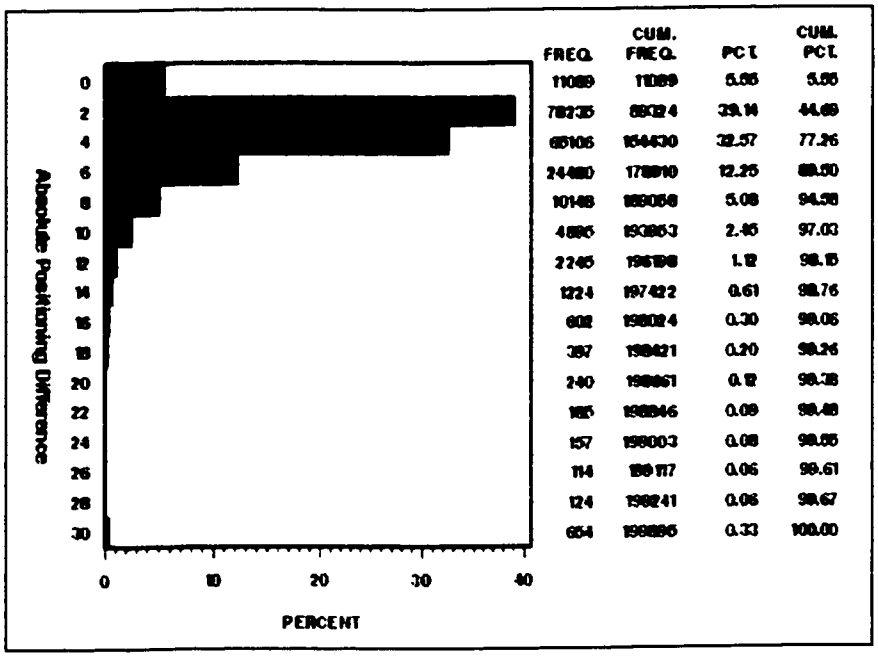

Figure 3.12: Absolute positioning differences statistical distribution.

Visual Quality Assessment

Vibrator performance control data are gathered in time-order, therefore, a time series presentation may give some indication about the behavior of these data. If the

common cause of variations of vibrator measurements is due to the reaction to surface conditions, then the majority of the vibrators operating at the same time would provide approximately similar measurements.

On the other hand, any specific variation in this process is assumed to be mainly due to problems associated with particular vibrators. Problems occuring with vibrators could be mechanical related to the vibrator itself, and instrumental related to the control system. Performance control data obtained from a vibrator that has a problem will deviate from the majority.

Figure 3.13 shows a time series for one day acquisition of the five involved vibrators at each VP, where each vibrator is represented by a different color. It is clear from this data presentation that vibrator number 4 provided measurements that show obvious deviation from the majority. It was noted that deviations are more apparent in some measurements than in others. In this case the ground viscosity exhibits more deviation than the ground stiffness. This task was performed on a daily basis for all vibrator performance control data. Data belonging to any vibrator that shows obvious deviation from the majority were removed from the analyzed data set.

Three-sigma Limits

As discussed in Section 2.3.2, world measured data occur within three standard deviations from both sides of the mean. Therefore, pursuant to the visual quality assessment step, data samples that fall outside the three-sigma limits were removed from the data set. This operation was performed also on a daily basis as shown in Figure 3.14.

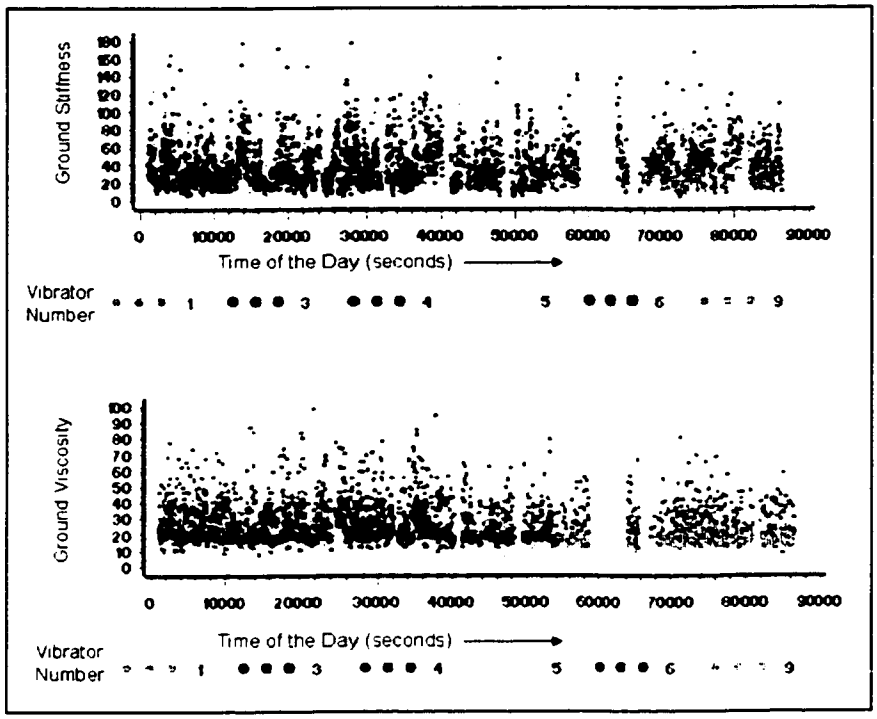

Figure 3.13: Time series plots of stiffness (top) and viscosity (bottom).

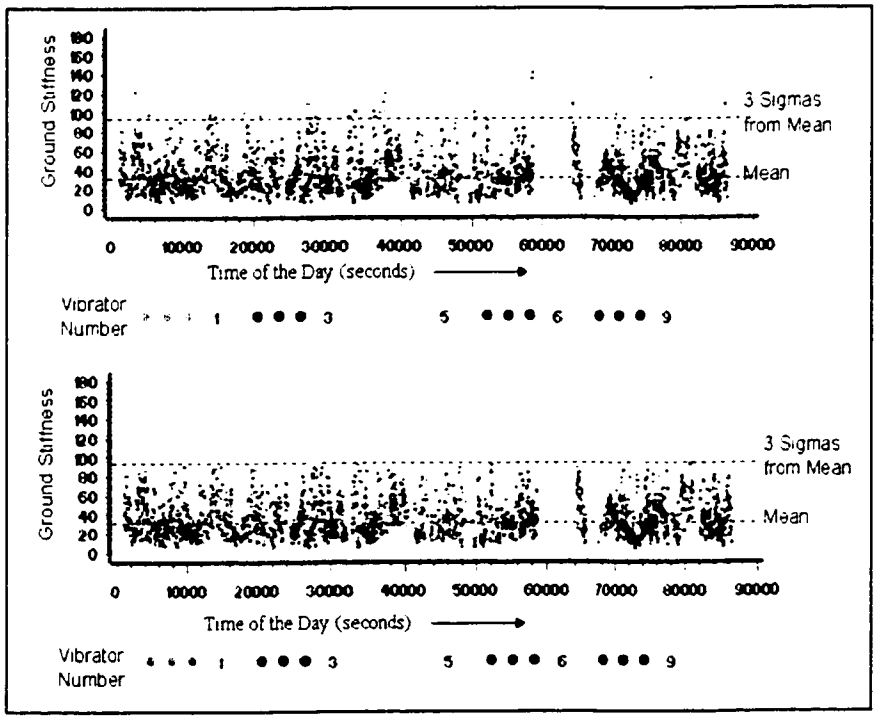

Figure 3.14: Three sigma limits approach, before application (top) after application (bottom).

Spatial Smoother

A spatial smoother was finally applied to the vibrator performance data. This is obtained by applying a rectangular smoother whose length in the X direction and in the Y direction, which is given by:

$$U(x,y)=\frac{1}{n}\sum_{x'}\sum_{y'}U'(x',y') \tag{3.1}$$

where:

$U(x,y)$ estimated point

$U'(x',y')$ sampled data point

$$\frac{x-X_{sm}}{2}<x'<\frac{x+X_{sm}}{2}$$

$$\frac{y-Y_{sm}}{2}<y'<\frac{y+Y_{sm}}{2}$$

Different smoother lengths were experimented with on the data, and finally a smoother with a 960 meter X_{sm} and a 1440 meter Y_{sm} seemed to be best. Figures 3.15 to 3.23 show the final vibrator performance control data maps.

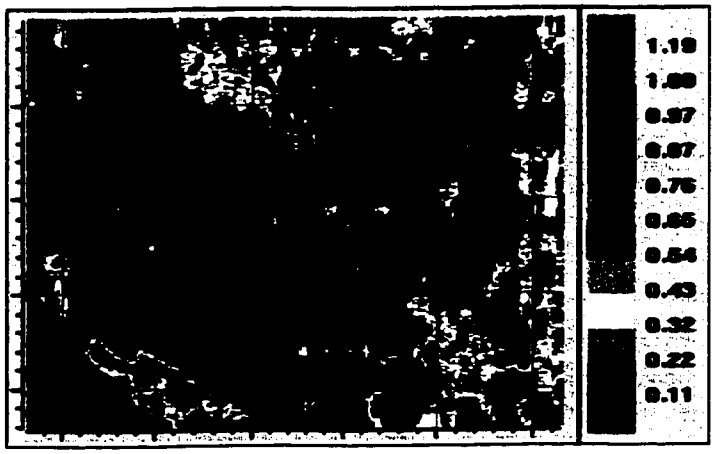

Figure 3.15 Average phase (degree) map.

Figure 3.16: Maximum phase (degree) map.

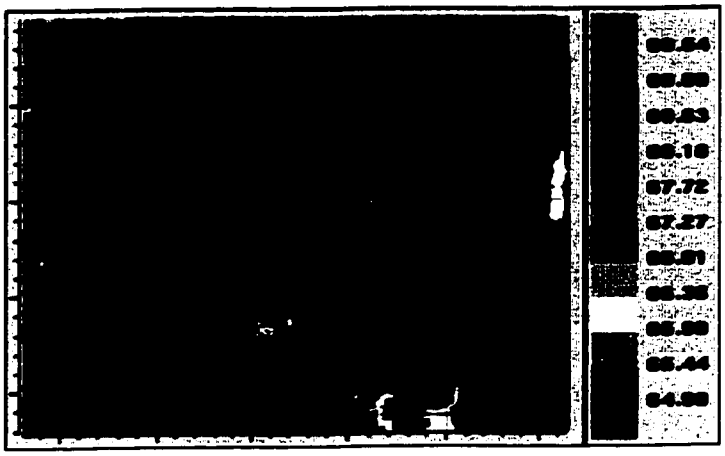

Figure 3.17: Average force (%) map.

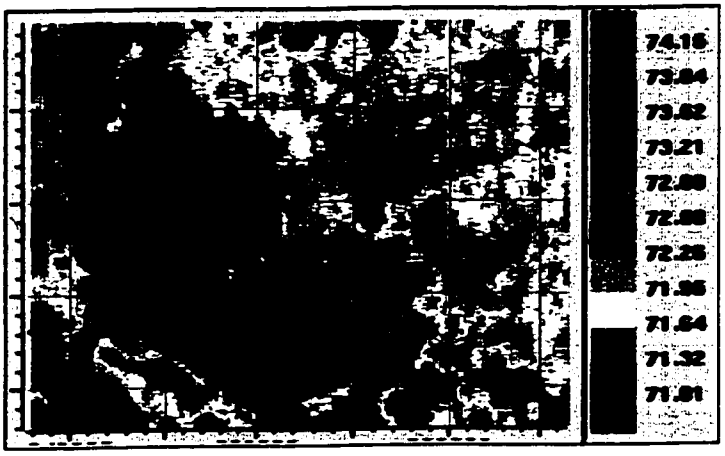

Figure 3.18: Maximum force (%) map.

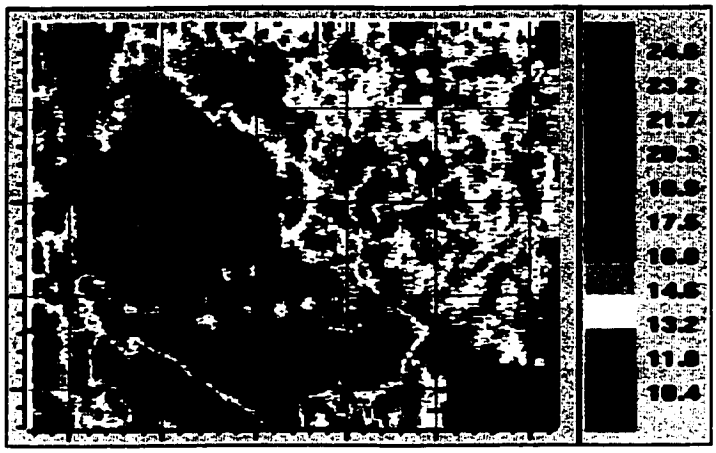

Figure 3.19: Average distortion (%) map.

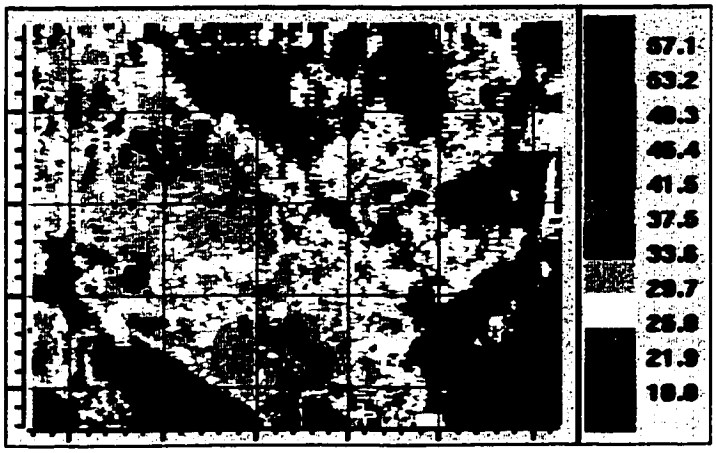

Figure 3.20: Maximum distortion (%) map.

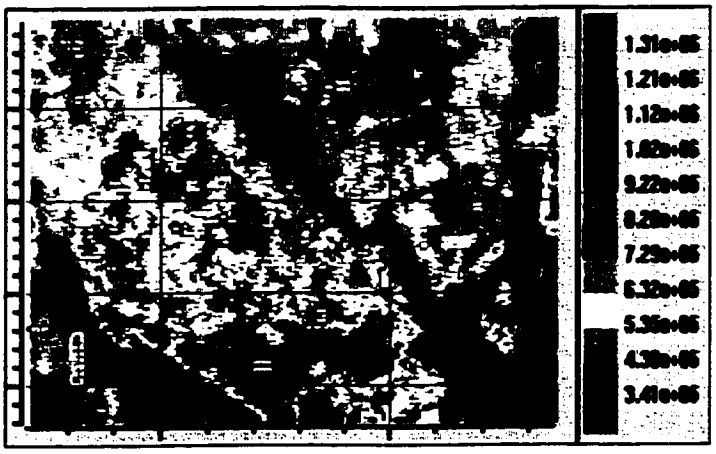

Figure 3.21: Ground viscosity (N.s/m) map.

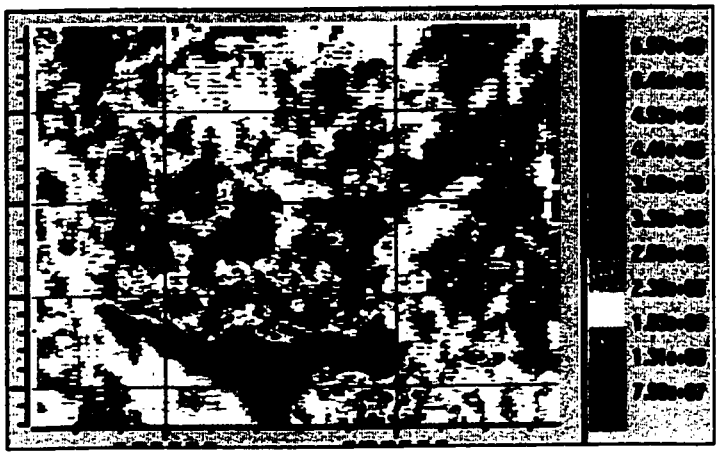

Figure 3.22: Ground stiffness (N/m) map.

Figure 3.23: Calculated V_s (m/s) map.

Repeatability

Vibrator performance control data provide indications about the interaction between vibrator and ground. Therefore, it is prudent to investigate their repeatability over time.

Figure 3.10 shows that VP's along the north-south lines are acquired twice at different times. Therefore, this data set can be used to make a repeatability experiment. Figure 3.24 shows cross-plots of all vibrator performance attributes measured independently two times. The horizontal axes of these plots represent measurements made at time 1 and the vertical axes represent measurements at time 2. The ground parameters:

stiffness and viscosity exhibit the best repeatability among the other attributes with very high correlation coefficients. Distortion attributes also show reasonably good repeatability. The least repeatability is obtained for phase and force attributes.

The weak repeatability exhibited by phase and force was theoretically predicted, as explained in Section 2.1.6. The elimination of certain attributes from the modeling step will be discussed and justified in the next chapter.

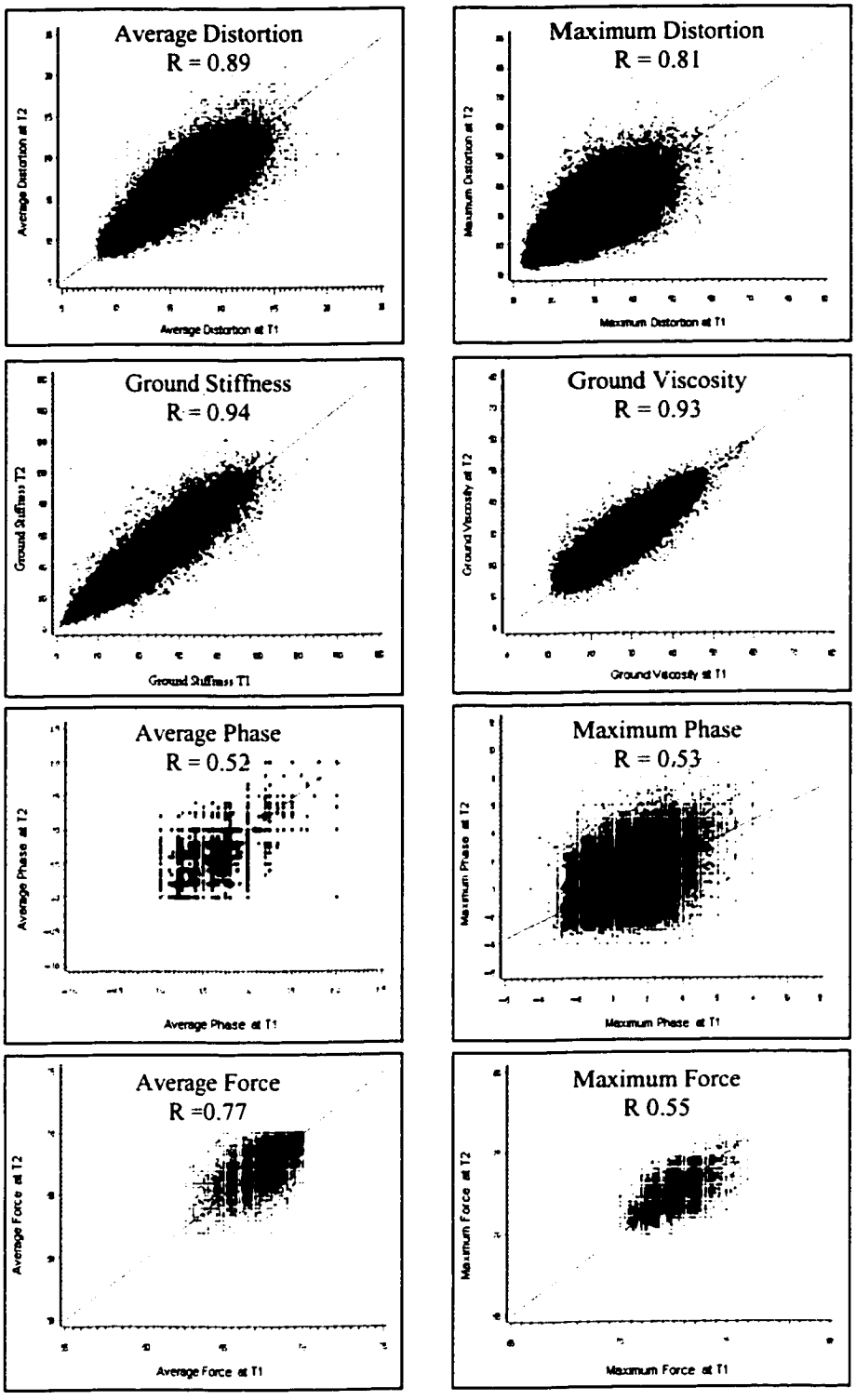

Figure 3.24: Repeatability of vibrator performance data a- average distortion, b- maximum distortion, c- ground stiffness, d- ground viscosity, e- average phase, f- maximum phase, g- average force, h- maximum force. Horizontal axis: first measurement (T1), vertical axis: second measurement (T2).

3.2.3 Uphole Data

Upholes represent the source of primary V_p data in this study. 463 upholes are available in the study area spatially distributed as depicted in Figure 3.25. Twenty wells marked in black in this figure will be excluded from all subsequent analyses, and used later as control points for method validation.

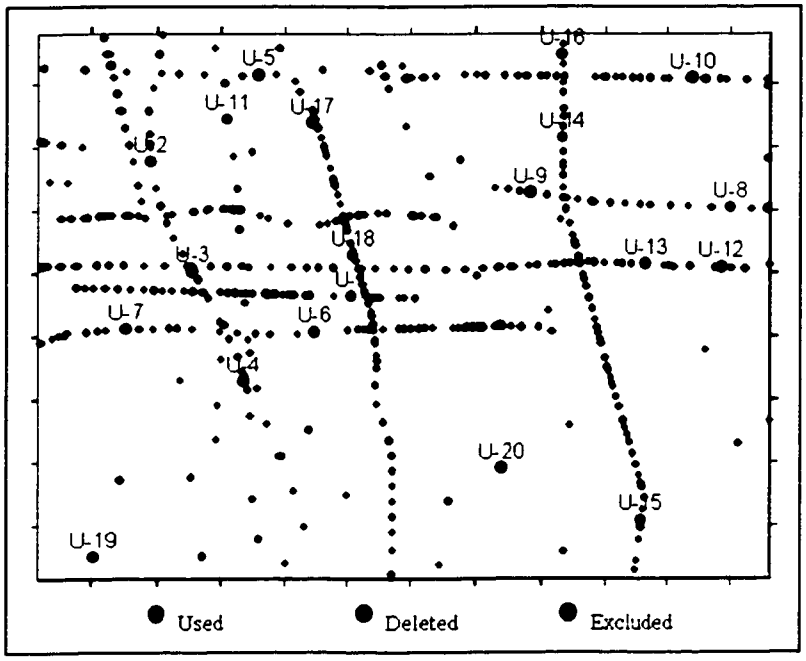

Figure 3.25: Spatial distribution of upholes in the study area.

The depths of penetration of these upholes are variables as summarized in Figure 3.26. The data pertaining to each uphole are available as depth-time pairs where each pair represent the depth and the time it takes the compression wave to reach this depth from the surface.

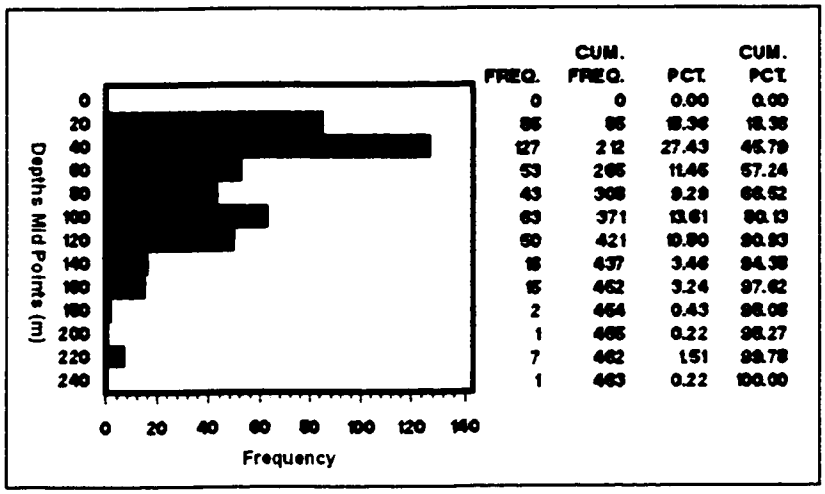

Figure 3.26: Upholes penetration depths statistics.

Depth-Time Plots

Depth versus time plot is constructed for each uphole as shown in Figures 3.27a and 3.27b. Such plot assists in detecting anomalous samples. Theoretically travel time should increase with depth. However, this criterion is sometimes not satisfied due to various reasons. For example, cavities or fractures introduced by the drilling process can result in anomalous travel times. Another source of error could be experimental such as a wrongly picked arrival time or an incorrect depth. Errors caused by these factors normally manifest themselves on the depth-time plots, and thus can be corrected provided that enough control points are available. The time of 31 ms at depth of 48 m shown in Figure 3.27a is a clear outlier. However, we could face some more complicated erratic values, like that shown in Figure-27b where the whole data set will be discarded from analysis. 11 upholes of the analyzed data exhibited this behavior and were discarded from the analysis (Figure 3.25).

In general, uphole survey cannot provide perfect results. For instance, lateral changes in near-surface geology can cause wrong measurements depending on the

magnitude of the source,or the receiver offset from the well. The assumption of straight raypath from source to receiver can be another source of bad measurements, especially with heterogeneous near-surface layers (Cox, 1999). Nevertheless, as in our case source offset from the borehole is relatively small, the magnitudes of these errors is minimal.

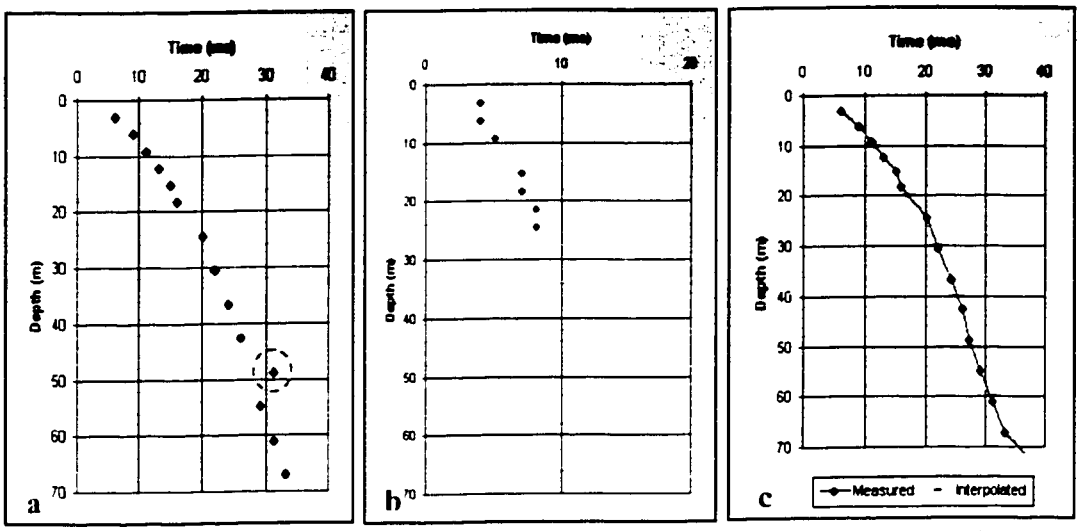

Figure 3.27: a) and b depth-time plots for uphole data c) travel time to certain depth calculation.

Iso-depth Velocity Layers

Average Vp velocity in iso-depth layers from the surface is calculated from the uphole data. The velocity layers shall be used for subsequent integration with secondary data set as discussed in the previous chapter.

Depth-time pairs exist in variable depth intervals for each uphole measurement. Hence, a depth-time curve can be constructed by a succession of linear segments between sampled data points. Six iso-depth average velocity layers for depths of 10 to 60 meters with an increment of 10 meters will be determined for this study. Travel time to a certain depth is determined using linear interpolation in the respective linear segment as shown in

Figure 3.27c. The average velocity is then calculated by dividing the depth by the travel time.

Spatial Consistency

Upholes were analyzed individually in the previous two steps. Next the spatial consistency of the calculated iso-depth average velocity layers must be considered for all upholes in the study area. For this reason, an average velocity map was generated for each iso-depth using least square interpolation as shown in Figure 3.28. This step is performed in order to detect if any adjustment is required to the calculated average velocities when significant velocity change occurs. Surface elevation and geology must be taken into account prior to any modifications.

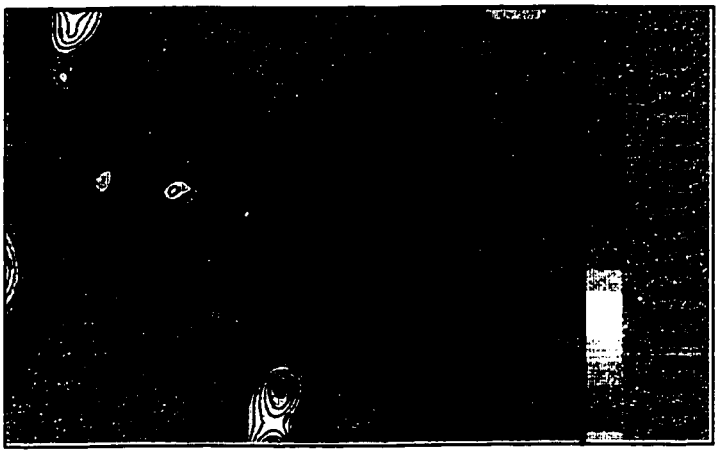

Figure 3.28: 20 meter average velocity map. (contour interval 200 m/s)

3.3 Univariate Statistics

Univariate statistics can reveal if there exist erratic values within a particular data set. In the previous section, data quality assessment was carried out following certain

approaches for both primary and secondary variables. In this section, univariate statistics will be calculated in order to detect if any residual erratic values have remained and also to determine the data set ranges.

3.3.1 Vibrator Performance Control Data

Univariate statistics were generatd for vibrator performance data at different phases. These phases are: raw data, visually edited data, three-sigma application, and spatial smoother. Univariate statistics for each of these stages are presented in Appendix II.

	No. Samples	Mean	Median	Standard Deviation	Skewness	CV
Average Phase	175747	0.71	0.75	0.2	-0.94	0.2834
Maximum Phase	175747	0.63	0.62	0.76	0.22	1.2022
Average Distortion	175747	14.86	14.9	2.61	-0.09	0.1757
Maximum Distortion	175747	26.27	26.64	5.51	-0.06	0.2097
Average Force	175747	68.69	68.79	0.45	-1.42	0.0065
Maximum Force	175747	72.31	72.35	0.5	-0.19	0.0069
Ground Viscosity	175747	6.78E+05	6.59E+05	1.56E+05	0.59	0.2304
Ground Stiffness	175747	2.13E+08	1.91E+08	75244594	1.56	0.3532
Shear Velocity	175747	606.7	475.67	324.97	1.25	0.5356

Table 3.1: Vibrator performance control data univariate statistics.

Table 3.1 shows a summary of the univariate statistics for the final vibrator performance control data. No obvious erratic values could be inferred from these

statistics. This is attributed to the preceding operations when preparing this data set. Phase and force attributes vary in narrow ranges as depicted by the standard deviation. The maximum phase coefficient of variation with a value greater than one resulted because this variable involves positive as well as negative values.

3.3.2 Upholes **Iso-Depth Average Velocity**

Table 3.2 presents univariate statistics calculated for each siso-depth average velocity layer. The number of contributing samples decreases as the depth increases due variable depth penetrations. All distributions have positive skewness indicating that the mean is greater than the median. These univariate statistics do not show any alarming extreme values.

Depth	No. Wells	Mean	Median	Standard Deviation	Skewness	CV
10	432	1120.58	1045.80	382.66	1.09	0.34
20	429	1410.68	1322.64	453.48	1.09	0.32
30	353	1559.12	1442.29	539.90	1.49	0.35
40	322	1679.02	1557.35	547.73	1.44	0.33
50	227	1708.73	1592.19	497.21	1.09	0.29
60	217	1776.66	1678.94	488.94	0.96	0.28

Table 3.2: Iso-depth average velocity layers univariate statistics.

CHAPTER 4

DATA RELATIONSHIPS AND INTEGRATION

4.1 Relationships

Integration of V_p obtained from upholes (primary data) and vibrator performance (secondary data) is an essential task in this study. However, before pursuing this step, the relationships between primary and secondary data components must be first established. Analytical and hypothetical relationships were advanced in Chapter 2. In this section relationships will be investigated using study area data as an attempt to validate the previously developed relationships and then perform their integration.

The relationships will be evaluated based on the correlation coefficient that measures the linear relationship between two variables. The correlation coefficient ranges from -1 to 1. Two variables that have a correlation coefficient of either -1 or $+1$ follow an exact linear relationship. A zero correlation coefficient indicates absence of correlation between two variables. Accordingly, correlation coefficients for collocated measurements

of primary and secondary were calculated. Table 4.1 and Figure 4.1 show correlation coefficients between the six iso-depth velocity values obtained from the upholes and the vibrator performance control data.

Depth (m)	10	20	30	40	50	60
Average Phase	0.19	0.24	0.26	0.23	0.26	0.25
Maximum Phase	-0.20	0.03	0.02	0.03	0.13	0.15
Average Force	0.09	0.04	0.05	0.04	-0.01	-0.05
Maximum Force	0.51	0.57	0.54	0.54	0.53	0.49
Average Distortion	0.62	0.64	0.58	0.56	0.49	0.47
Maximum Distortion	0.53	0.56	0.50	0.49	0.44	0.43
Ground Viscosity	-0.56	-0.57	-0.53	-0.49	-0.44	-0.42
Ground Stiffness	0.66	0.64	0.62	0.60	0.51	0.46
V_s and V_p	0.71	0.71	0.69	0.66	0.56	0.52

Table 4.1: Correlation coefficients of iso-depth uphole velocities and vibrator performance control data.

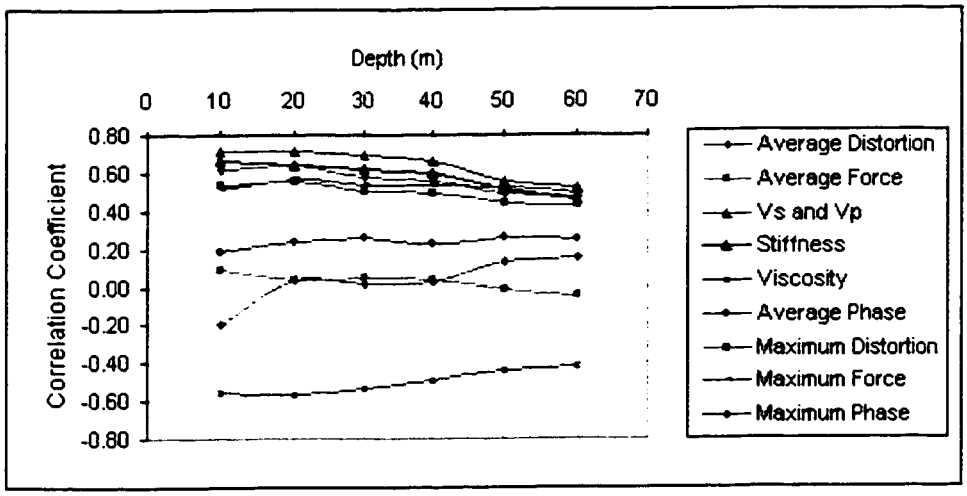

Figure 4.1: Depth versus correlation coefficients plot.

4.1.1 Phase Attributes

It is clear from Table 4.1 that both average and maximum phase attributes have poor correlation coefficients. Figures 4.2 and 4.3 show scatter plots of respectively the average and maximum phase attributes and the 20 meter iso-depth uphole velocities. These scatter plots do not indicate any coherent relationship as also predicted by the correlation coefficients.

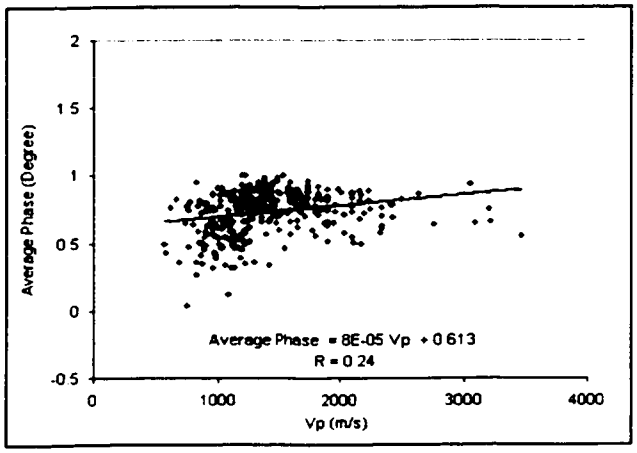

Figure 4.2: Cross-plot of average phase versus 20 meters iso-depth uphole velocities.

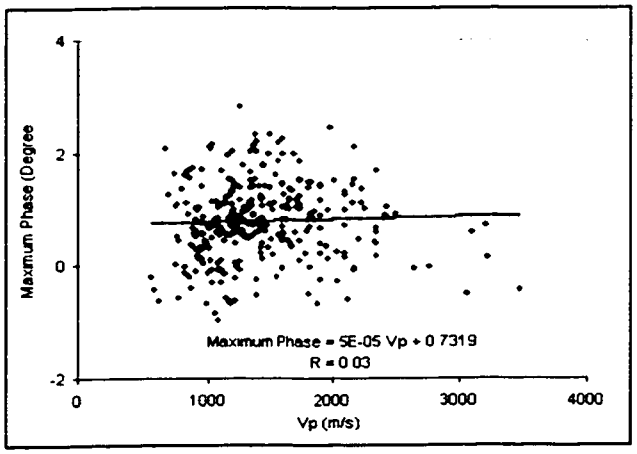

Figure 4.3: Cross-plot of maximum phase versus 20 meters iso-depth uphole velocities.

It was noted in Section 2.1.3 that one of the vibrator control system functions is to minimize the discrepancies between the phase of the pilot signal and the feedback signal. This is done by continuously adjusting the drive system throughout the vibration duration by applying negative or positive phase shifts. The final average phase value results from averaging of all phase shifts, negative and positive, applied during the sweep and thus resulting in a value that varies in a narrow range from one location to another. The maximum phase represents a single value of maximum applied phase shift that can occur at any time through the vibration for various reasons including mechanical or interaction with the ground. However, it is not possible to separate between the two causes of variations.

The repeatability study performed in Section 3.2.2 showed that measurements of phase attributes at the same location in different times had poor repeatability. Therefore, it can be concluded that phase attributes are not suitable for velocity estimation by means of integrating them with uphole velocities.

4.1.2 Force Attributes

The average force has poor correlation with vibrator performance control data while maximum force shows some correlation (Table 4.1). The average and maximum force attributes were crossploted with 20 meter iso-depth uphole velocities as respectively shown in Figures 4.4 and 4.5. The average force shows no clear correlation with uphole velocities, but maximum force shows an increasing relation as indicated by the positive correlation coefficient.

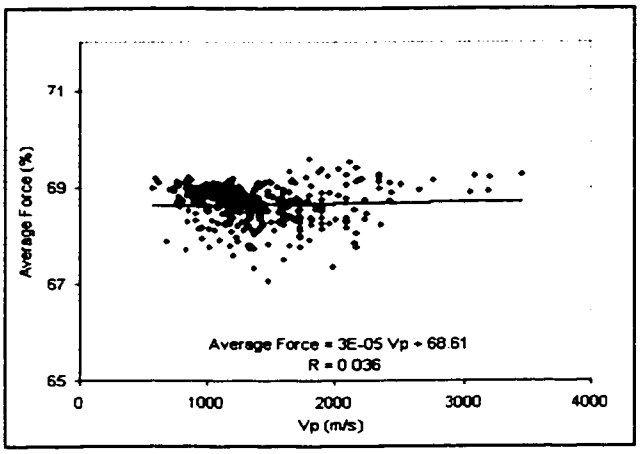

Figure 4.4: Cross-plot of average force versus 20 meters iso-depth uphole velocities.

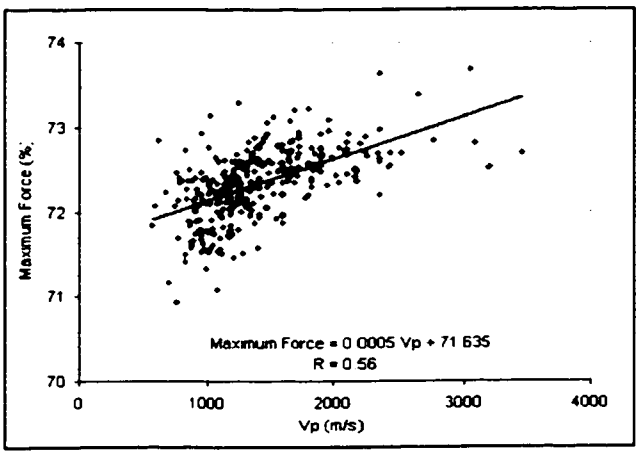

Figure 4.5: Cross-plot of maximum force versus 20 meters iso-depth uphole velocities.

The vibrator control system alters the exerted force in order to maintain similar amplitude between the pilot and the feedback signal as indicated in Section 2.1.3. This is performed by adjusting the vibrator drive level within preset thresholds in order to maintain consistent amplitudes from one location to another. Consequently, the average force does not show considerable spatial variations and thus can be excluded from the data integration part.

Maximum force, on the other hand, represents a single applied force value during the sweep. This occurs when the vibrator tries to overcome the ground's maximum reaction at its resonance frequency. The ground resonance frequency varies according to the surface material properties especially the ground stiffness. This justifies the increasing relation between the maximum force and the uphole velocities observed in Figure 4.4.

It should be pointed out that the repeatability study performed in Section 3.2.2 showed better repeatability of average force than the maximum force when both measured twice at the same location. Nevertheless, both force attributes vary in narrow ranges.

4.1.3 Distortion Attributes

Figures 4.5 and 4.6 show respectively crossplots of average and maximum distortion with 20 meter iso-depth uphole velocities. Both show increasing relationships, with a better correlation belonging to the average distortion.

The harmonic distortion is attributed to various reasons as discussed in Section 2.1.6. One of these is the non-linear interaction between vibrator and ground. In practice, it has been observed that distortion is larger when vibrating on stiff grounds. This justifies the obtained positive correlation between uphole velocities and distortion attributes.

Repeatability study of Section 3.2.2 showed better repeatability of the average distortion than maximum distortion. The greater correlation of average distortion with uphole velocities may be due to this reason.

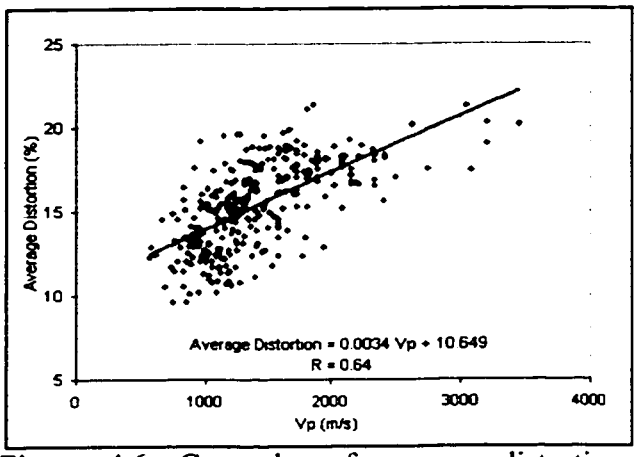

Figure 4.6: Cross-plot of average distortion versus 20 meters iso-depth uphole velocities.

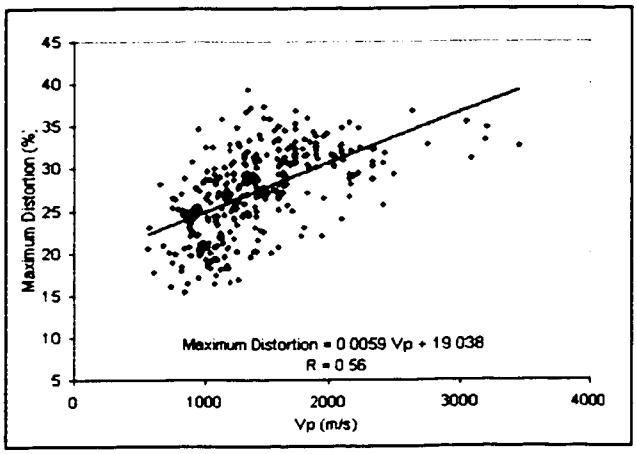

Figure 4.7: Cross-plot of maximum distortion versus 20 meters iso-depth uphole velocities.

4.1.4 Ground Parameters

Ground parameters: stiffness and viscosity exhibit relatively good correlation with uphole velocities (Table 4.1). Ground stiffness correlation coefficients are consistently higher than those of the ground viscosity.

Ground viscosity shows negative linear correlation with uphole velocities. Figure 4.8 shows a crossplot of ground viscosity and 20 meter iso-depth uphole velocities. Since viscosity represents the damping or energy dissipation, and loose materials dissipates

energy more than solid materials, therefore sandy areas have relatively higher viscosity and thus lower seismic wave velocity. This is attested by correlating surface materials present in the study area and the measured viscosity values.

Ground stiffness exhibits an increasing trend with uphole velocities (Figure 4.9), because stiffer materials have higher seismic wave velocities. This phenomenon is corroborated by the observations that when vibrating on surfaces covered with sand, lower stiffness values are obtained than when vibrating on gravel planes and hilly areas.

The repeatability study (Section 3.2.2) illustrated that ground parameters habe better repeatability than other vibrator control data attributes. This indicates that they are more strongly influenced by the medium properties than other factors, which in turn strengthens their significance for the presented study.

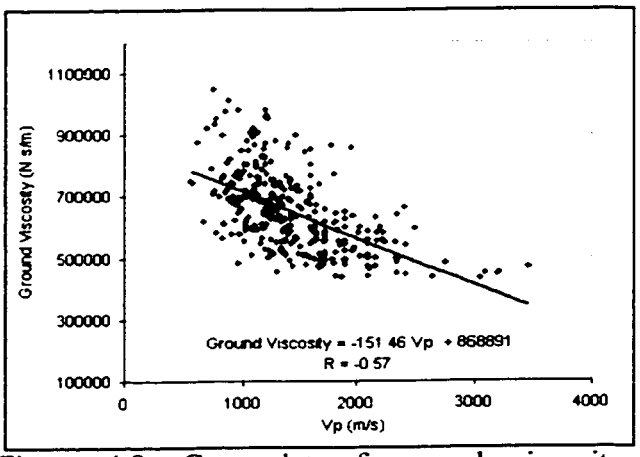

Figure 4.8: Cross-plot of ground viscosity versus 20 meters iso-depth uphole velocities.

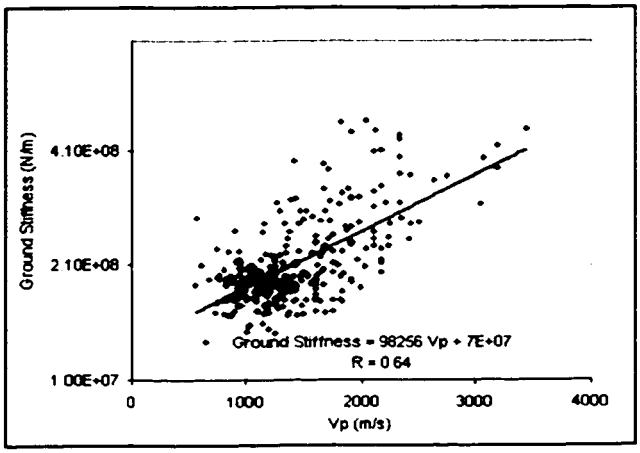

Figure 4.9: Cross-plot of ground stiffness versus 20 meters iso-depth uphole velocities.

4.1.5 Estimated Velocity

The analytical relations derived in Section 2.1.5 were used to estimate V_s from both ground parameters: stiffness and viscosity. Table 4.1 shows that estimated V_s possesses consistently higher correlation with uphole velocities. Figure 4.10 shows a crossplot of estimated V_s and 20 meter iso-depth uphole velocities. The exhibited linear relation is confirming the predictions.

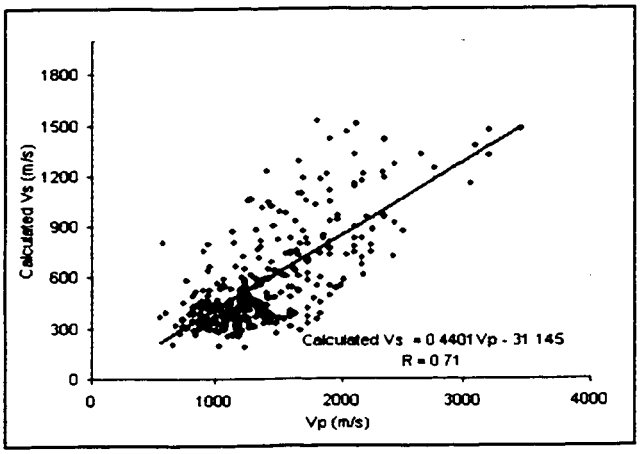

Figure 4.10: Cross-plot of calculated V_s versus 20 meters iso-depth uphole velocities.

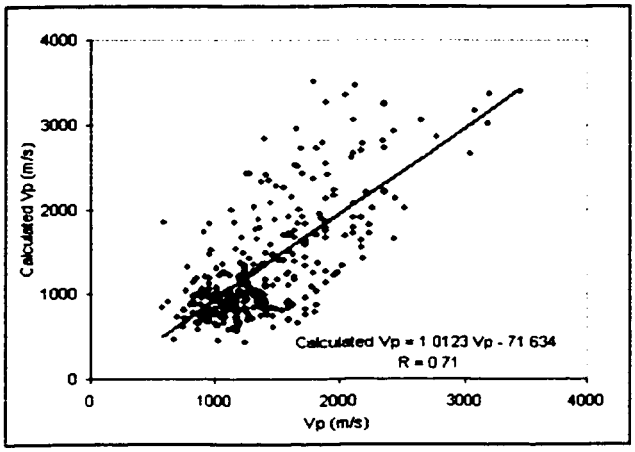

Figure 4.11: Cross-plot of calculated V_p versus 20 meters iso-depth uphole velocities.

The Vp is obtained by multiplying Vs by a constant of 2.3 as discussed in Section 2.1.5. This seems to fit the data well as shown in Figure 4.11 where the slope of the best fitted line is approximately 1.

4.1.6 Conclusions from the Observed Relationships

Previous relationship analyses revealed that estimated V_p has the best correlation with V_p obtained from upholes. The correlation coefficients pertaining to this attribute are greater than 0.65 to a depth of 40 meters. These correlation coefficients decrease with depth which confirms predictions. This is due to the fact that estimates derived from vibrator measurements are only influenced by a relatively thin section of the earth surface. There is an abrupt change in correlation coefficients occurring at 50 meter depth where they decrease from 0.66 to 0.56. This indicates that the depth of influence cutoff is lying between 40 and 50 meters depths.

Other attributes including ground stiffness, maximum distortion, and average distortion showed fair correlation with uphole data. Ground stiffness is the only attribute

among these that holds above 0.6 up to depth of 40 meters. However, ground stiffness is incorporated in the calculation of the estimated V_p. For theses reasons and its direct relation to V_p obtained from upholes, estimated V_p will be utilized in subsequent data integration up to a depth of 50 meters.

4.2 Data Spatial Analysis

In this section the spatial variability of the involved data including uphole and vibrator performance control data will by analyzed by means of semi-variogram analyses (Section 2.3.3).

4.2.1 Uphole Data

Semi-variograms (Section 2.3.3) were calculated for each set of the iso-depth velocities up to 50 meter depth. An omnidirectional semi-variogram was calculated using a lag distance of 1000 meters and 28 lags for each layer as a first step to determine if the data show an interpretable structure. This lag distance was found to give a good number of pairs in all directions. Next semi-variograms were calculated in six directions, with an angular tolerance of ±15°. All the semi-variograms revealed a northwesterly trending anisotropy in the data at about 145° from the north. The resulting semi-variograms were approximated by different models including multiply structured models, and for each model the kriging was performed. The parameters of those models that produced the least kriging errors are presented in Table 4.2.

Iso-Depth	Nugget	Range	Sill	Anisotropy Factor	Principal Direction	Model
10	18000	5200	1.2E5	0.85	145	Spherical
20	25000	5500	1.4E5	0.85	145	Spherical
30	20000	5500	1.8E5	0.85	145	Spherical
40	20000	5500	1.8E5	0.85	145	Spherical
50	20000	5500	1.5E5	0.85	145	Spherical

Table 4.2: Upholes iso-depths velocities semi-variogram models.

The equations of the spherical model are given by:

$$\left.\begin{aligned} V(h) &= C_0 + C_1\left[1.5\left(\frac{h}{a}\right) - 0.5\left(\frac{h}{a}\right)^3\right] && \text{if } h < a \\ V(h) &= C_0 + C_1 && \text{if } h \geq a \end{aligned}\right\} \qquad (4.1)$$

where C_0 is the nugget, C_1 is the sill, h is the lag, and a is the range.

4.2.2 Estimated V_p from Vibrator Performance Control Data

Semi-variograms for the estimated V_p were constructed in similar ways to those of the uphole data. A lag distance of 560 meters out to a maximum lag of 28,000 meters was used. A tolerance of ±15° was used for the directional semi-variograms.

The directional semi-variograms showed a pronounced anisotropy in the direction of 145° from the north. Figure 4.12a shows the covariance map of the measured variogram data of the estimated V_p. The variogram analyses used 50 offsets to the maximum offset, thus the covariance map axes range from -28,000 to 28,000 meters. Each cell in this map corresponds to certain lags in the X and Y directions. For instance,

the cell at X=5,000 and Y=-10,000 includes data for all pairs whose separation vector has an X value of 5,000 and a Y value of -10,000. This map assists in identifying the presence of anisotropy in the analyzed data as illustrated in this case along the 145° direction.

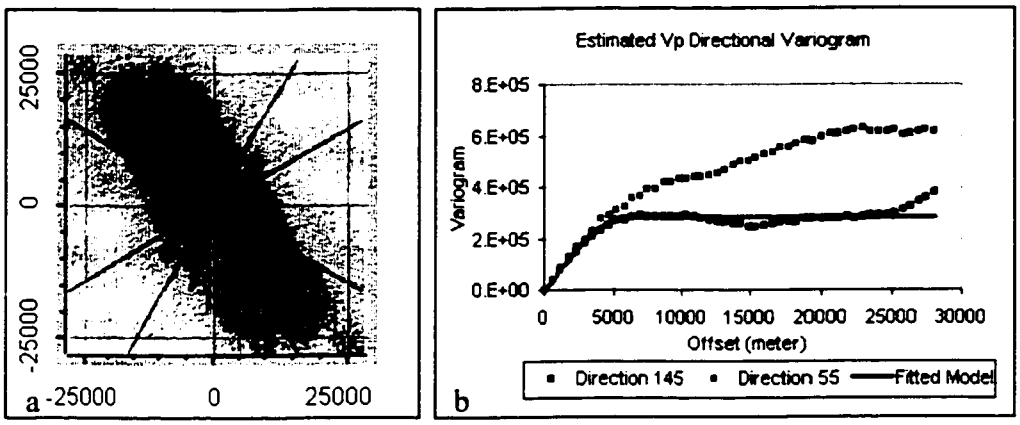

Figure 4.12: a) Covariance map b) Principal directions semi-variograms.

Two principal directions were identified from the six analyzed directions along which the semi-variograms were calculated. These two directions are the direction of the anisotropy and the one perpendicular to it at 55° from north. The semi-variograms along these two directions possessed different sill values as shown in Figure 4.12b. This feature was thoroughly analyzed and attempts were made to fit the obtained semi-variograms with different models. Finally a spherical model with C_0 = 0, C_1 = 2.85E5, a = 6000 meters was chosen. An anisotropy factor of 0.85 was selected with a principal direction of 145°. This semi-variogram model, Figure 4.12b, well fits the principal direction more and reasonably fits the other perpendicular direction within the given range.

4.3 Geostatistical Modeling and Validation

The geostatistical modeling was done by kriging and cokriging. First, the uphole data were kriged to estimate the excluded 20 upholes (Section 3.2.3). Next uphole velocities were integrated using cokriging with the estimated velocities from the vibrator performance control data

4.3.1 Kriging

Uphole data from each iso-depth was kriged to generate velocity maps. The cell size in each map was 60 by 60 meters giving a grid of 950 cells in the east-west direction and 720 cells in north-south direction. Figure 4.13 shows the iso-depth 20 meters kriged velocity map. Ordinary Kriging (OK) was used to generate this map (Section 2.3.3).

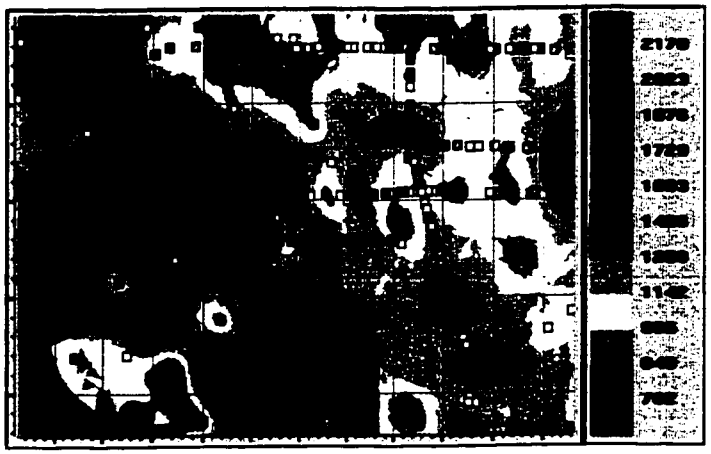

Figure 4.13: Iso-depth 20 meters uphole velocities kriged map.

4.3.2 Data Integration

Uphole data of each iso-depth were integrated with vibrator performance data using the relations established in Section 4.1. Before integration, estimated V_p values were kriged in order to form an exhaustive data set. Then, the integration was done using

cokriging (Section 2.3.4). Ordinary Cokriging (OCK) and Collocated Cokriging (CCK) were applied and results were assessed. CCK resulted in approximately similar results as the OCK, but in a faster time.

Figure 4.14 exhibits a iso-depth 20 meters cokriged velocity map. Besides honoring the uphole data, this maps also honors the features of the estimated Vp map. This gives this map a great deal of details compared to a smoother map obtained using kriging of uphole data.

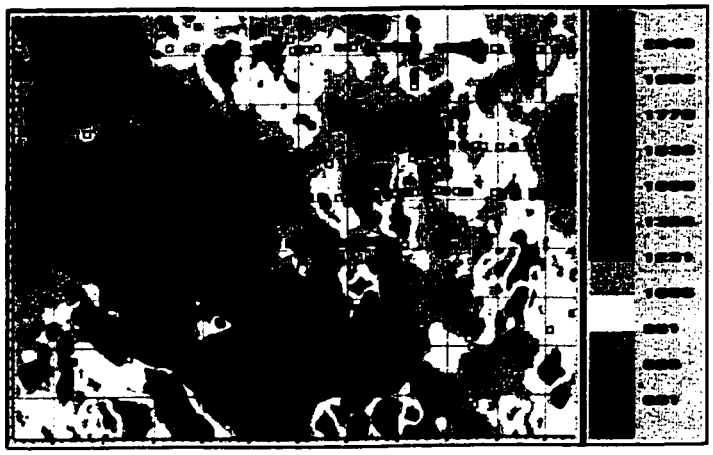

Figure 4.14: Iso-depth 20 meters uphole velocities cokriged map.

4.3.3 Validation

Validation of the results obtained from the previous geostatistical modeling was performed quantitatively using 20 excluded upholes (Section 3.2.3). Figures 4.15 to 4.19 show bar charts of the measured velocities from the 20 excluded upholes and the estimated velocities by kriging and cokriging.

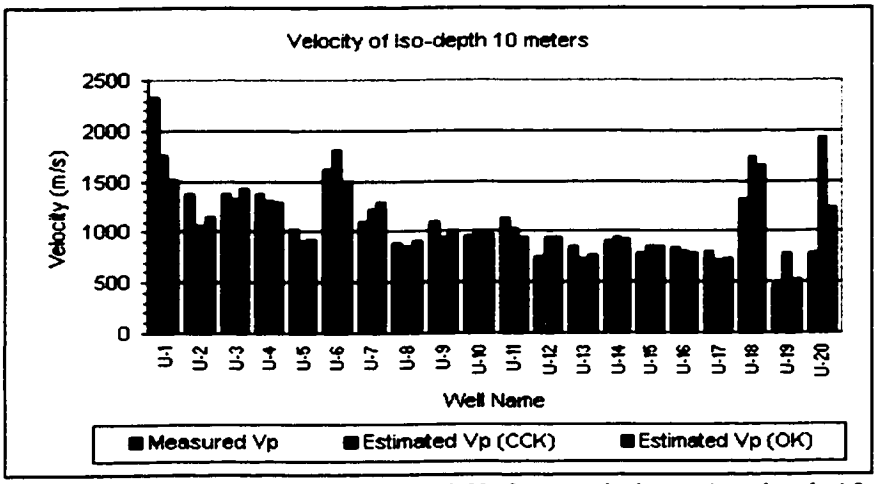

Figure 4.15: Bar chart of measured V_p from upholes at iso-depth 10 meters and estimated V_p from OK and CCK.

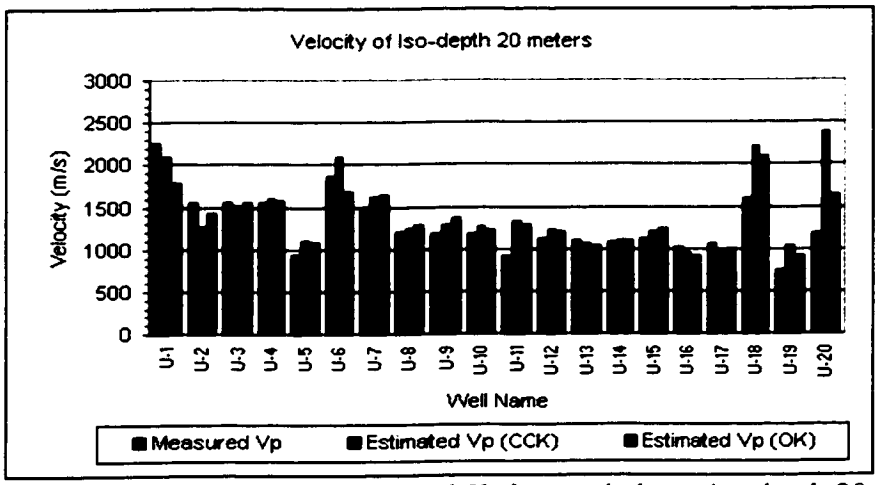

Figure 4.16: Bar chart of measured V_p from upholes at iso-depth 20 meters and estimated V_p from OK and CCK.

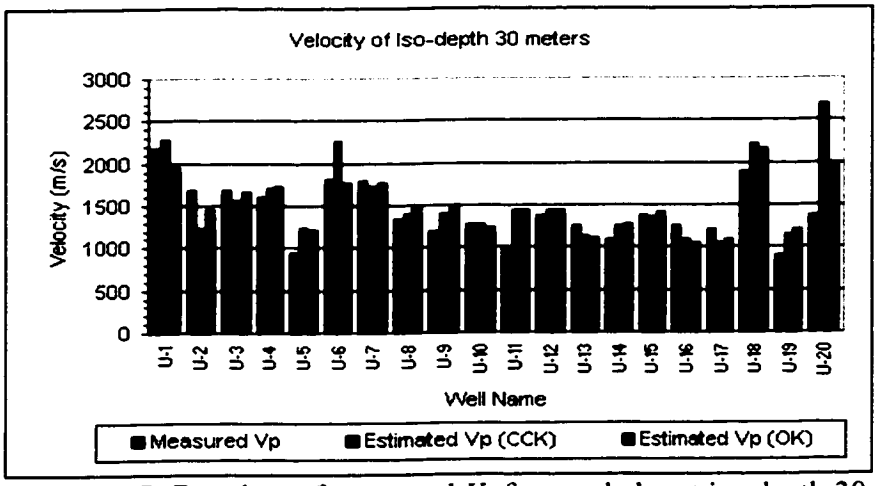

Figure 4.17: Bar chart of measured V_p from upholes at iso-depth 30 meters and estimated V_p from OK and CCK.

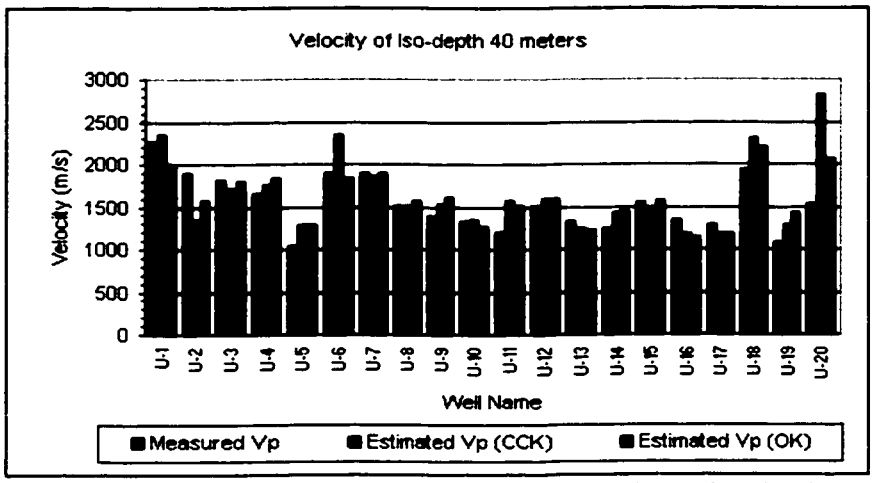

Figure 4.18: Bar chart of measured V_p from upholes at iso-depth 40 meters and estimated V_p from OK and CCK.

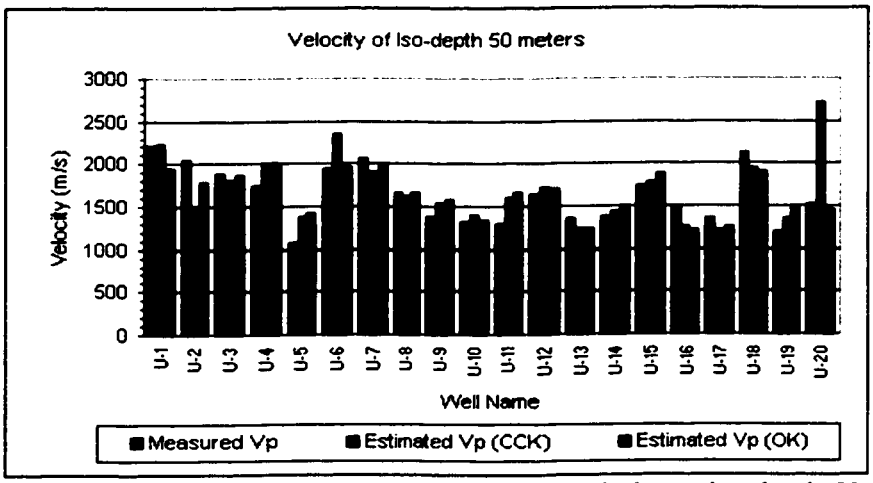

Figure 4.19: Bar chart of measured V_p from upholes at iso-depth 50 meters and estimated V_p from OK and CCK.

Table 4.3 presents the correlation coefficients between measured and estimated velocities at each iso-depth. Uphole U-20 showed a peculiar behavior as discussed below, and had to be excluded from the calculation of the correlation coefficients.

Iso-Depth	10	20	30	40	50
Uphole Data	0.78	0.79	0.76	0.76	0.79
Integrated Data	0.64	0.69	0.65	0.64	0.57
Uphole Data Excluding U-20	0.83	0.83	0.82	0.81	0.79
Integrated Data Excluding U-20	0.84	0.85	0.82	0.80	0.77

Table 4.3: Correlation coefficients between measured and estimated velocities from OK and CCK.

The anomalous uphole U-20 was thoroughly investigated. It is located in an area that was not sampled by the vibrator performance data, but within a vicinity of a contiguous high velocity area. The raw uphole data for no obvious reason for the uphole relatively low velocity measurements. The drilling report of this uphole indicates that hard limestone was encountered while drilling the first 30 meters, which somehow contradicts the low measured velocity values. Therefore, it was concluded that this uphole's measurements are questionable.

To further investigate the benefits of integrating uphole data with vibrator performance control data, the 19 of the 20 excluded upholes (U-20 was excluded) in iso-depth 30 meters were run through geostatistical modeling. This is done to mimic a case where we have only a limited number of sparsely located upholes. First, semi-variograms were calculated using these 19 upholes and then kriging was performed. Figure 4.20a shows a kriged map obtained using these upholes. Second, a relation between velocities from these upholes and the estimated V_p from vibrator performance control data was established. Then, integration was done using CCK. Figure 4.20b shows velocity map to depth of 30 meters resulting from this integration.

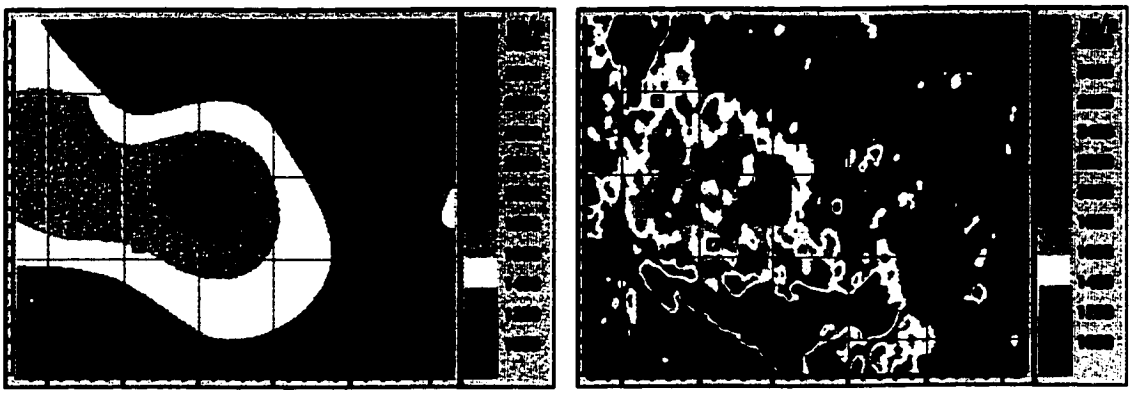

Figure 4.20: a) Kriged velocity map using 19 uphole samples b) Cokriged velocity map using 19 uphole samples and estimated V_p from vibrator performance control data.

The values of the uphole iso-depth 30 meters velocities were determined from the maps of Figures 4.20a and 4.20b. The correlation between the estimated values and the measured values are depicted in Figures 4.21a and 4.21b. It is clear from these figures that integration has reduced the uncertainty of velocity estimation as indicated by the correlation coefficient of 0.68 compared to a value of 0.34 obtained from estimations based on the uphole data only. Therefore, it can be concluded that integration of velocities measured from uphole and those estimated from vibrator performance control data is beneficial when estimating velocity distribution from sparsely located uphole data.

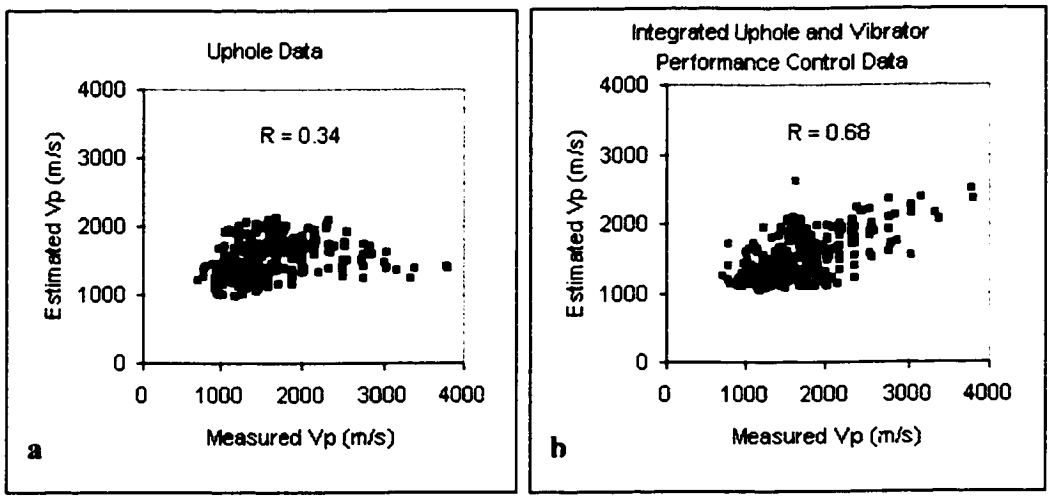

Figure 4.21: a) Crossplot of 353 measured uphole velocities and estimated velocities by OK b) Cross plot of the same uphole velocities and estimated velocities from integration using CCK.

CHAPTER 5

APPLICATION

An important application of near surface velocity is calculation of the static correction for seismic reflection and refraction measurements to remove topography and near surface variation effects. In this chapter the principle of static correction will be briefly described (refer to Cox, 1999 for detailed coverage). Then, two 3D velocity models for the near surface will be constructed for the study area using geostatistical modeling. Finally, these models will be applied to stack seismic reflections in a portion of the study area. Some seismic sections obtained using the geostatistical approach will be compared with those obtained by the conventional method.

5.1 Static Correction

Static corrections, or statics as normally referred to, are of vital importance for seismic reflection data processing and interpretation in land and transition zone. Statics are time shifts applied to seismic traces aiming to produce a time section that is as free as possible from artifacts or apparent structural features resulting from topography and near surface geologic variations. The correction is performed by referencing the time section to a flat datum or seismic reference datum (SRD). This reference is located at an arbitrary depth from the surface. Therefore, the depth from the surface to the reference is known, however, velocity must be known down to this depth in order to compute time shifts.

The following example shall demonstrate the importance of statics. Assume that a seismic line is acquired by collocating sources and receivers over the earth model shown in Figure 5.1. Then the resulting time section would be similar to that of Figure 5.2 that exhibits an apparent structure not representing the depth section.

Assume that SRD is located at zero elevation. Then the time shift for each collocated source and receiver will be the time it takes the seismic wave to travel from the source to SRD plus the time to travel from SRD back to the receiver. This also applies when source and receiver are located at different points on the surface. Therefore, if statics are applied to reference the section in Figure 5.2 to SRD, then the resulting section will be as shown in Figure 5.3. In this section reflections represent a flat layer similar in structure to the depth section. Thus application of statics produced a time section that is conformable with the depth section. This could not have been obtained without knowledge of the velocity from surface elevation to zero elevation. Therefore, it is important to have good knowledge of the velocity from surface to the SRD.

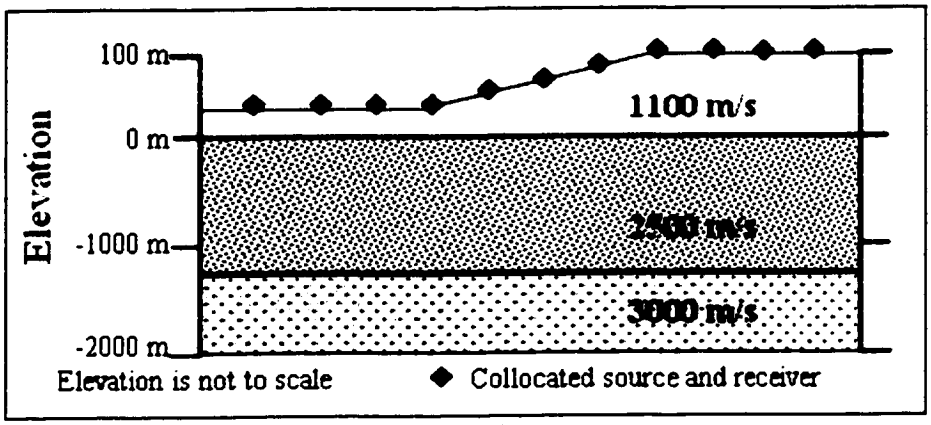

Figure 5.1: Schematic earth cross section.

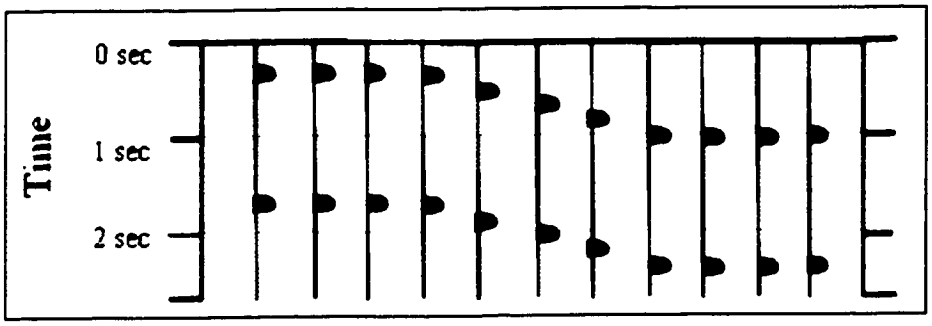

Figure 5.2: Schematic seismic section referenced to surface.

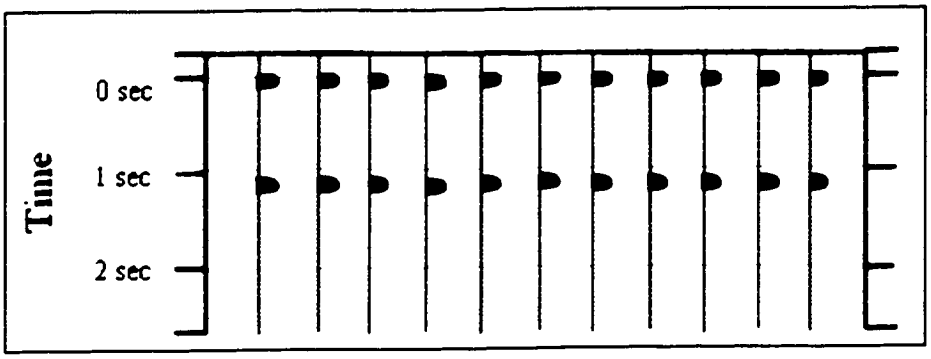

Figure 5.3: Schematic seismic section referenced to SRD.

Velocity in the near-surface is obtained from uphole surveys (Section 2.2). However, areas with near surface lateral velocity variation and sparsely spaced uphole controls require additional information to guide velocity determination. This is basically the objective for incorporating vibrator performance control data in near surface velocity

computation. Assume that near surface velocity is to be determined from surface to zero elevation for the earth model shown in Figure 5.4 using three uphole controls. No interpolation technique will adequately predict the extents of the lithologic unit penetrated by uphole number 2. Therefore, additional information is needed to guide such interpolation.

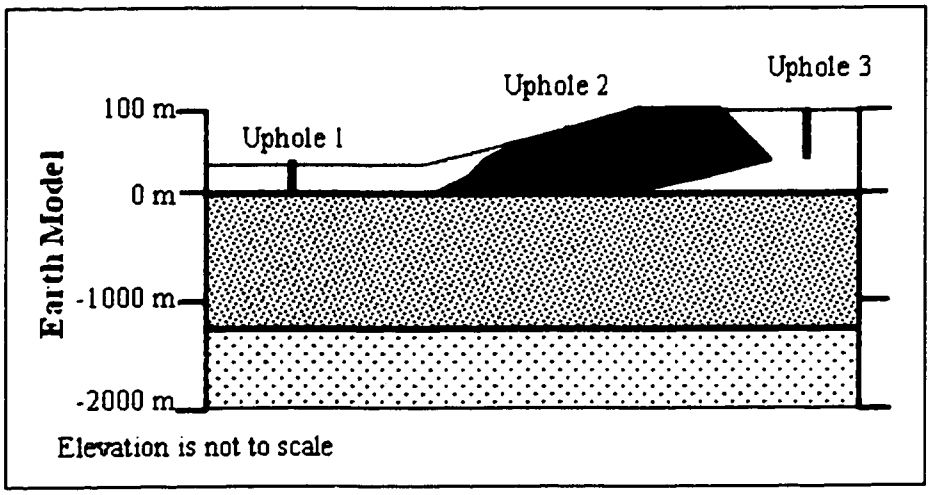

Figure 5.4: Schematic earth cross section with upholes.

5.2 3D Velocity Models Building

In this section the steps undertaken to construct two 3D velocity models will be discussed. The first model will use the uphole data while the second will incorporate uphole and seismic performance control data.

5.2.1 Model from Uphole Data

The skeleton of this model consists of voxels with areal dimensions of 120 by 120 meters and a variable vertical dimension determined by the earth thickness from surface

to SRD at any particular location. Each column or thickness is divided into 15 layers. This model will include 2,572,125 voxels: 475 in the east-west, 361 in the north-south, and 15 vertical layers. Geostatistical techniques are going to be used to estimate interval velocity in each voxel.

The 15 vertical layers were determined based on the most frequent uphole sample interval and the earth's thickness from surface to SRD. Analysis of all uphole sample intervals produced a dominant sample interval of 6 meters (Figure 5.5). The earth's thickness from surface to SRD is shown in Figure 5.6. This is obtained by subtracting the SRD elevation (Figure 5.7) from the surface elevation (Figure 3.2). It is clear from this Figure 5.6 that earth thickness goes as low as about 40 meters in the southeastern part of the study area. Therefore, the 15 vertical divisions will assure that at least one uphole sample is present in each layer knowing also that a 3 meter sample interval is the second dominant.

Therefore, the first step performed was to calculate interval velocities from uphole data as shown in Figure 5.8. Then, multidirectional semi-variograms were measured in the areal directions and a vertical semi-variogram were estimated using a lag distance of 6 meters, which is basically the dominant sample interval in the uphole data. The used areal directional semi-variograms and the vertical semi-variogram are shown in Appendix III along with their parameters.

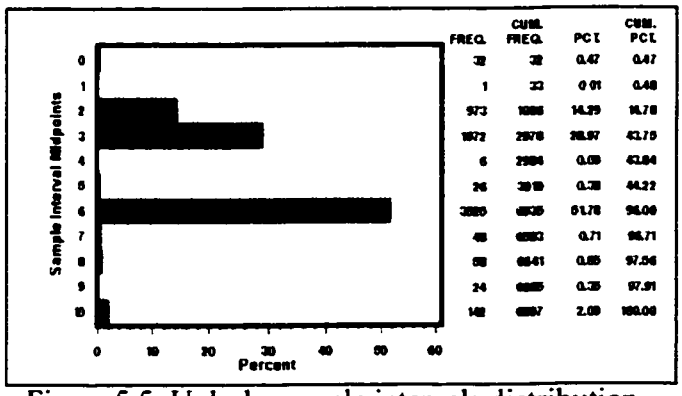

Figure 5.5: Uphole sample intervals distribution.

Figure 5.6: Earth's thickness from surface to SRD in meter.

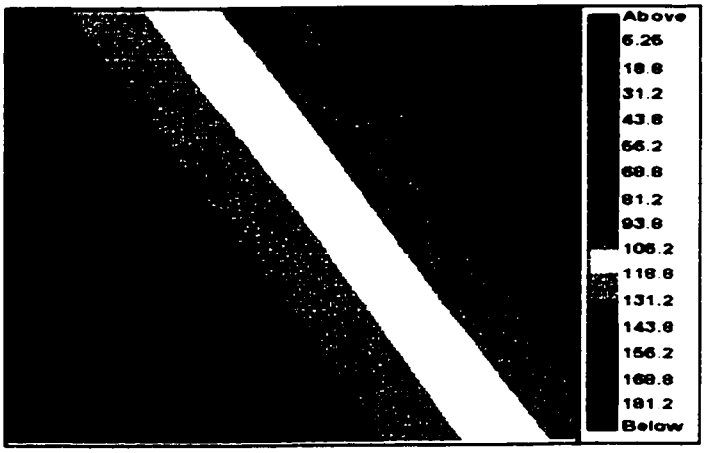

Figure 5.7: SRD elevation from MSL in meter.

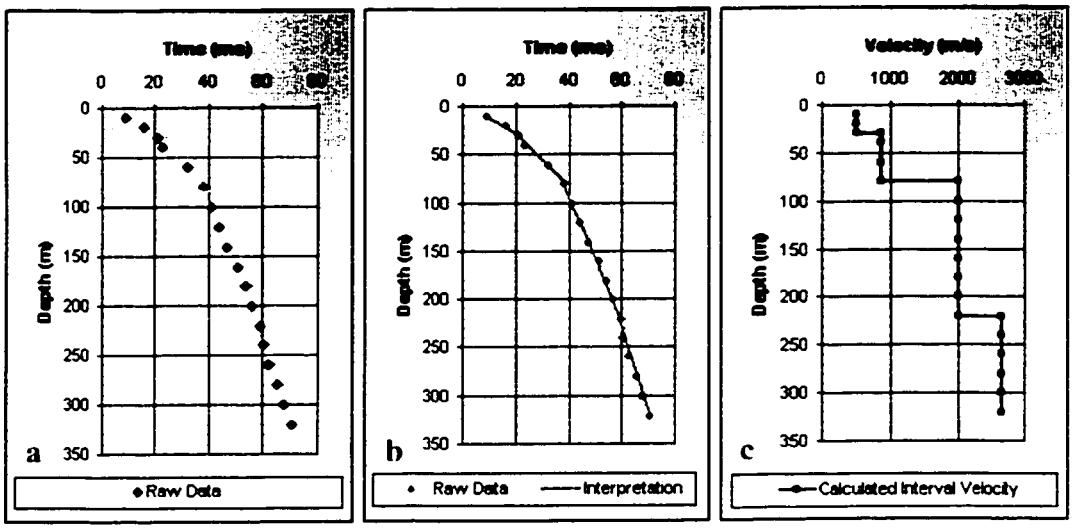

Figure 5.8: a) Raw uphole data b) Interpreted uphole data c) Calculated interval velocity from interpreted uphole data.

3D ordinary kriging was performed next. This comprises the first constructed model. Results from this model are presented in Appendix III. Statics were calculated from this model by dividing the vertical thickness of each voxel by the estimated model velocity and then summing all statics in a particular column. Figure 5.9 shows a statics map in the study area from surface to SRD.

Figure 5.9: Study area statics from surface to SRD obtained using upholes.

5.2.2 Model from Integrated Data

It was established in Section 4.1 that the maximum depth of influence of vibrator performance data is about 50 meters. Therefore, average velocity from surface to each iso-depth layer was geostatistically computed using collocated cokriging of each iso-depth uphole velocity layer and the vibrator performance control data in a similar way as in Section 4.3.2, but including all upholes. Then, interval velocity was computed in 5 layers between the resulting velocity maps where each layer has a constant thickness of 10 meters. Cross sections from this model are included in Appendix III. Following this step, travel times were computed for this 50 meter earth's thickness using the integrated model.

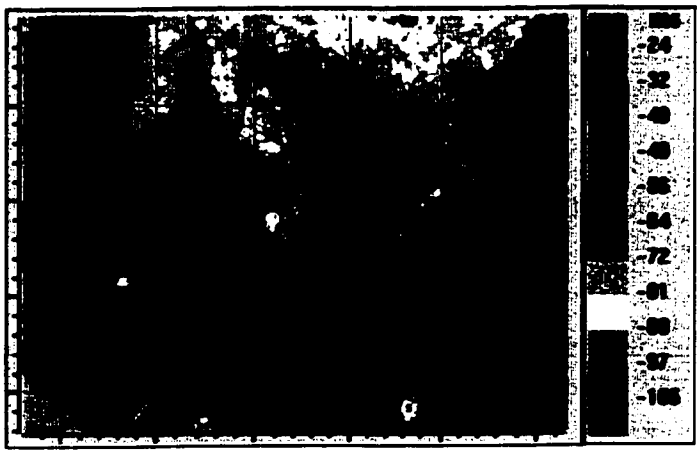

Figure 5.10: Study area statics calculated using integrated 3D velocity model.

Subsequently, 3D kriging was used to estimate interval velocity from surface to a depth of 50 meters using uphole data as in Section 5.2.1. Cross sections from this model are shown in Appendix III. Vertical travel times through this volume were then calculated. These travel times were subtracted from those obtained in the previous section

where travel times are computed from surface to SRD. This produced travel times from 50 meters below the surface to the SRD. Finally, the times obtained from the data integration step up to depth of 50 meters were added to the times from 50 meters below surface to SRD. The total times comprise the statics estimated from the integrated model. Figure 5.10 show a map of the computed statics over the study area.

5.3 Application

Seismic data from a portion of the study area, Figure 5.11, were processed using four different statics models. These include the two models described in Section 5.2 besides two other models developed by Saudi Aramco Processing Center.

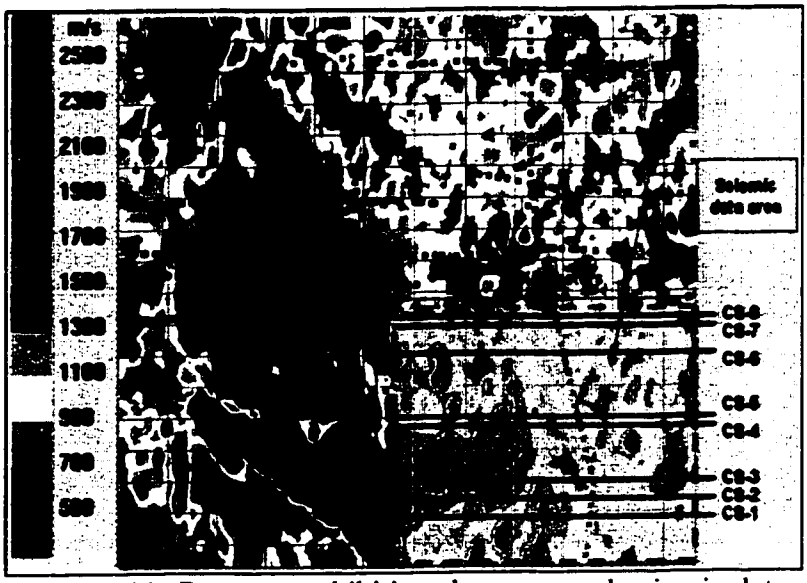

Figure 5.11: Basemap exhibiting the processed seismic data area and locations of the seismic sections. The background map shows the estimated P-wave velocity from vibrators.

The first model developed in Saudi Aramco Processing Center is called "Frozen Model". The model is built based on uphole average velocity measurements from surface to the SRD. An average velocity map is constructed based on uphole measurements that reach the SRD depth using conventional interpolation techniques such as least squares. Then this map is used to calculate statics by dividing thickness grid from surface to SRD by average velocity grid. This method does not utilize upholes which do not reach the SRD. It also produces unsatisfactory results when SRD goes above surface and when low velocity layers go deeper than SRD.

The second Saudi Aramco statics model is called "2-Layer Model". This model relies on estimating the depth of the low near surface velocity based on uphole data. Any velocity lower than 1,800 m/s is considered to be low. Then high velocities are measured from uphole data to determine the amount of localized time shifts from the depth of the low velocity layer to the SRD. These shifts can be applied if SRD is above or below surface. However, in the study area this approach has not sufficiently resolved the statics problems. Therefore, an approach that relied on integrating the 2-Layer Model with the geology of the area was utilized. This method required addition of about 400 pseudo upholes to the study area in order to control velocity estimation whenever needed. Figure 5.12 shows the density of the added pseudo upholes. As can be inferred, this method required a lot of interpretation and human intervention. It also required several iterations before converging to an acceptable model. Every iteration required a model building followed by application of this model to stack the seismic data which resulted in a lengthy time period, requiring manpower and computer time.

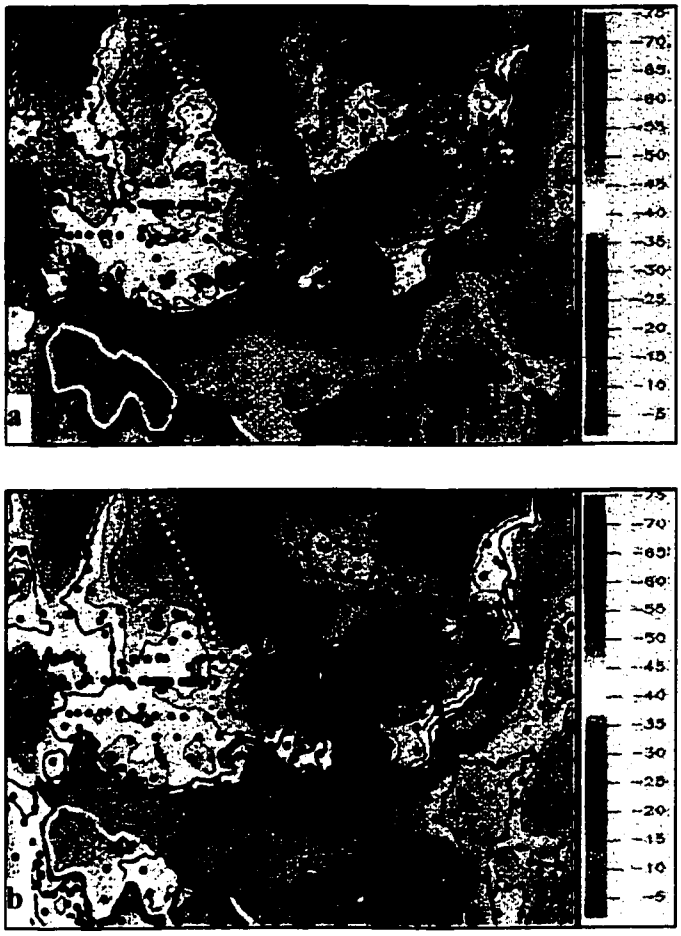

Figure 5.12: a) 2-Layer Model with real upholes posted b) 2-Layer Model and geology incorporation with pseudo uphole posted. Contour interval is -5 ms.

It should be pointed out that the SRD used in building the geostatistical models was 50 meters below Saudi Aramco's SRD to avoid the case when SRD goes above surface.

Figure 5.13 shows a seismic section along line CS-5. Four stacks of this line were produced using the previously described four models. The Frozen Model's stack seems to be poor compared to the other models. The 2-Layer Model produced results that are comparable to the results obtained from the 3D kriged model. The integrated model showed more improvements than the 2-Layer Model and the 3D kriged model. It handled the medium and long wavelengths statics better. Automatic statics was performed using

these statics models excluding the Frozen Model. Figure 5.14 shows 3 seismic sections obtained from the three statics models after the application of automatic statics. It is obvious that better results are obtained from the integrated model.

Figure 5.15 shows a seismic section along line CS-8 which runs over an area that has good uphole controls. The 3D kriged and the integrated models show similar results, both being better than the 2-Layer Model. They produced continuous horizons compared to broken ones exhibited by the 2-Layer Model stack. It should be noted that with good uphole controls, the integrated model did as good as the 3D kriged model. Figure 5.16 shows stacks from this line after the application of automatic statics.

Generally, based on analyzing seismic data from all the reprocessed area, it was concluded that the integrated model has consistently produced better results than the 2-Layer Model. The 3D kriged model produced results comparable with those obtained when using the integrated model in areas with good uphole controls. As a rule, the integrated model has resolved medium and long wavelengths statics more than the other two models.

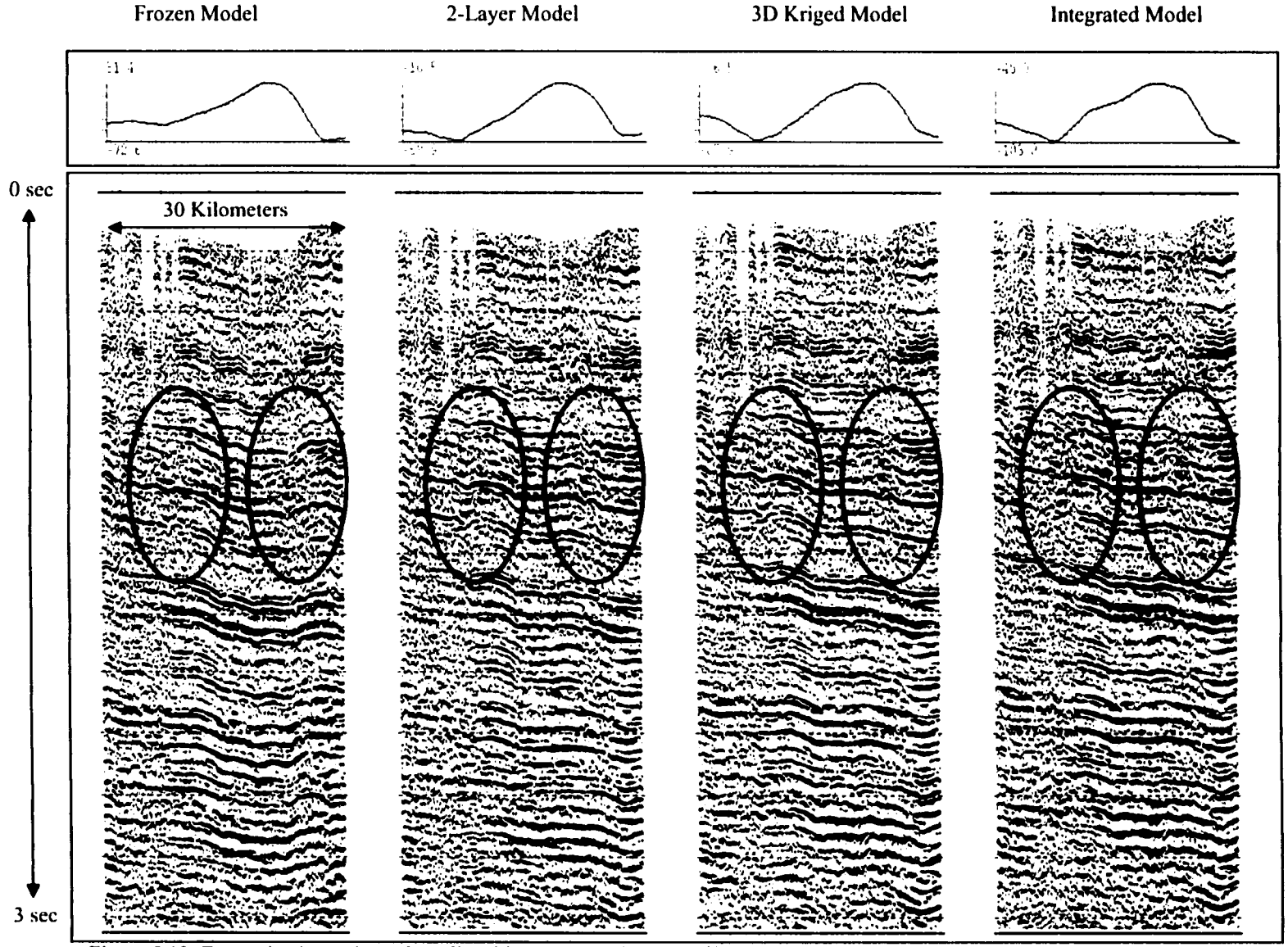

Figure 5.13: Four seismic sections along line CS-5 processed using different statics models. Curves on the top show total CMP statics mean in ms.

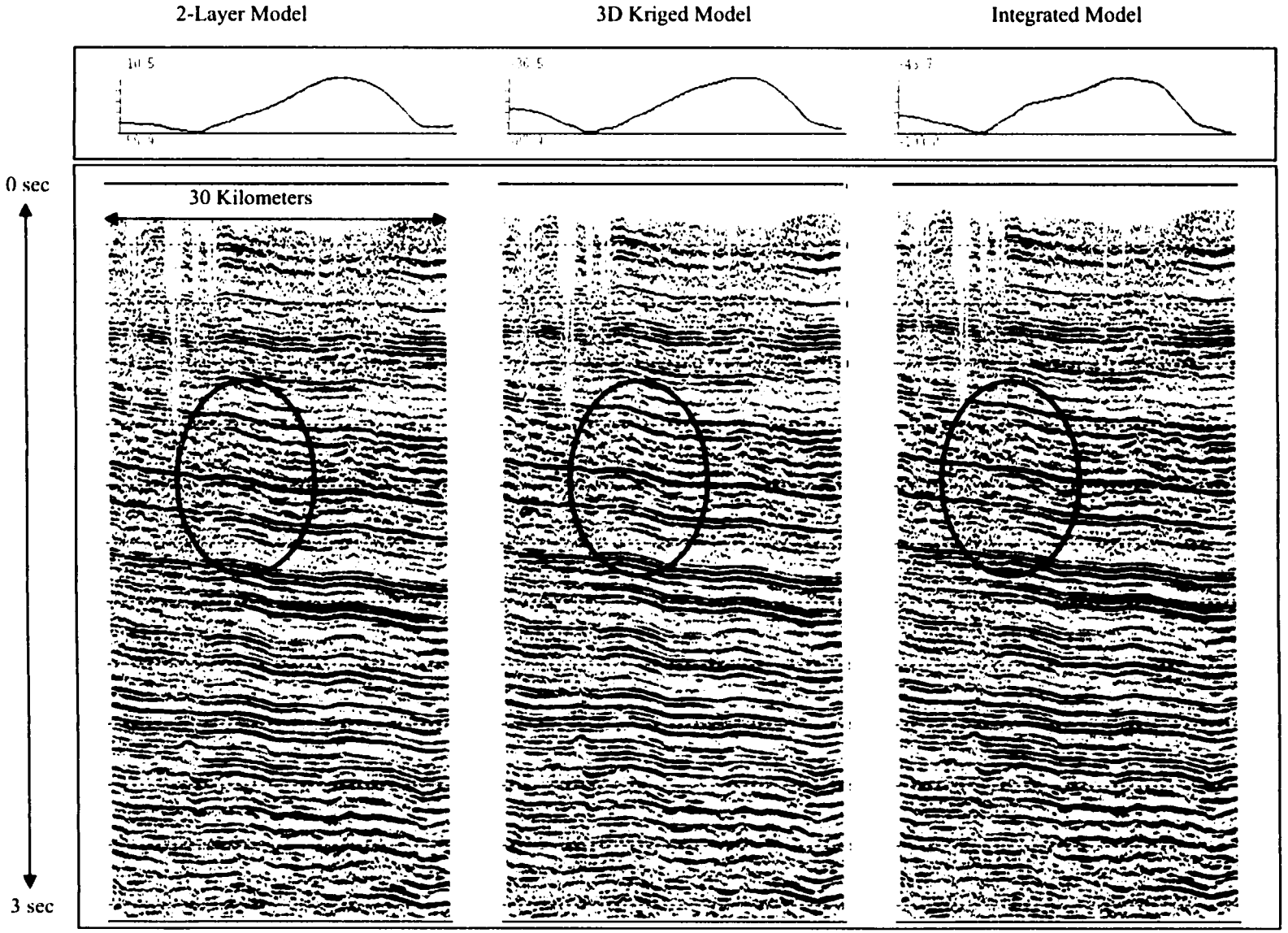

Figure 5.14: Three seismic sections along line CS-5 processed using different statics models with automatic statics applied. Curves on the top show total CMP statics mean in ms.

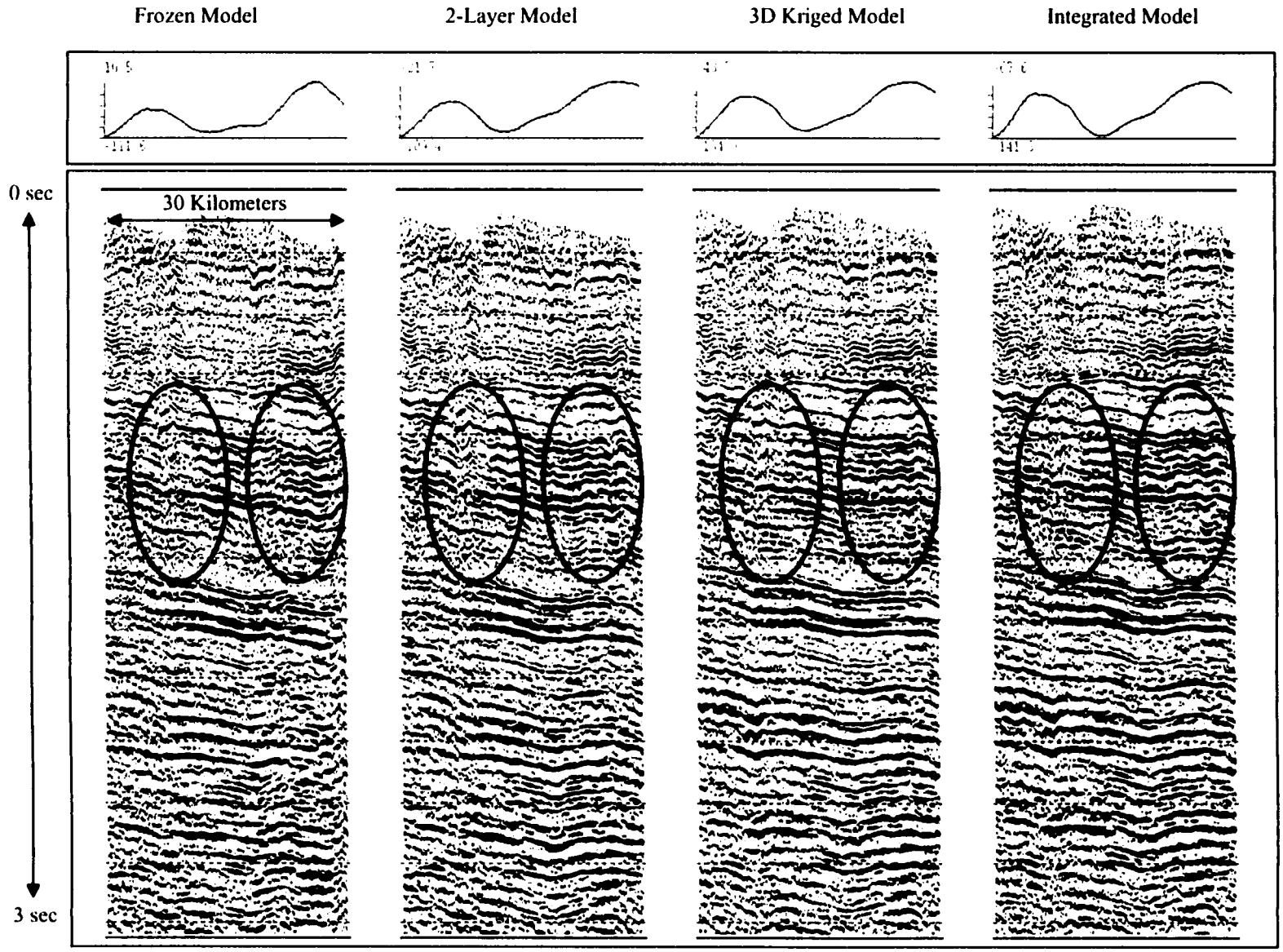

Figure 5.15: Four seismic sections along line CS-8 processed using different statics models. Curves on the top show total CMP statics mean in ms.

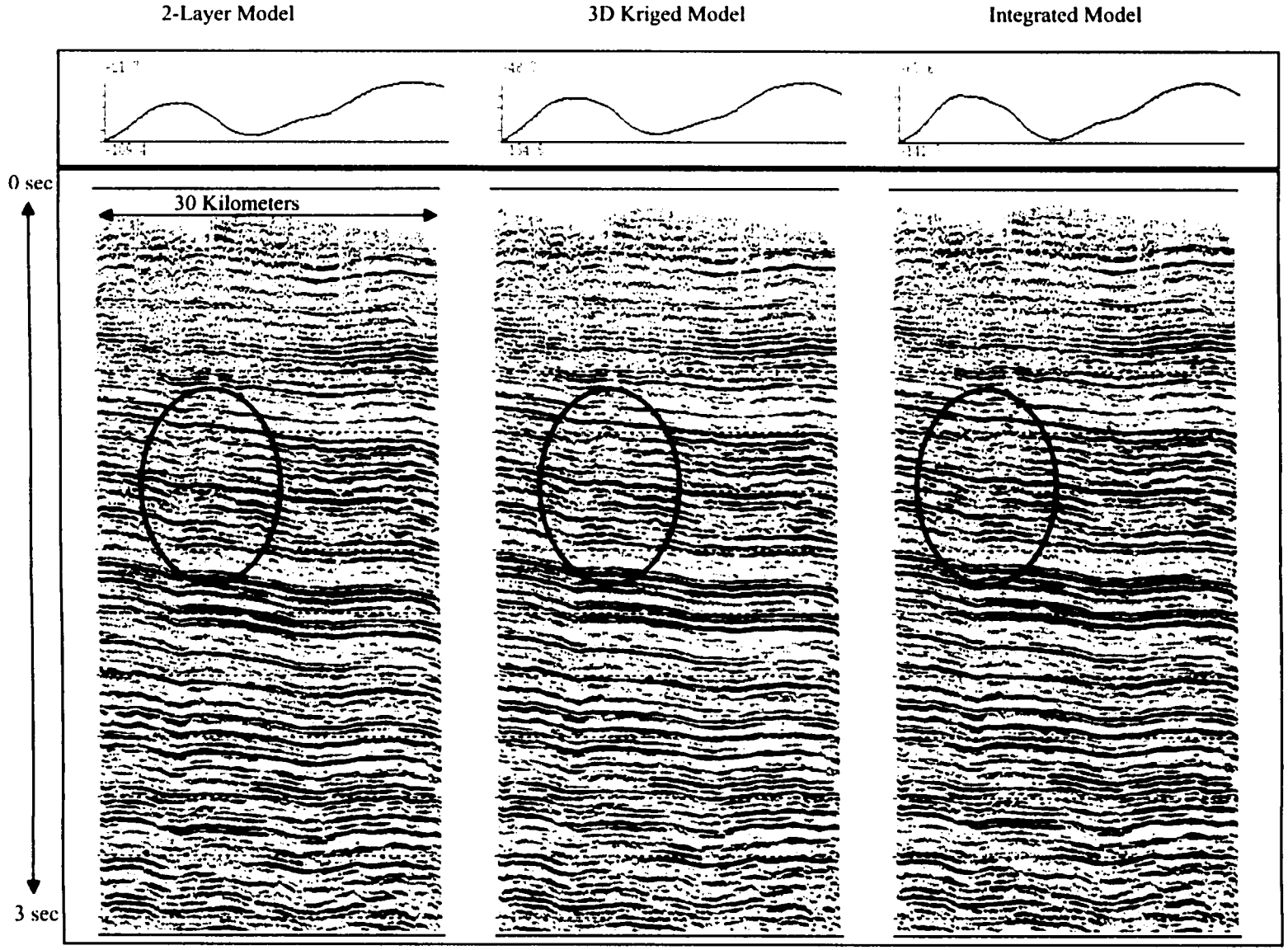

Figure 5.16: Three seismic sections along line CS-8 processed using different statics models with automatic statics applied. Curves on the top show total CMP statics mean in ms.

5.4 Regional Application

To test the application of using vibrator estimated V_p to other areas, uphole and vibrator performance control data from two areas in Saudi Arabia (Figure 5.17) were analyzed. The vibrator performance control data were processed following the same steps as described in Chapter 3.

For Area 1, iso-depth velocities to 20 meter depth were calculated from uphole data (65 upholes) and correlated with the vibrator estimated V_p. The estimated V_p map is shown in Figure 5.18a while the cross correlation with uphole data in Figure 5.18b. The obtained correlation coefficient was 0.6 which is acceptable for data integration.

Figure 5.19a shows the estimated V_p from vibrator measurements for Area 2. Iso-depth 30 meter velocities were calculated from the existing 15 upholes in the area and cross correlated with the estimated V_p (Figure 5.19b). An acceptable correlation coefficient of 0.65 was obtained.

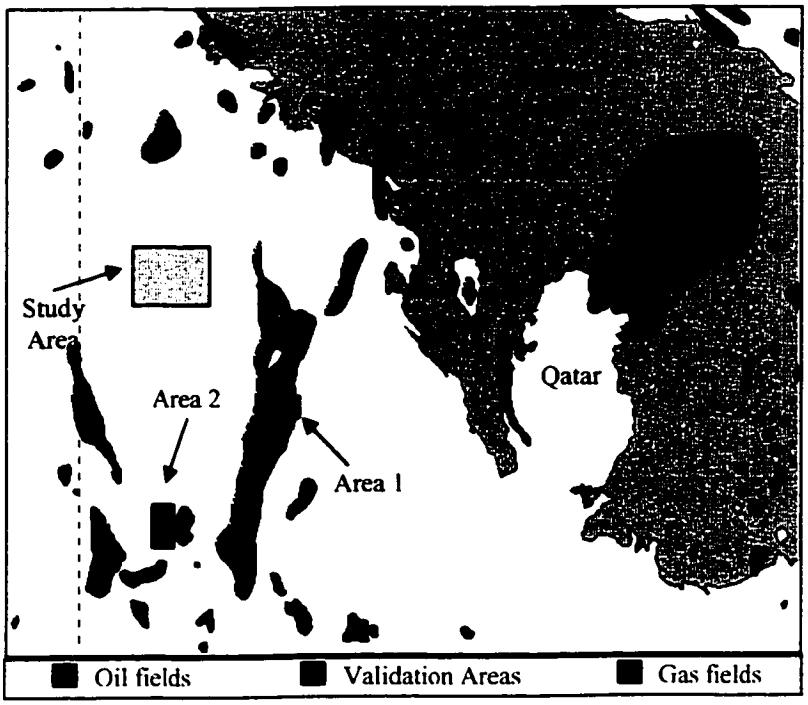

Figure 5.17: Study area location map.

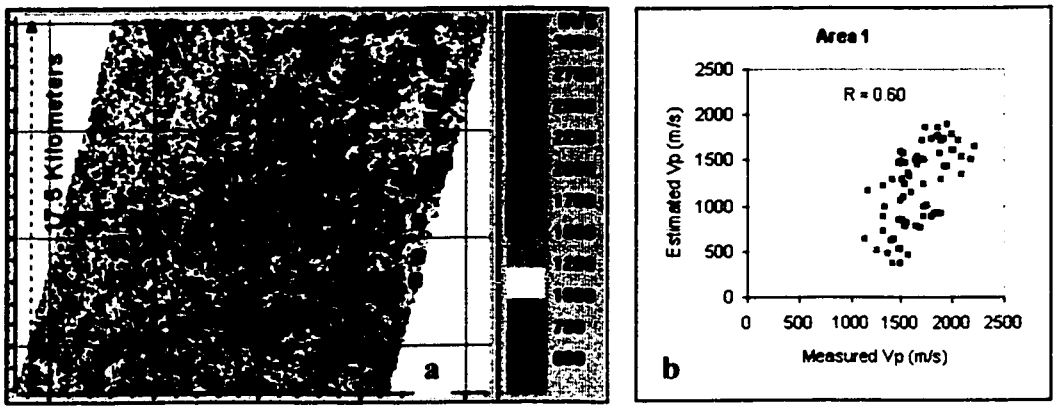

Figure 5.18: a) Area 1 estimated V_p map and uphole locations b) Crossplot of uphole measured velocities and estimated V_p.

It can be concluded based on the above two examples, that the estimated V_p from vibrator measurements has a fair correlation with uphole velocities. The correlation magnitude varies from one area to another and also with the number of uphole controls.

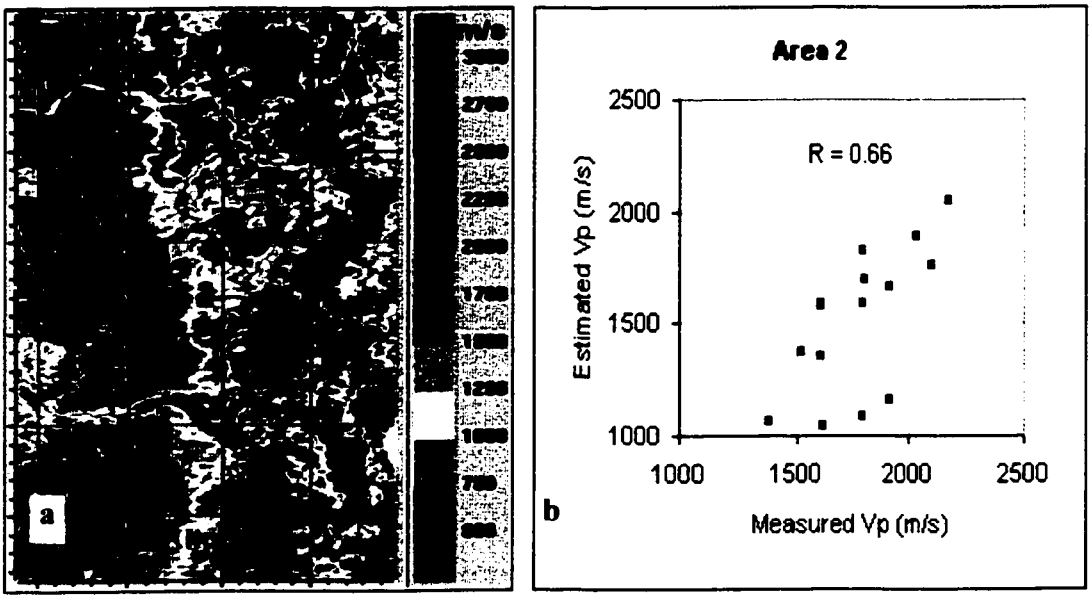

Figure 5.19: a) Area 2 estimated V_p map and uphole locations b) Crossplot of uphole measured velocities and estimated V_p.

CHAPTER 6

CONCLUSIONS AND RECOMMENDATIONS

6.1 Conclusions

The following conclusions can be drawn from the previous analyses and results:

1. Geostatistical techniques proved to be useful in estimating near surface velocity distributions and resulted in better velocity models than those obtained from conventional techniques.
2. There is a good correlation between P-wave velocities estimated from vibrator ground parameters and direct measurements of velocities by uphole surveys.
3. An analytical technique was established to estimate P-wave velocity from vibrator measured ground parameters.
4. P-wave velocity estimated from vibrator measurements can be used to improve determination of near surface velocity when integrated with uphole measurements.

This integrated velocity model can be used to derive statics and then to stack the seismic data.

5. Data integration is especially important in areas with sparse uphole controls.
6. The proposed technique is superior to geostatistical estimations based on uphole data alone or using a more elaborated conventional manual technique.
7. Near surface velocity modeling through geostatistical techniques significantly reduced the turn around time and the required manpower.
8. 3D geostatistical modeling honors all uphole controls regardless of their penetration depths.
9. Integration of estimated P-wave velocity from vibrator measured ground parameters reduces medium and long wavelength statics more than using only uphole data.

6.2 Recommendations

Based on this study, we recommend the following measures:

1. Ground parameters: stiffness and viscosity measured by vibrator performance control system are of vital importance, thus they have to be provided to the client. They can be added in a separate file to the survey acquisition geometry files known as SPS files (Shell Processing Support) and delivered to the processing center where they should be properly handled and archived.
2. The geostatistical approaches used in this study should be implemented when calculating statics. This can be done in two ways:

   a. Use geostatistical techniques (kriging) to calculate statics in areas where reasonable upholes are present.
   b. Incorporate (by cokriging) vibrator measured ground parameters into statics calculation in areas with sparse uphole control.

3. Use vibrator-measured ground parameters to check uphole measurements, especially in case of suspicious uphole velocities.
4. Use the statistical quality control approach discussed in this study to assess the quality of vibrator performance control data. Interactive computer software package can be developed to perform this task.
5. Further research is needed to understand the depth of influence of vibrator ground parameters measurements. One possible approach could be to analyze the Rayleigh waves dispersion and determine the influence depth by assuming it to be equal to half Rayleigh wavelength.
6. Although this study used vibrator performance control data obtained from a 3D vibroseis seismic survey, 2D vibroseis seismic lines can also be improved by integrating vibrator and uphole data.
7. Vibrator performance control data, whenever available should be used in surface geological studies because of their sensitivity to near surface variations.

Dhahran, Saudi Arabia
September 11, 2002

King Fahad University of Petroleum & Minerals
Deanship of Graduate Studies
Office of the Dean

Subject: Thesis Modification Acknowledgment

This letter is written to acknowledge that page number 108 of the thesis titled "Use of Vibrator Performance Data to Improve Near-Surface Velocity Determination" submitted to the Graduate Studies Office in May 2002 is not missing. However, there was a skip in the numbering from page 107 to page 109.

I apologize for the inconvenience caused by this matter.

Regards

Mustafa N. Al-Ali
ID # 887580
Thesis Author

c.c. Dean of the Library Affairs, Building 8

REFERENCES

Al-Ali, M. N. et al., 2001, Conventional and Sparse 3D: What is in between?, SEG Annual Meeting, San Antonio, September 2001.

Al-Sayari, S. S. and Zötl, J. G., 1978, Quaternary Period in Saudi Arabia. Springer-Verlag, Wien New York.

Armstrong, M., 1998, Basic Linear Geostatistics. Springer, Berlin.

Arya, S. et al., 1979, Design of Structures and Foundations for Vibrating Machines. Gulf Publishing Company, Houston.

Baeten, G. and Ziolkowski, A., 1990, The Vibroseis Source. Elsevier, Amsterdam.

Baliguet, P., 1992, Overview of different ways of controlling vibrators, and effects on Q. C. measurements, EAEG Annual Meeting, Vibroseis Workshop, Paris, June 1992..

Berg, G. V., 1989, Elements of Structural Dynamics. Prentice Hall, Inc., Englewood Cliffs, New Jersey.

Brown, G. L. and Moxley, S. D., 1964, Hydraulic Servomechanisms as Seismic Energy Sources: IEEE, March 23-26.

Buchholdt, H., 1997, Structural Dynamics for Engineers. Thomas Telford, London.

Clark, I., 1979, Practical Geostatistics. Applied Science Publisher LTD, London.

Cox, M., 1999, Static Corrections for Seismic Reflection Surveys. Society of Exploration Geophysicists, Tulsa, Oklahoma.

Garotta, R. and Marin, D., 1992, Adaptation of vibroseismic to local recording conditions, EAEG Annual Meeting, Paris, June 1992.

Garotta, R., 1990, New development and perspectives in vibroseismic, SEG Annual Meeting, San Francisco, September 1990.

Goovaerts, P., 1997, Geostatistics for Natural Resources Evaluation. Oxford University Press, New York.

Isaaks E. and Srivastava R., 1989, An Introduction to Applied Geostatistics. Oxford University Press, New York, NY.

Kitanidis, P. K., 1997, Introduction to Geostatistics. Cambridge University Press, New York.

Lerwill, W. E., 1981, The Amplitude and Phase Response of a Seismic Vibrator: Geophysical Prospecting, 29, 503-528.

Marsal, D., 1987, Statistics for Geoscientists. Pergamon Press, Oxford.

Martin, J. E. and Jack, I. G., 1990, The Behavior of a Seismic Vibrator Using Different Phase Control Methods and Drive Levels: First Break, 8, 404-414.

Meunier, J. et al., 1996, Quality Control and Attribute Analysis on a 3D Vibroseis Crew, SEG Annual Meeting, Denver, 1996.

Miller, G. F. and Pursey, H., 1955, On the partition of energy between elastic waves in a semi-infinite solid, Proceedings of the Royal Society (London), A223, 68.

Postel, J. J. et al., 1996, Quality Control on a 3D vibroseismic crew, EAEG Annual Meeting, Amsterdam, June 1996.

Powers, R. W., 1968, Arabie Seoudite Lexique Stratigraphique Internationale. III, 10b, p.1-177, Paris.

Reynolds, D. D., 1981, Engineering Principles of Acoustics. Allyn and Bacon, Inc., Boston.

Richart, F. E. et al., 1970, Vibrations of Soils and Foundation. Prentice-Hall, Inc., Englewood Cliffs, New York.

Sallas, J. J. and Weber, R. M., 1982, Comments on "The Amplitude and Phase Response of a Seismic Vibrator" by W. E. Lerwill: Geophysical Prospecting, 30, 731-740.

Sallas, J. J., 1984, Seismic vibrator control and the down-going P-wave: Geophysics, 49, 731-740.

Schrodt, J. K., 1987, Techniques for Improving Vibroseis Data: Geophysics, 52, 469-482.

Sercel VE432 Vibrator Control System Manual Training Manual, Massy, August 1999.

Seriff, A. J. and Kim, W. H., 1970, The effect of harmonic distortion in the use of vibratory surface sources, Geophysics Vo. 35, No. 2, 234-246.

Thigpen, B. B. et al., 1975, Special report of the subcommittee on polarity standards. Geophysics 40, 694-699.

Waters, K. H., 1981, Reflection Seismology. John Wiley & Sons, New York.

Weijermars, R., 1999, Surface Geology, Lithostratigraphy and Tertiary Growth of the Dammam Dome, Saudi Arabia: A New Field Guide: GeoArabia, Vol. 4, No. 2, 199-226.

Wheeler, D. J., 1995, Advanced Topics in Statistical Process Control. SPC Press, Knoxville, Tennessee.

Whybrow, P. J. et al., 1987, Miocene stratigraphy, Geology and Flora (Algae) of Eastern Saudi Arabia and the Ad Dabtiyah Vertebrate Locality: Bull. Br. Mus. Nat. Hist. (Geol.) 41 (4), 371-382.

APPENDIX I

Area of Interest Geomorphic Features Photographs

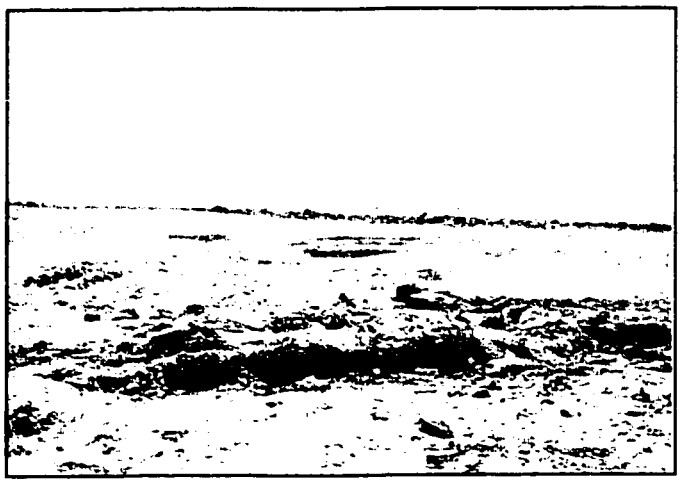

Figure I.1: Photograph No. 2 silty sand surface.

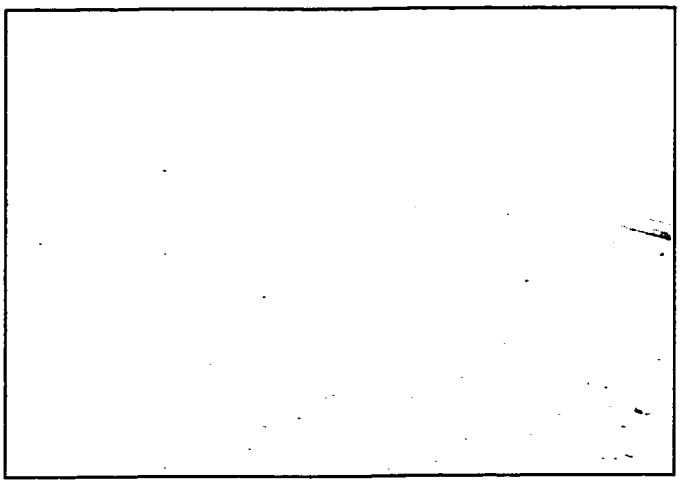

Figure I.2: Photograph No. 3 surface with hard sandstone cover.

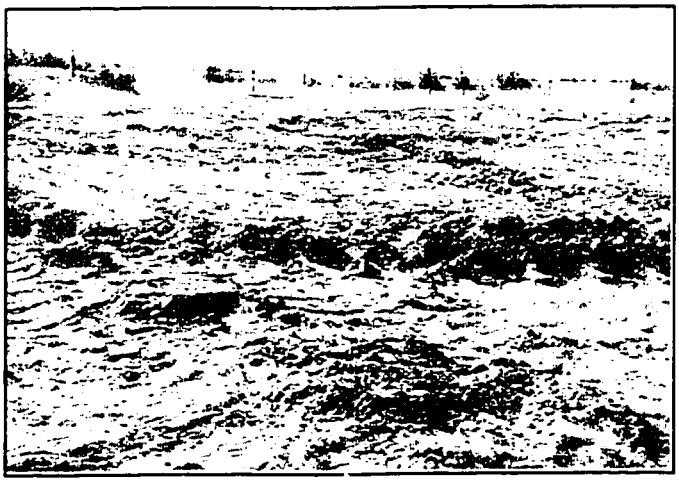

Figure I.3: Photograph No. 4 fine to medium grain silty sand surface.

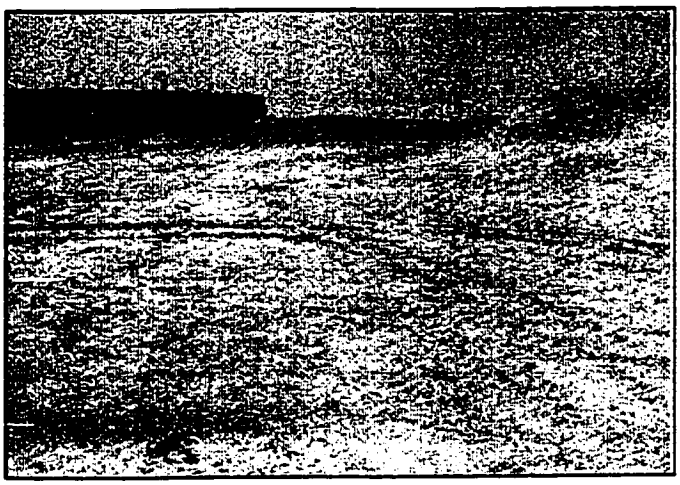

Figure I.4: Photograph No. 5 fine grain silty sand surface with some surrounding hills.

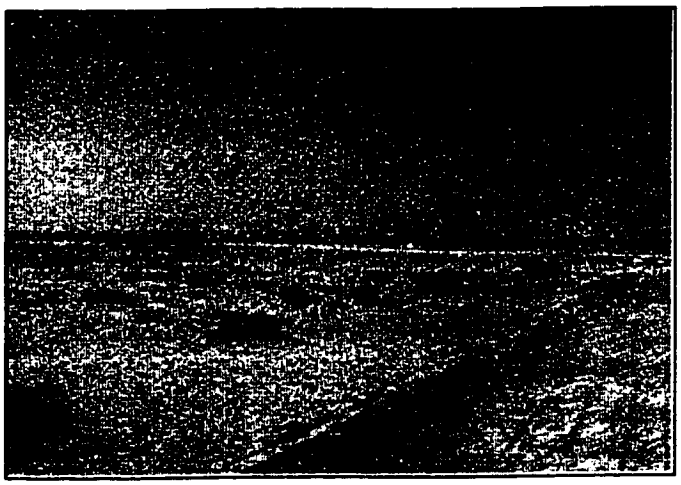

Figure I.5: Photograph No. 6 hard limestone covered with thin sand layer.

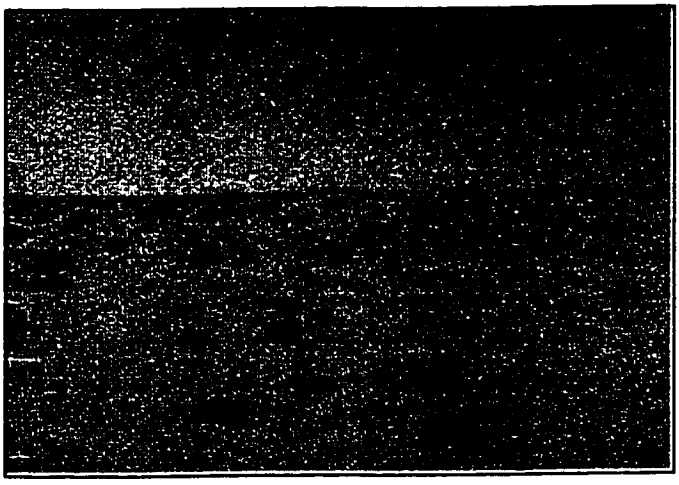

Figure I.6: Photograph No. 7 fine sand with gravels.

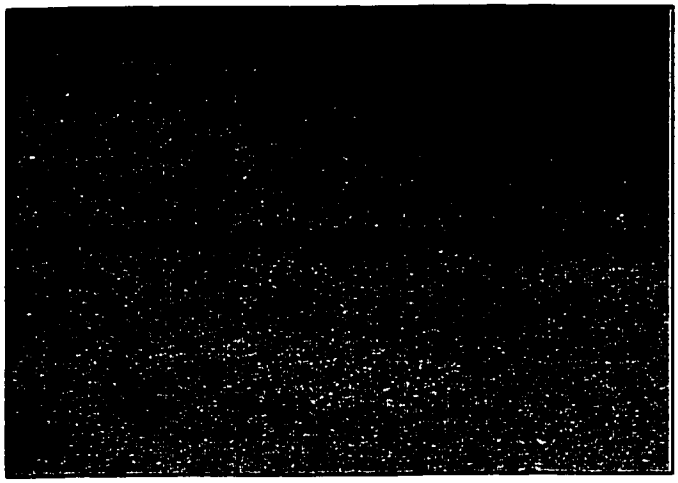

Figure I.7: Photograph No. 8 fine grain sand with gravels.

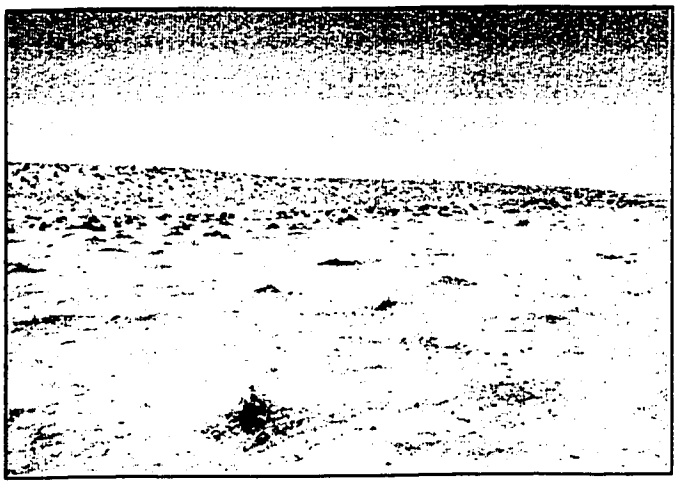

Figure I.8: Photograph No. 9 relatively soft sand with some vegetation.

Figure I.9: Photograph No. 10 sand with gravels covering a hard rock surface.

Figure I.10: Photograph No. 11 hills covered with silty sand and gravels.

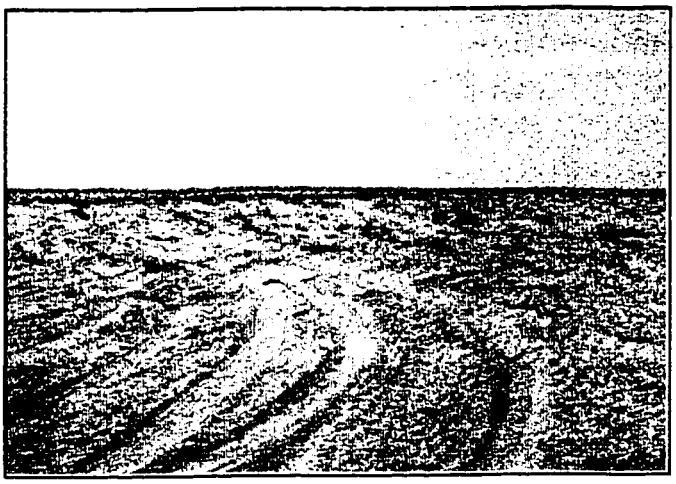

Figure I.11: Photograph No. 12 soft sand with some vegetation.

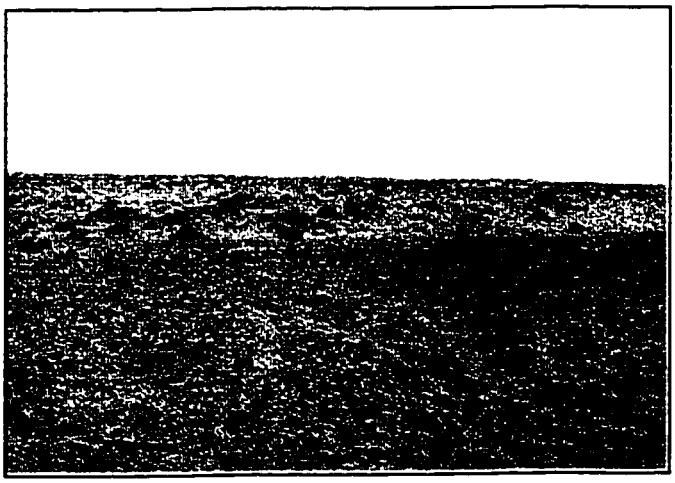

Figure I.12: Photograph No. 13 sand with gravels on a hill's plateau.

Figure I.13: Photograph No. 14 hills covered with silty sand and gravels.

Figure I.14: Photograph No. 15 Silty sand and gravels covered hills.

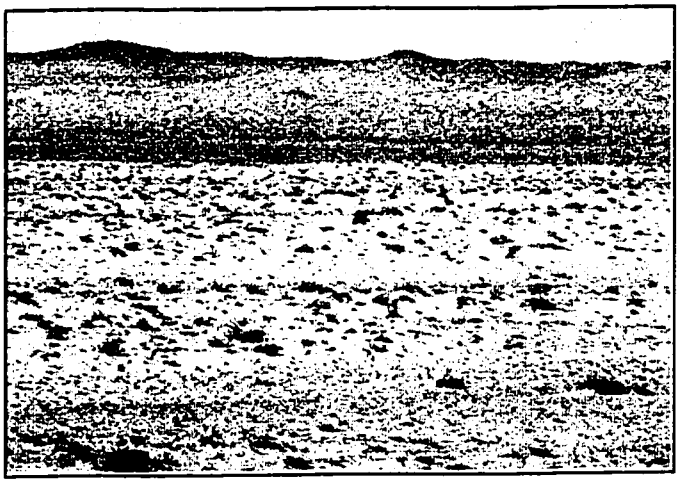

Figure I.15: Photograph No. 17 sand with gravels with hills showing Hadrukh outcrop.

Figure I.16: Photograph No. 18 Hofuf Formation outcrop sample-1 location.

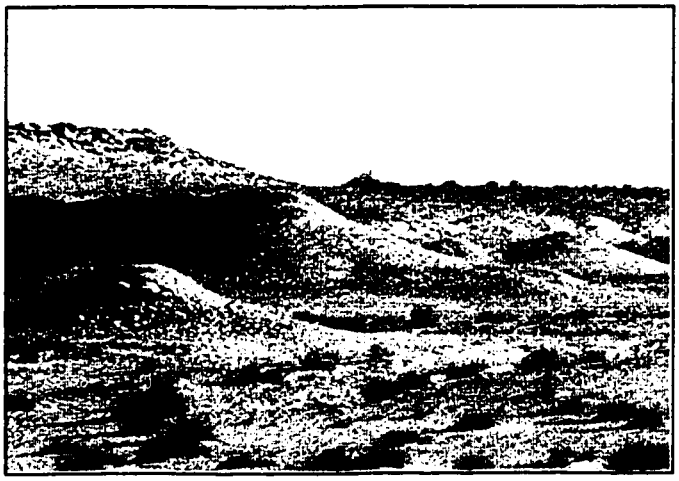

Figure I.17: Photograph No. 19 Dam Formation outcrop.

Figure I.18: Photograph No. 20 Hadrukh Formation sample-2 location.

Figure I.19: Photograph No. 21 Hadrukh Formation outcrop sample-3 location.

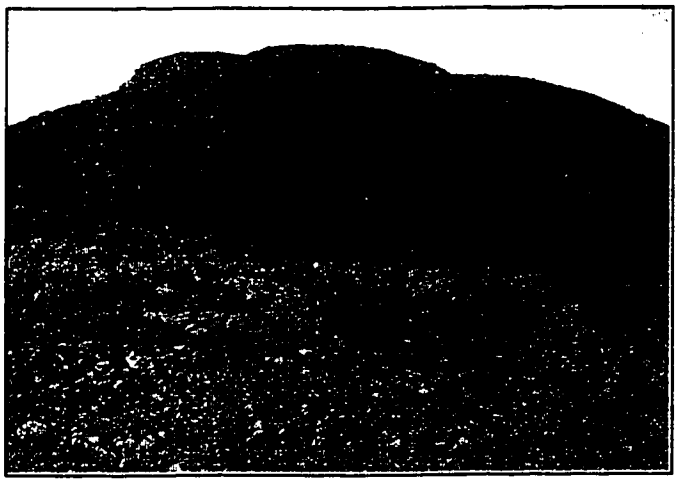

Figure I.20: Photograph No. 22 Dam Formation outcrop sample-4 location.

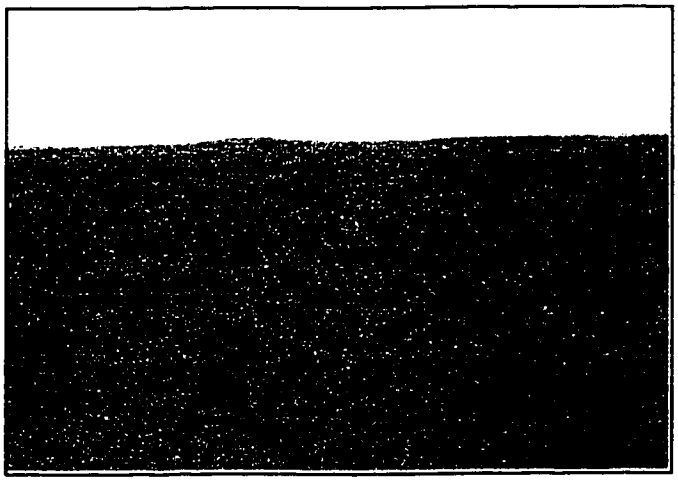

Figure I.21: Photograph No. 23 Sand and gravel plain.

APPENDIX II

Vibrator Performance Control Data Univariate Statistics

	Average Phase	Maximum Phase	Average Distortion	Maximum Distortion	Average Force	Maximum Force	Ground Viscosity	Ground Stiffness	Shear Velocity
Mean	0.74	0.79	15.35	27.86	68.46	72.38	676310	2.17E+08	585.98
Median	1	1	15	24	69	72	633750	1.87E+08	396.41
Mode	1	-2	10	16	69	72	463125	1.50E+08	396.41
Standard Deviation	0.64	2.91	4.87	13.50	1.90	1.49	241326	1.31E+08	449.41
Variance	0.41	8.48	23.75	182.29	3.61	2.21	5.82E+10	1.72E+16	201972
Kurtosis	9637.91	221.96	7.13	6.83	199.22	614.22	6.82	8.80	4.79
Skewness	63.89	1.34	1.05	1.65	-7.84	-10.55	0.96	1.95	1.49
Range	120	359	99	99	74	129	5094375	1.59E+09	4102.61
Minimum	0	-179	0	0	0	0	121875	6.24E+06	10.16
Maximum	120	180	99	99	74	129	5216250	1.59E+09	4112
No. Samples	1003645	1003645	1003645	1003645	1003645	1003645	1003645	1003645	1003645
CV	0.8734	3.6699	0.3176	0.4847	0.0277	0.0205	0.3568	0.6022	0.7669

Table II.1: Univariate statistics for raw data.

	Average Phase	Maximum Phase	Average Distortion	Maximum Distortion	Average Force	Maximum Force	Ground Viscosity	Ground Stiffness	Shear Velocity
Mean	0.73	0.79	15.33	27.76	68.48	72.38	670015.2	2.17E+08	589.30
Median	1	1.00	15	24	69	72	6.34E+05	1.87E+08	396.41
Mode	1	-2	10	16	69	72	463125	1.50E+08	396.41
Standard Deviation	0.65	2.85	4.87	13.43	1.88	1.41	232938.8	1.29E+08	452.47
Variance	0.42	8.13	23.70	180.31	3.55	1.98	5.42E+10	1.66E+16	2.05E+05
Kurtosis	9839.24	244.98	7.20	6.81	199.21	728.11	6.40	8.36	4.77
Skewness	65.21	1.32	1.06	1.64	-7.83	-12.93	0.79127	1.90	1.49
Range	120	359	99	99	72	129	5094375	1.59E+09	4102.61
Minimum	0	-179	0	0	0	0	1.22E+05	6.24E+06	10.16
Maximum	120	180	99	99	72	129	5.22E+06	1.59E+09	4112.78
No. Samples	939081	939081	939081	939081	939081	939081	939081	939081	939081
CV	0.8881	3.6130	0.3176	0.4838	0.0275	0.0194	0.3476	0.5953	0.7678

Table II.2: Univariate statistics for data after visual editing.

	Average Phase	Maximum Phase	Average Distortion	Maximum Distortion	Average Force	Maximum Force	Ground Viscosity	Ground Stiffness	Shear Velocity
Mean	0.71	0.64	14.85	26.18	68.71	72.30	6.77E+05	2.14E+08	580.60
Median	1.00	1.00	14.00	23.00	69.00	72.00	6.34E+05	1.87E+08	396.41
Mode	1.00	-2.00	10.00	16.00	69.00	72.00	4.88E+05	1.68E+08	396.41
Standard Deviation	0.46	2.53	4.32	11.03	1.16	1.06	2.28E+05	1.17E+08	445.01
Variance	0.21	6.39	18.68	121.63	1.34	1.12	5.18E+10	1.37E+16	198032.10
Kurtosis	1.91	2.2	2.75	3.96	11.05	3.41	2.28	6.21	4.96
Skewness	-0.83	0.28	0.58	1.10	-2.49	0.51	0.44	1.58	1.53
Range	3.00	27.00	28.00	81.00	12.00	13.00	1.71E+06	1.00E+09	4102.61
Minimum	0.00	-12.00	6.00	10.00	59.00	67.00	1.22E+05	6.24E+06	10.16
Maximum	3.00	15.00	34.00	91.00	71.00	80.00	1.83E+06	1.01E+09	4112.78
No. Samples	893135	893135	893135	893135	893135	893135	893135	893135	893135
CV	0.6512	3.9488	0.2910	0.4212	0.0168	0.0146	0.3359	0.5481	0.7665

Table II.3: Univariate statistics for data after the three-sigma application.

	Average Phase	Maximum Phase	Average Distortion	Maximum Distortion	Average Force	Maximum Force	Ground Viscosity	Ground Stiffness	Shear Velocity
Mean	0.71	0.63	14.86	26.27	68.69	72.31	6.78E+5	2.13E+08	606.70
Median	0.75	0.62	14.90	26.64	68.79	72.35	6.59E+5	1.91E+08	475.67
Mode	1.00	0.66	12.40	20.06	69.00	72.49	5.15E+5	1.24E+08	284.88
Standard Deviation	0.20	0.76	2.61	5.51	0.45	0.50	1.56E+5	75244594	324.97
Variance	0.04	0.58	6.82	30.38	0.20	0.25	2.4E+10	5.66E+15	105605.30
Kurtosis	3.64	3.43	2.15	2.29	7.04	3.11	2.79	5.52	3.70
Skewness	-0.94	0.22	-0.09	-0.06	-1.42	-0.19	0.59	1.56	1.25
Range	1.30	7.39	14.35	36.85	5.97	4.09	1.06E+6	6.33E+08	2029.97
Minimum	0.00	-2.50	8.92	14.02	63.99	70.62	3.67E+5	2.91E+07	65.22
Maximum	1.30	4.89	23.27	50.88	69.96	74.72	1.43E+6	6.62E+08	2095.19
No. Samples	175747	175747	175747	175747	175747	175747	175747	175747	75145
CV	0.2834	1.2022	0.1757	0.2097	0.0065	0.0069	0.2304	0.3532	0.5356

Table II.4: Univariate statistics for data after smoother application.

Histogram plots were generated for the ground stiffness data at different phases as shown in Figures II.1, II.2, II.3 and II.4. These displays assist in gaining more insight about each data quality assessment step by means of observing the data distribution.

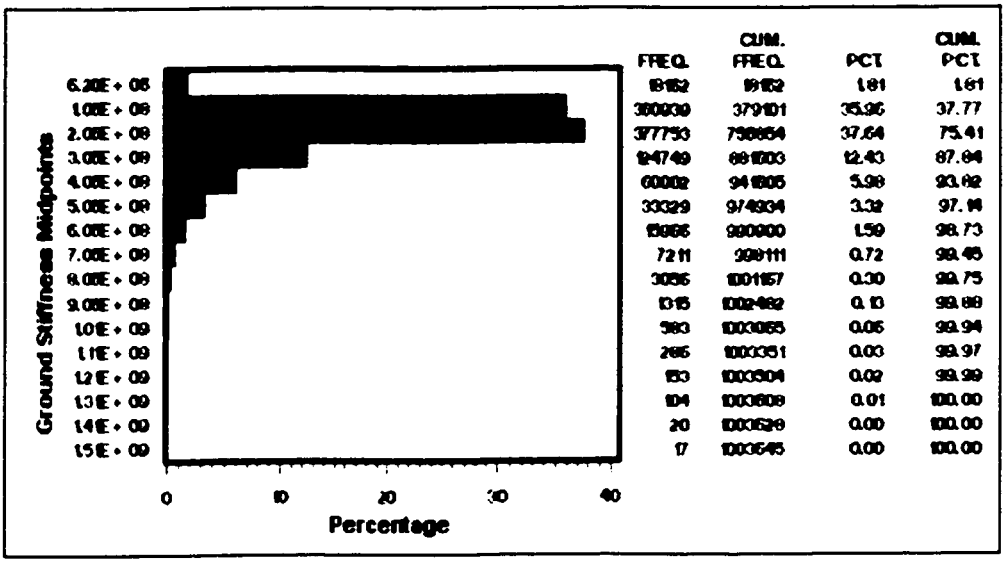

Figure II.1: Histogram of raw ground stiffness data.

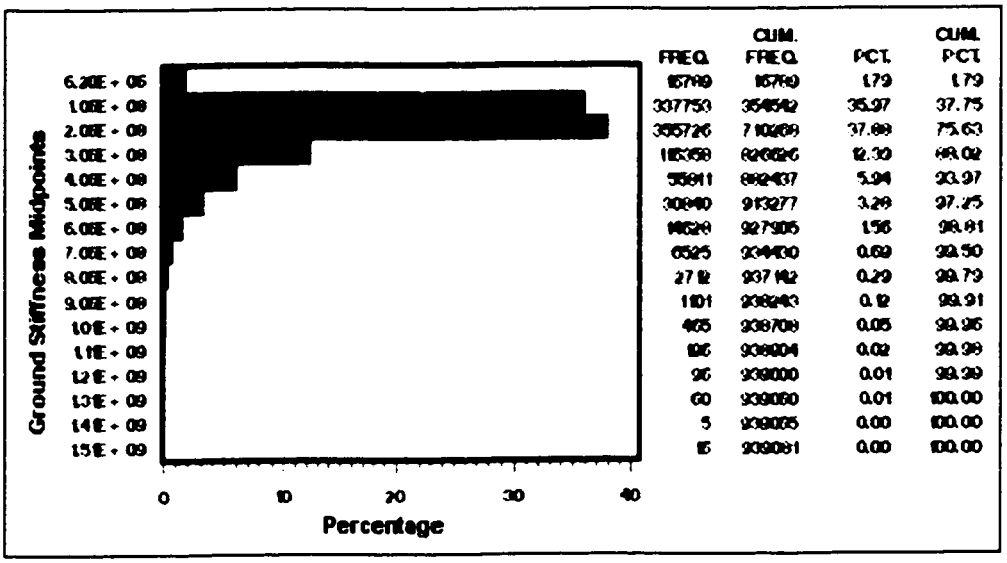

Figure II.2: Histogram of visually edited ground stiffness data.

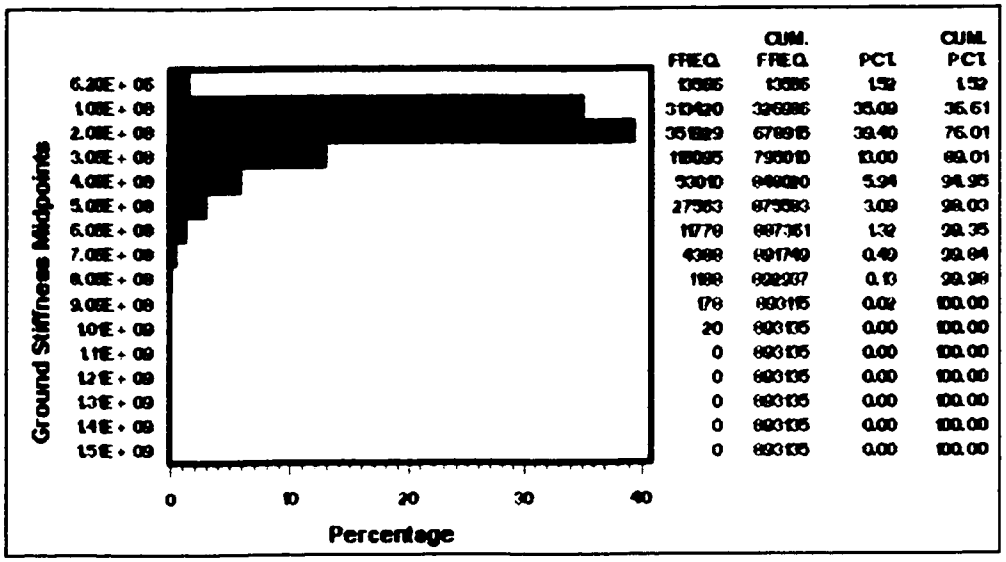

	FREQ.	CUM. FREQ.	PCT.	CUM. PCT.
6.20E+08	13686	13686	1.52	1.52
1.08E+09	312420	326086	35.09	36.61
2.08E+09	351829	677915	39.40	76.01
3.08E+09	118085	796000	13.00	89.01
4.08E+09	53010	849010	5.94	94.95
5.08E+09	27353	876363	3.09	98.03
6.08E+09	11778	887361	1.32	99.35
7.08E+09	4388	891749	0.49	99.84
8.08E+09	1188	892937	0.13	99.98
9.08E+09	178	893115	0.02	100.00
1.01E+10	20	893135	0.00	100.00
1.11E+10	0	893135	0.00	100.00
1.21E+10	0	893135	0.00	100.00
1.31E+10	0	893135	0.00	100.00
1.41E+10	0	893135	0.00	100.00
1.51E+10	0	893135	0.00	100.00

Figure II.3: Histogram ground stiffness data after three-sigma limits application.

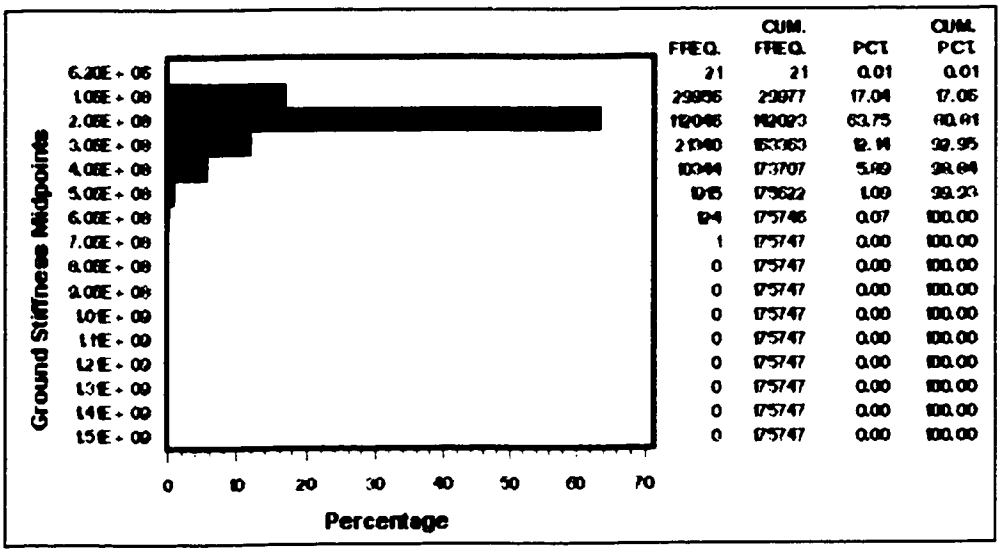

	FREQ.	CUM. FREQ.	PCT.	CUM. PCT.
6.20E+08	21	21	0.01	0.01
1.08E+09	29956	29977	17.04	17.05
2.08E+09	112046	142023	63.75	80.81
3.08E+09	21040	163063	11.97	92.78
4.08E+09	10044	173107	5.71	98.49
5.08E+09	1515	174622	0.86	99.35
6.08E+09	124	174746	0.07	99.42
7.08E+09	1	174747	0.00	99.42
8.08E+09	0	174747	0.00	99.42
9.08E+09	0	174747	0.00	99.42
1.01E+10	0	174747	0.00	99.42
1.11E+10	0	174747	0.00	99.42
1.21E+10	0	174747	0.00	99.42
1.31E+10	0	174747	0.00	99.42
1.41E+10	0	174747	0.00	99.42
1.51E+10	0	174747	0.00	99.42

Figure II.4: Histogram ground stiffness data after smoother application.

APPENDIX III

3D Interval Velocity Model Semi-variograms and Data Application Results

III.1 Uphole Data Semi-Variograms

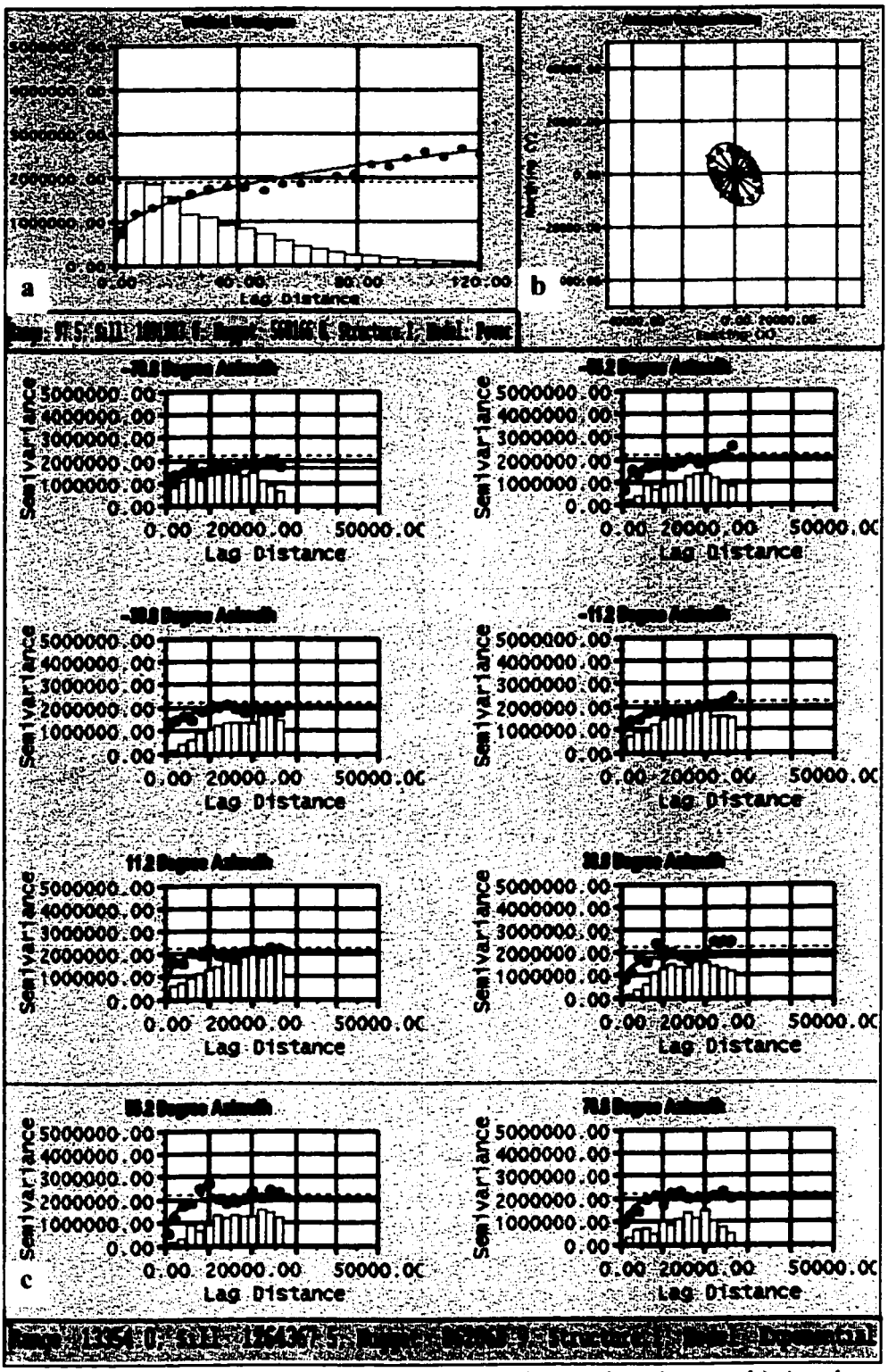

Figure III.1: a) Vertical uphole interval velocity semi-variogram b) Areal uphole data semi-variograms anisotropic modeling with an anisotropy ratio of 1.5:1 c) Areal uphole data directional semi-variograms.

III.2 3D Interval Velocity Models

Two cross sections are shown next from every 3D interval velocity models described in Chapter 5. The locations of these two sections are shown in the basemap of Figure III.2.

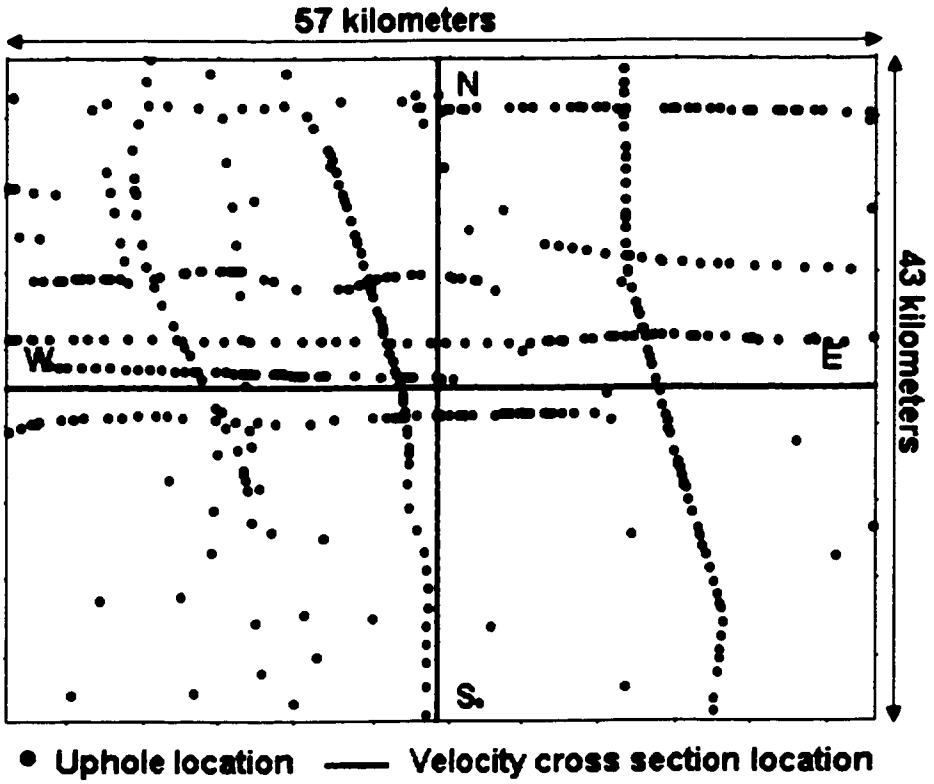

Figure III.2: A basemap exhibiting the uphole locations and the interval velocity cross sections locations.

III.2.1 Surface to SRD Uphole Model

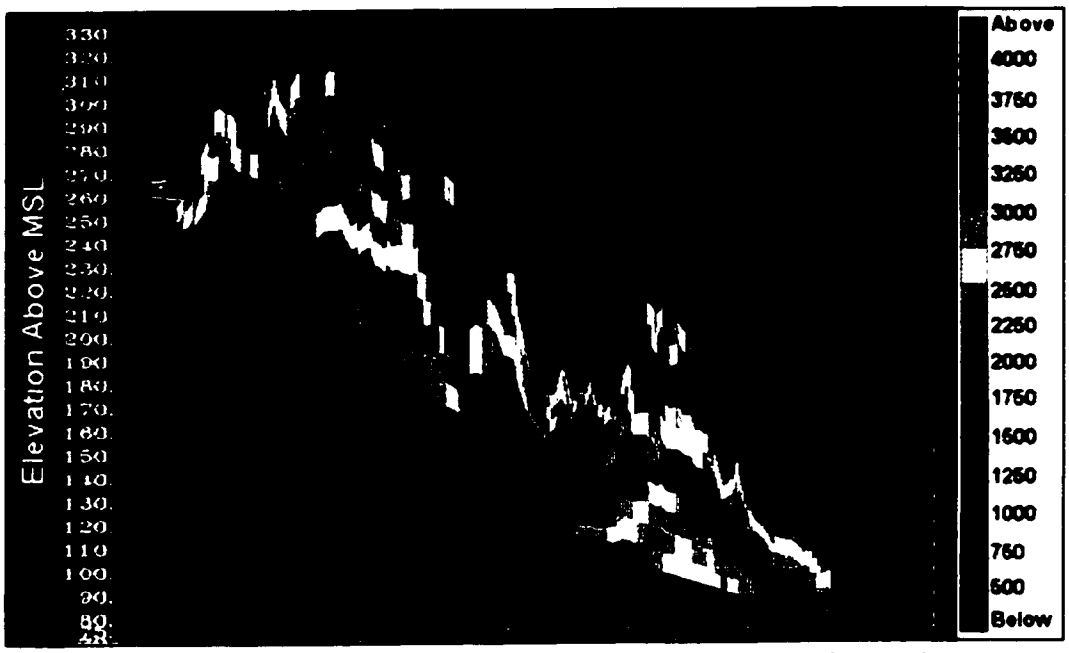

Figure III.3: East-west interval velocity cross section from surface to SRD obtained from modeling of uphole data in (m/s).

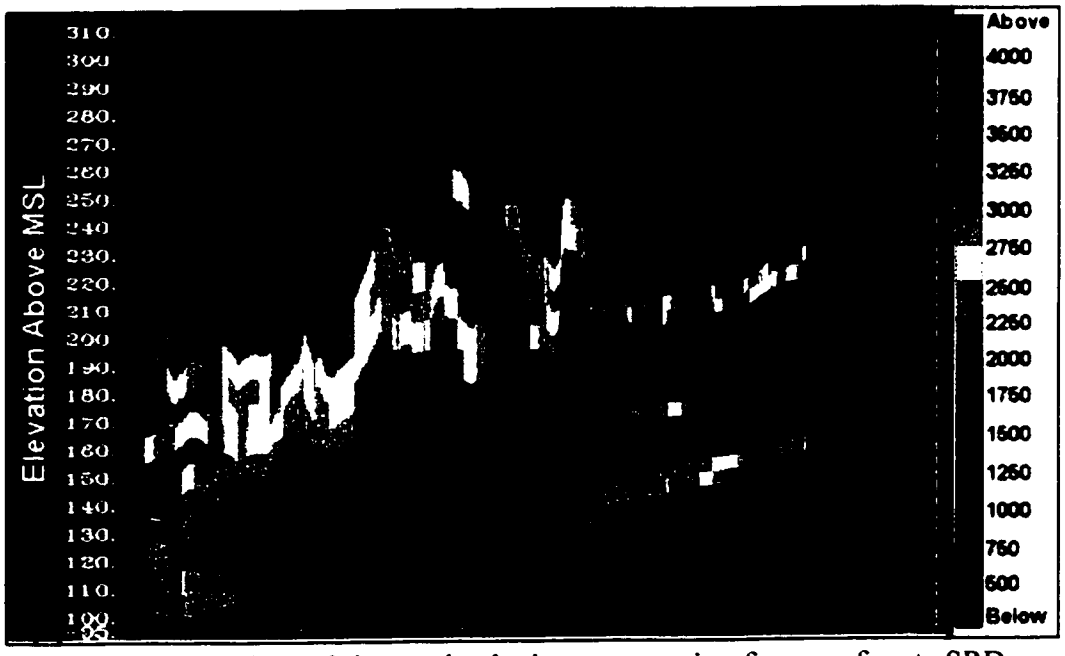

Figure III.4: North-south interval velocity cross section from surface to SRD obtained from modeling of uphole data in (m/s).

III.2.2 Surface to 50 meters depth Uphole Model

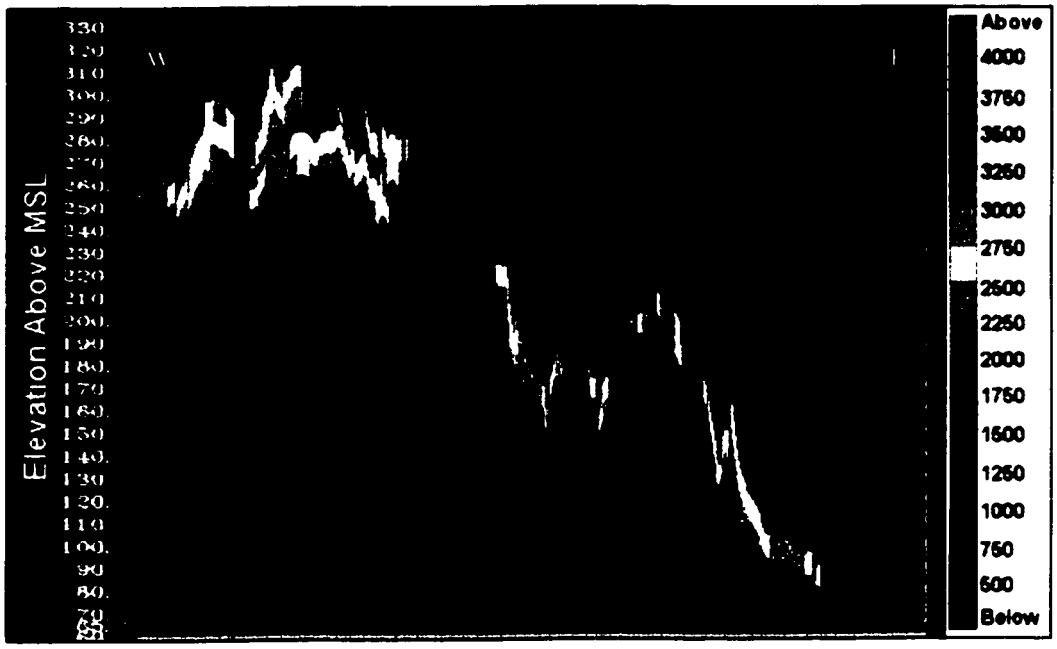

Figure III.5: East-west interval velocity cross section from surface to 50 meters depth obtained from modeling of uphole data in (m/s).

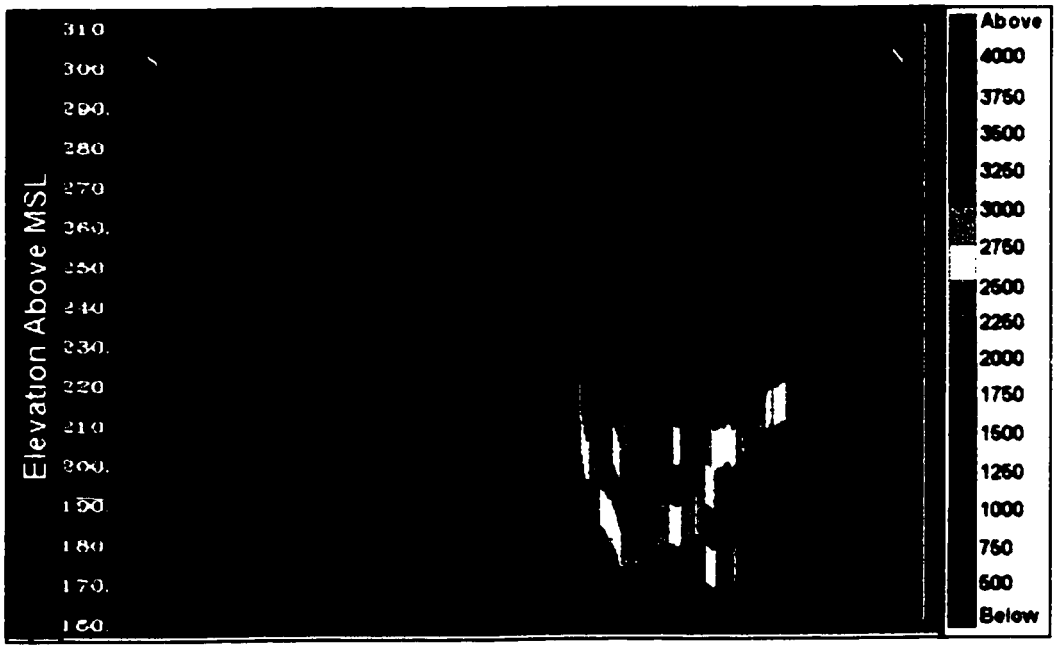

Figure III.6: North-south interval velocity cross section from surface to 50 meters depth obtained from modeling of uphole data in (m/s).

III.2.3 Surface to 50 meters depth Integrated Model

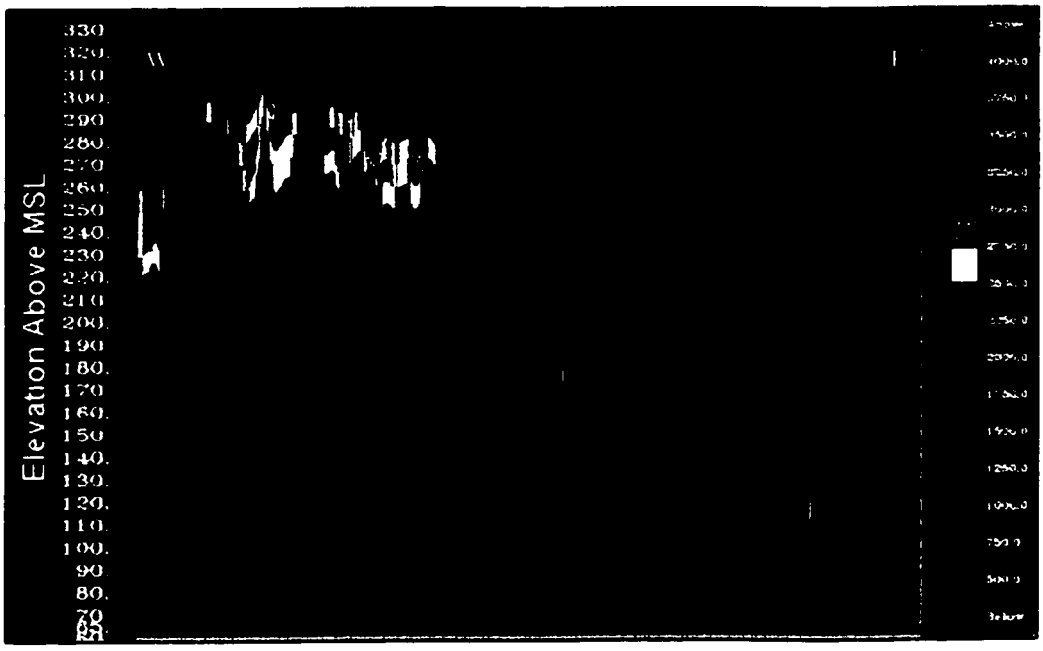

Figure III.7: East-west interval velocity cross section from surface to 50 meters depth obtained from integrated data modeling.

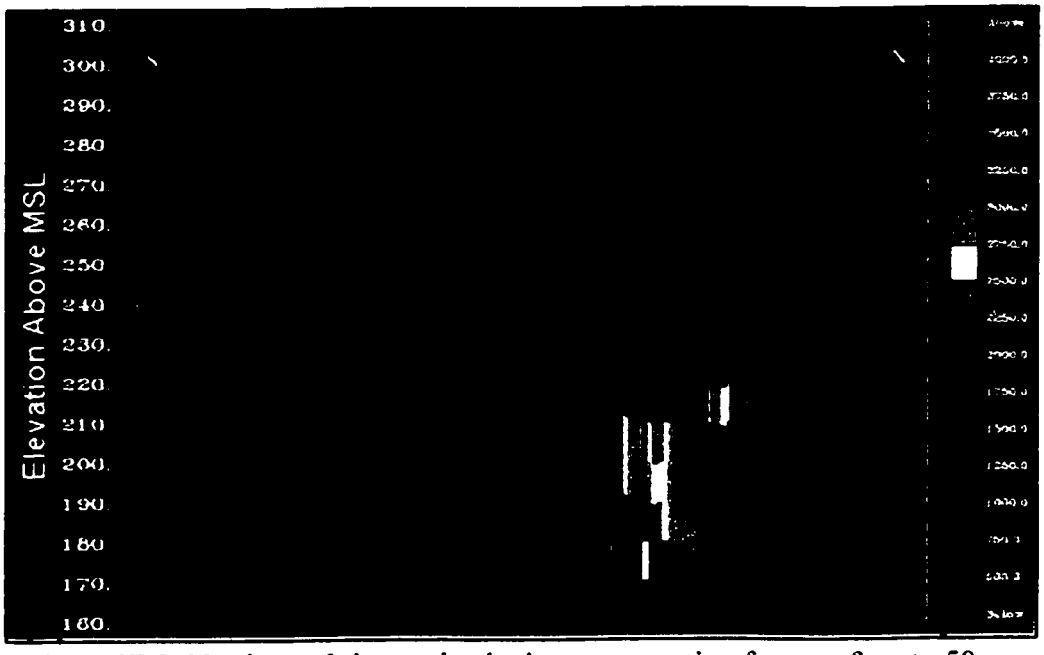

Figure III.8: North-south interval velocity cross section from surface to 50 meters depth obtained from integrated data modeling.

III.3 Seismic Sections

Figure III.9 shows a basemap of the area where seismic data were processed with different statics models. Figures III.10 to III.15 show seismic sections along some lines within this area.

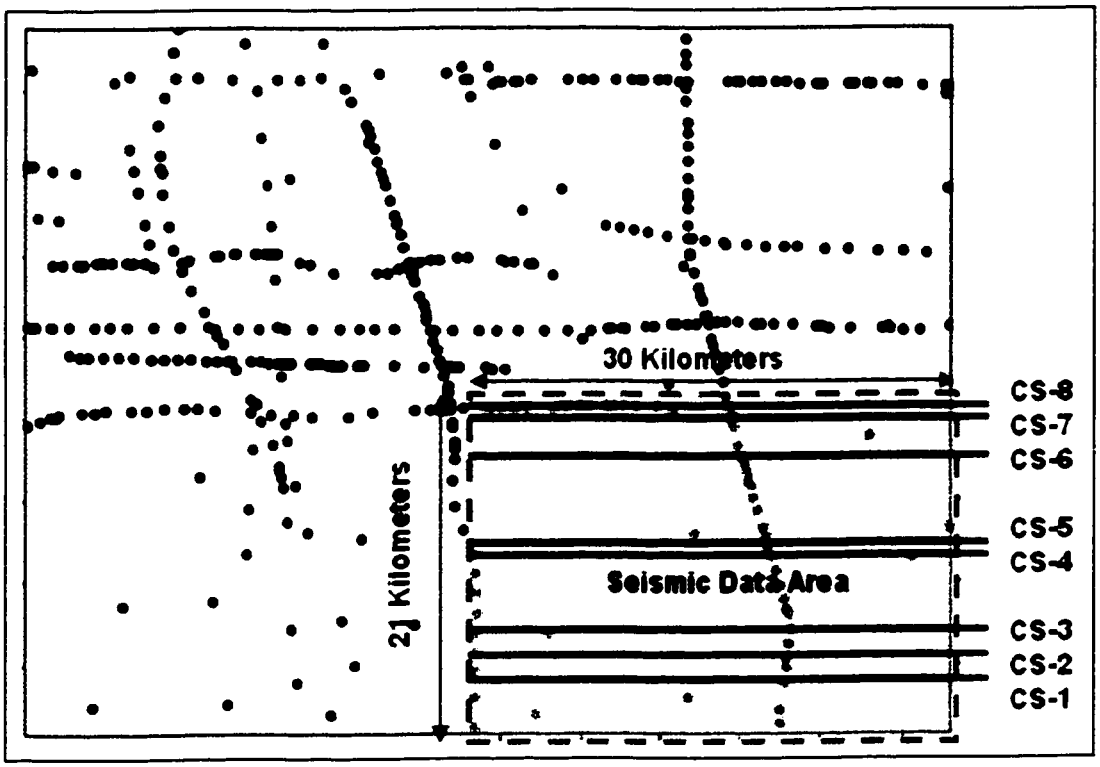

Figure III.9: Basemap for seismic sections and uphole locations.

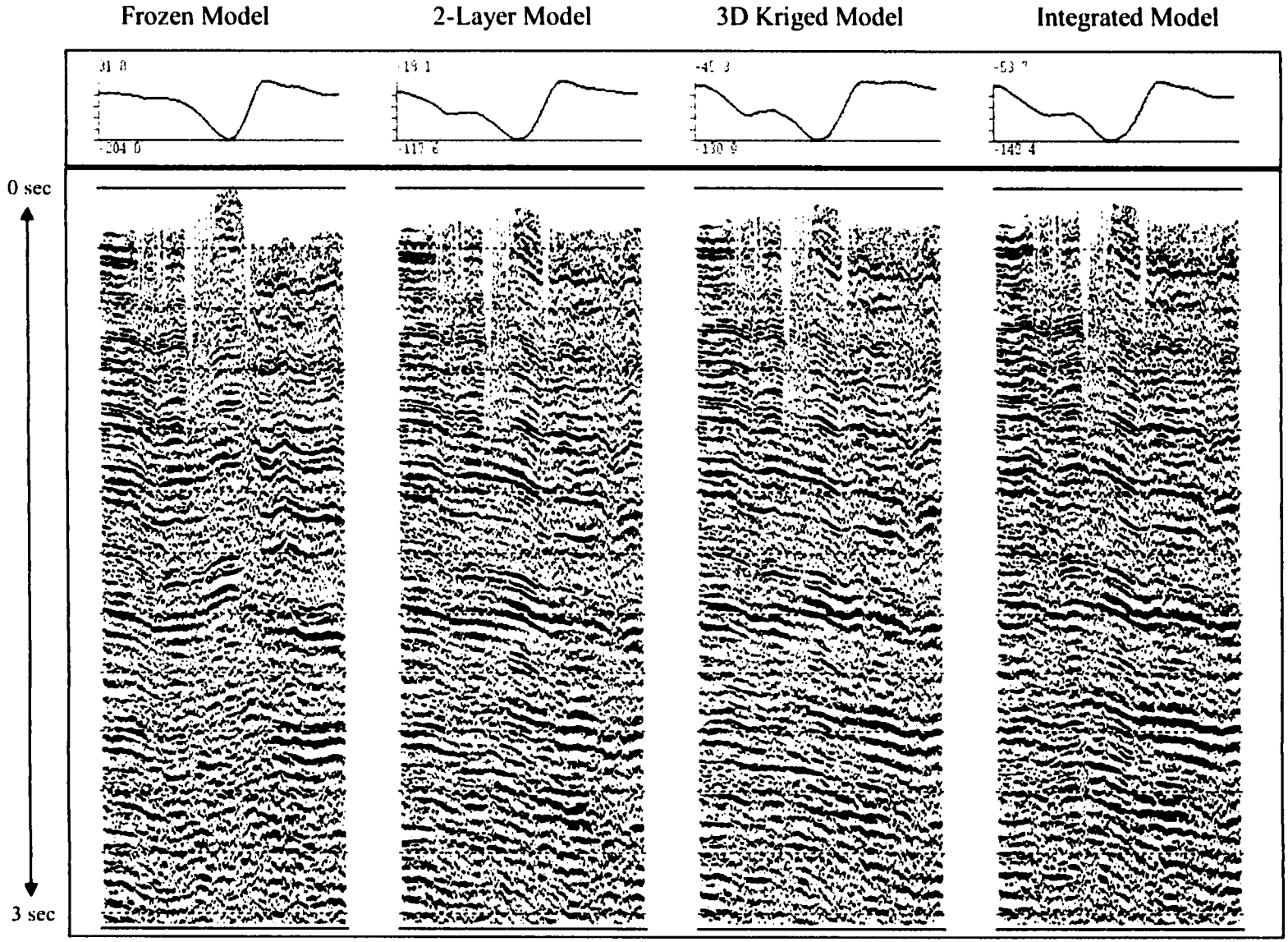

Figure III.10: Four seismic sections along line CS-1 processed using different statics models. Red lines on top show total CMP statics mean in ms.

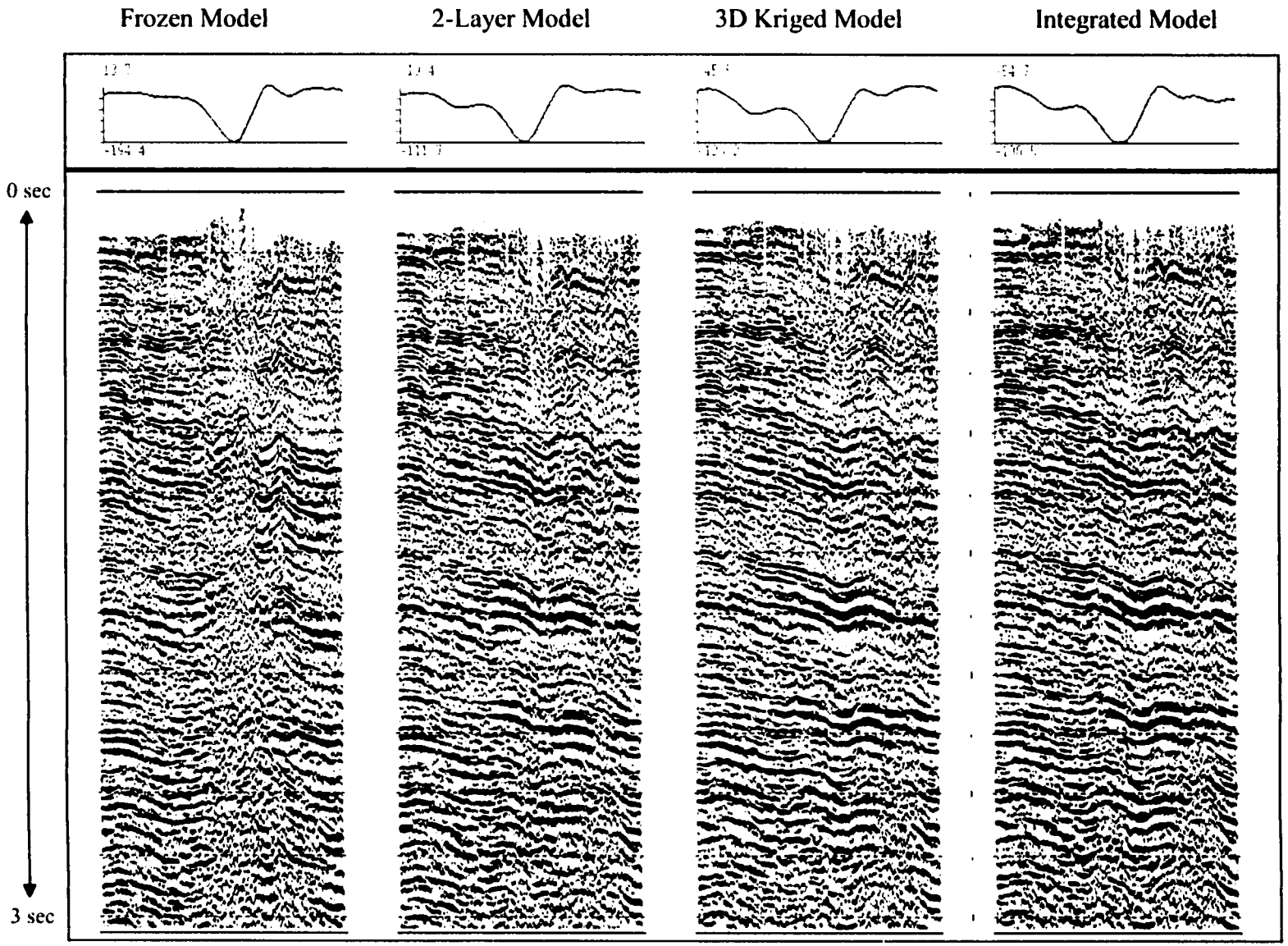

Figure III.11: Four seismic sections along line CS-2 processed using different statics models. Red lines on top show total CMP statics mean in ms.

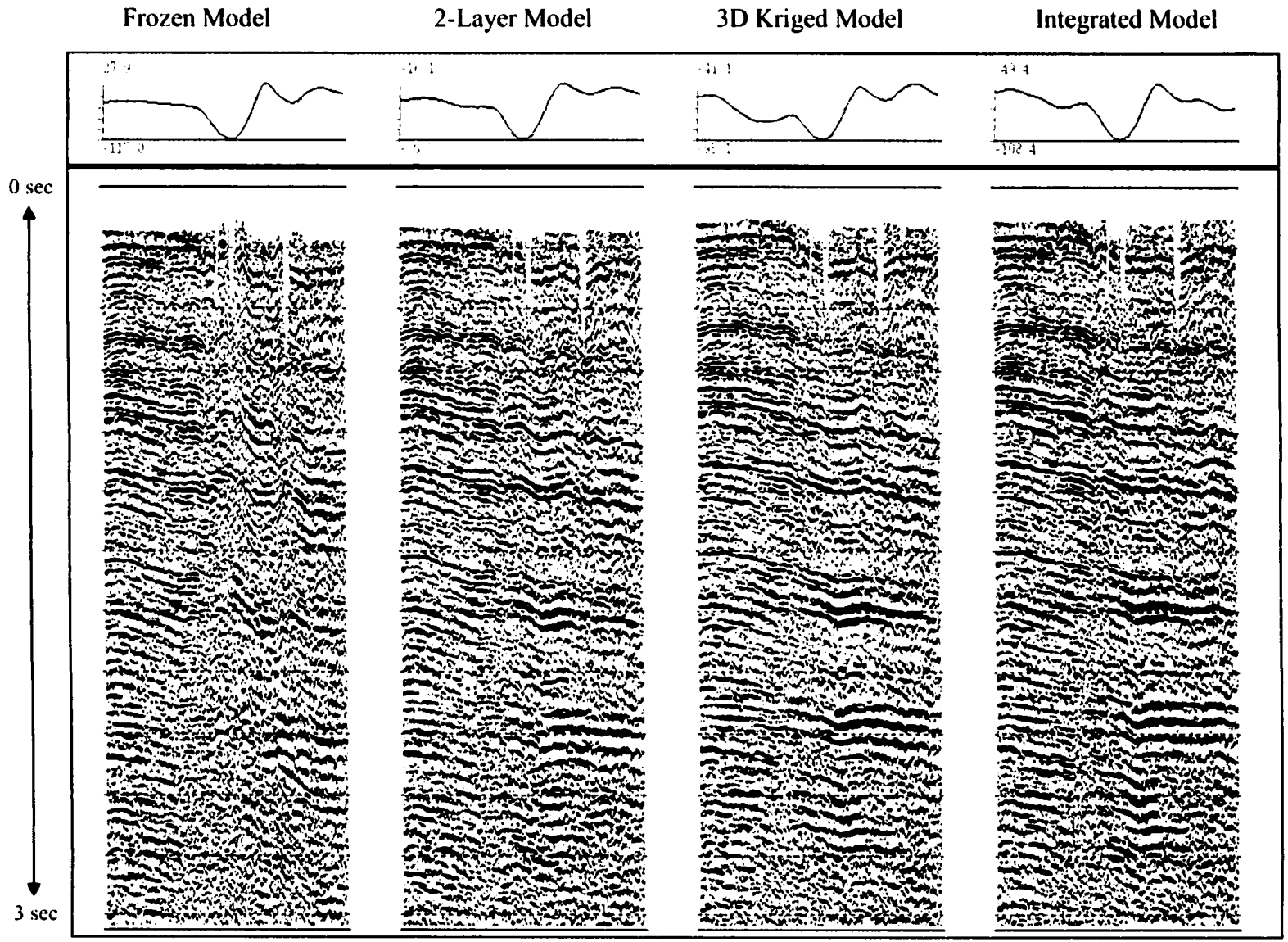

Figure III.12: Four seismic sections along line CS-3 processed using different statics models. Red lines on top show total CMP statics mean in ms.

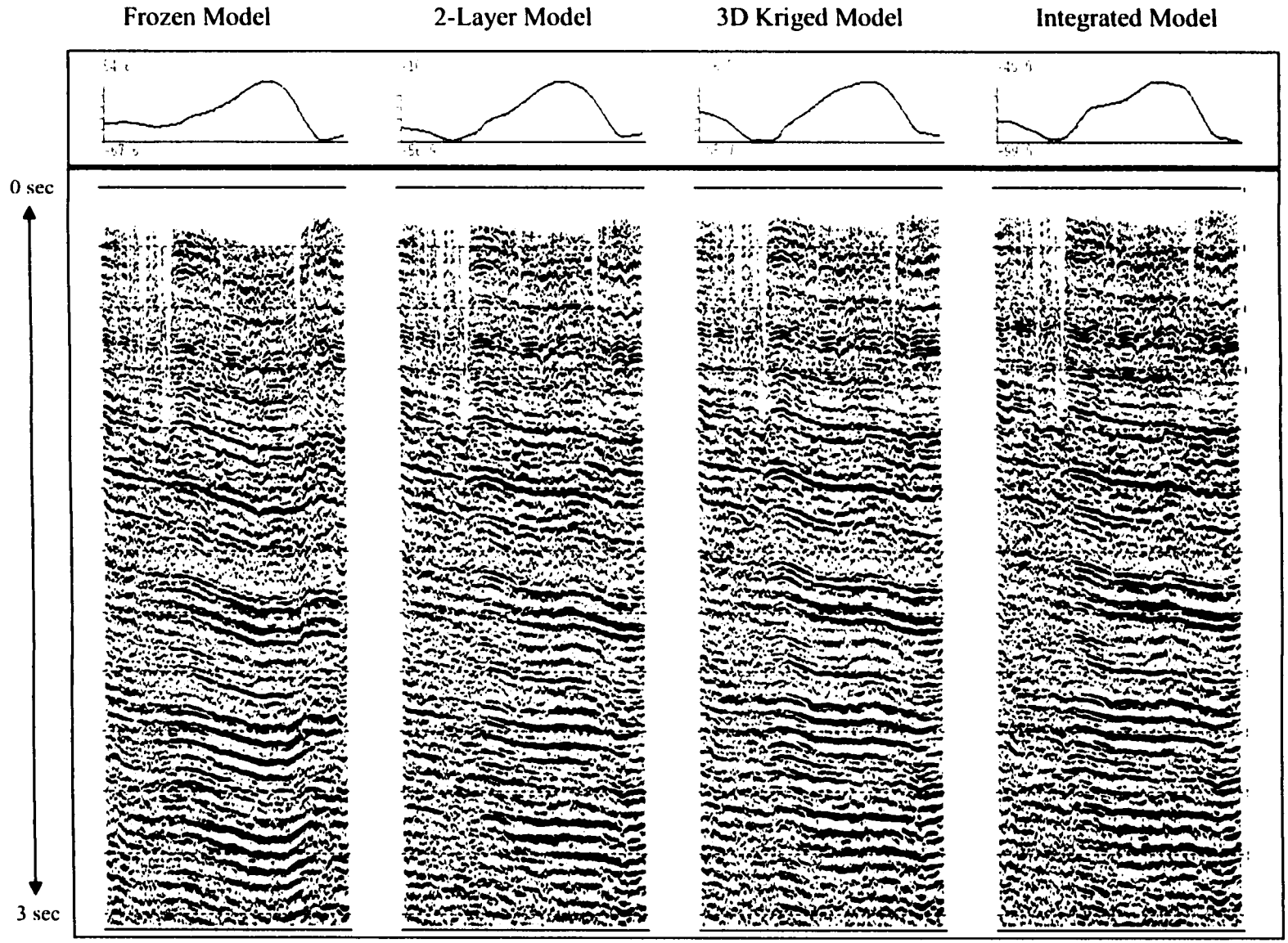

Figure III.13: Four seismic sections along line CS-4 processed using different statics models. Red lines on top show total CMP statics mean in ms.

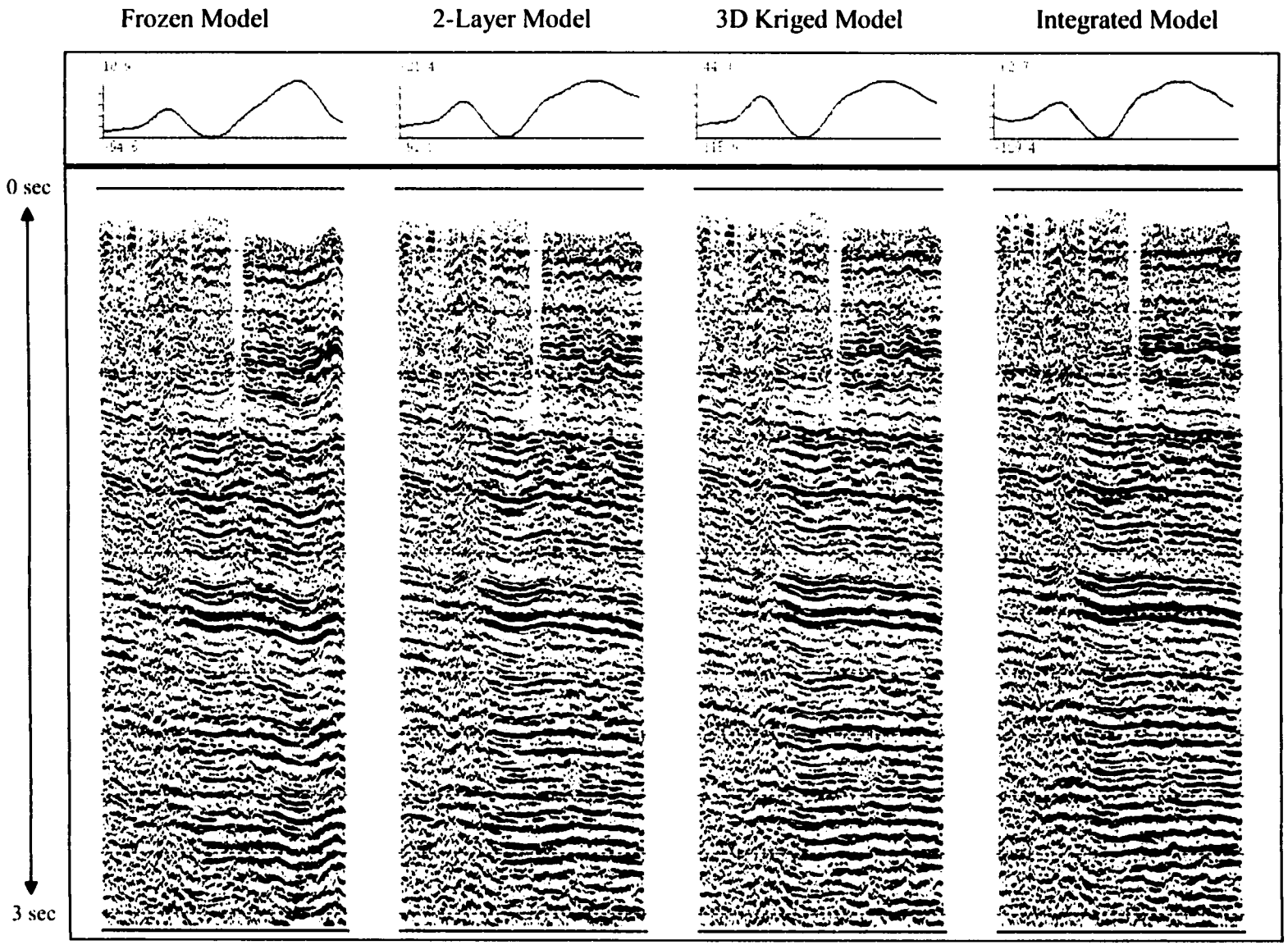

Figure III.14: Four seismic sections along line CS-6 processed using different statics models. Red lines on top show total CMP statics mean in ms.

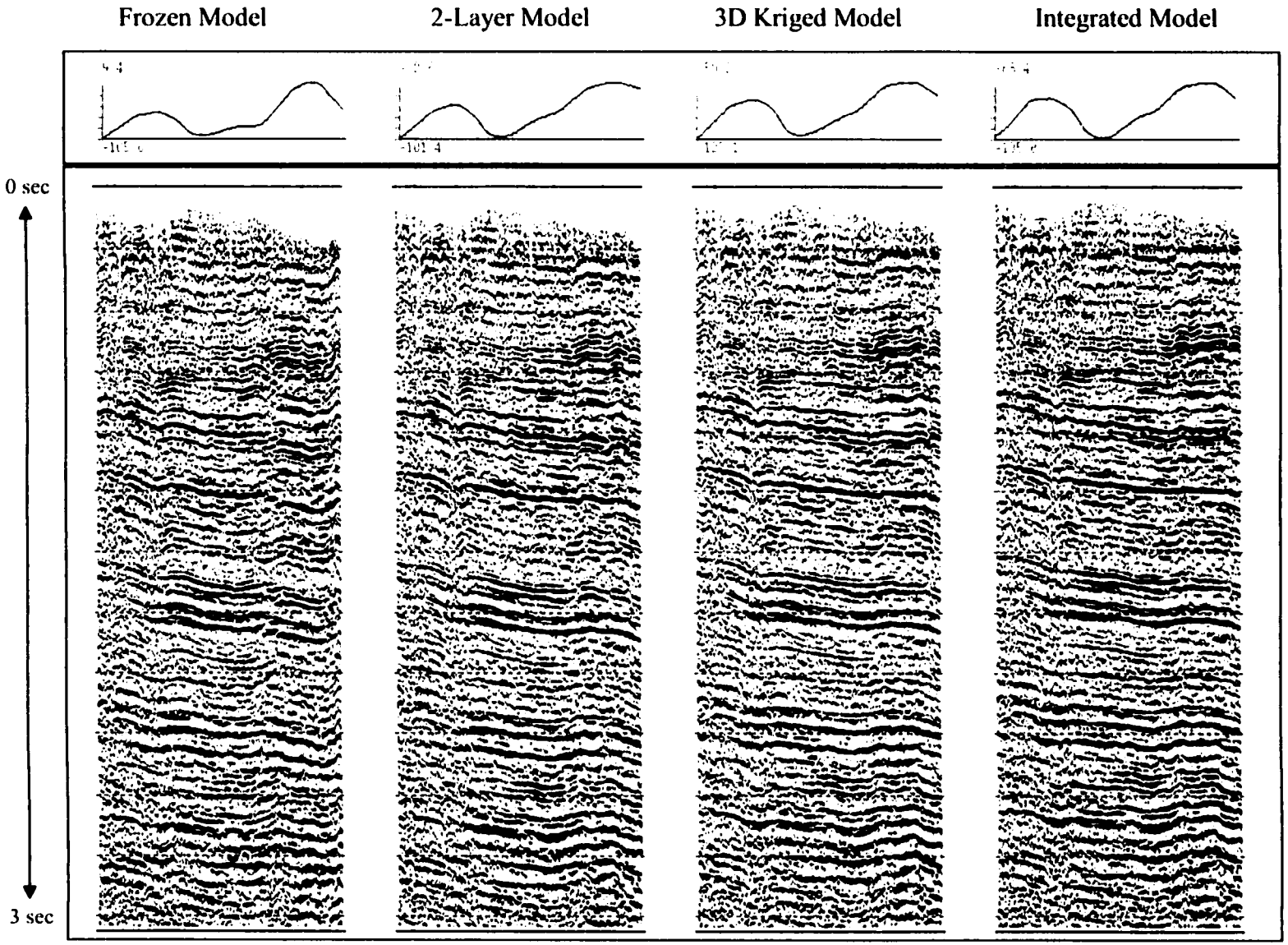

Figure III.15: Four seismic sections along line CS-7 processed using different statics models. Red lines on top show total CMP statics mean in ms.